



Universität Augsburg
Mathematisch-Naturwissenschaftliche
Fakultät

Negative Casimir entropies in the plane–sphere geometry

Masterarbeit

im Studiengang Physik

vorgelegt von: Michael Hartmann
geboren am: 27.10.1987
Matrikelnummer: 1071177
Lehrstuhl: Theoretische Physik I

Augsburg, den 13. Juni 2014

“There is a theory which states that if ever anyone discovers exactly what the Universe is for and why it is here, it will instantly disappear and be replaced by something even more bizarre and inexplicable. – There is another theory which states that this has already happened.”

— Douglas Adams, *The Restaurant at the End of the Universe*

Erstgutachter: Prof. Dr. Gert-Ludwig Ingold

Zweitgutachter: Prof. Dr. Thilo Kopp

Contents

1. Introduction	1
2. Plane wave basis and multipole basis	3
2.1. Notation	3
2.2. Maxwell equations in vacuum	4
2.3. Plane wave basis	5
2.4. Multipole basis	7
2.5. Matrix elements for the change of basis	8
3. Reflection properties of metals	12
3.1. Drude model	12
3.2. Plasma model and perfect reflectors	13
3.3. Fresnel coefficients	14
3.4. Mie coefficients	17
4. The scattering formula in the plane–plane geometry	19
4.1. Round-trip operator	19
4.2. Free energy	21
4.3. Perfect reflectors	22
4.4. Drude mirrors	23
4.5. Entropy	24
5. The scattering formula in the plane–sphere geometry	26
5.1. Round-trip operator \mathcal{M}	27
5.2. Round-trip operator in multipole basis	27
5.3. Matrix elements in multipole basis	29
5.4. Wick rotation	31
5.5. Properties of the scattering matrix	31
5.6. Scaling	33
5.7. Matsubara frequency $\xi = 0$	34
5.8. Conclusion	35
6. Numerical issues	37
6.1. Truncation of the vector space	37
6.2. Modified Bessel functions and Mie coefficients	38
6.3. Integration	39

6.4. Matrix elements	41
6.5. Determinant	44
6.6. Truncation of the infinite sum over n	45
6.7. Truncation of the sum over m	46
6.8. Numerical differentiation	48
6.9. Numerical stability	48
7. The proximity force approximation	50
7.1. The PFA for the plane–sphere geometry	50
7.2. Comparison with scattering approach	52
8. Large-distance limit	54
9. Thermal effects	58
9.1. Low temperatures	58
9.2. High temperatures	60
9.3. Intermediate temperatures	64
10. Negative entropies	67
11. Conclusion and outlook	71
A. Special functions	73
A.1. Spherical harmonics	73
A.2. Associated Legendre polynomials	74
A.3. Wigner (small) d-matrix elements	76
A.4. Modified Bessel functions	76
A.5. Polylogarithms	77
B. Proofs and mathematical transformations	79
B.1. Normalization	79
B.2. Commutation of \mathcal{J}_z and \mathcal{M}	80
B.3. Determinants of block matrices	81
B.4. Equivalence of the matrix elements of CANAGUIER–DURAND et al.	81
B.5. $B_{\ell_1 \ell_2, p}^{(m)}$ for $\xi \rightarrow 0$	82
B.6. Determinant of $\mathcal{M}^{(m)}(P, P)$ for $\xi \rightarrow 0$	83
B.7. Infinite series	84
B.8. Scattering at a sphere and factor -2	84
C. Numerical implementation	86
Bibliography	87

1. Introduction

In 1948 Hendrik Casimir considered two parallel, perfectly conducting plates in vacuum at temperature $T = 0$ and predicted an attracting force [14]. This force was experimentally verified in 1956 by DERJAGUIN, ABRIKOSOVA and LIFSHITZ [16] as well as in 1958 by SPARNAAY [48]. The accuracy of Casimir experiments has been drastically improved over the last decades and several experiments claim to achieve a precision at the 1% level [33]. Experiments are usually carried out using a metallic sphere and a metallic plate at ambient temperature. In particular, the plane–sphere geometry avoids misalignments that render accurate measurements in the plane–plane configuration difficult.

Since the Casimir effect is a manifestation of vacuum fluctuations in the mesoscopic world, it has relations to many open physical questions. As the Casimir force is the dominant force between electrically neutral bodies at micron or sub-micron distances, it plays an important role in the search for new hypothetical forces predicted by unified theories like string theory [39]. Moreover, the Casimir effect is linked with the theory of gravitation and in particular the cosmological constant. All energy gravitates and thus zero point fluctuations are expected to contribute to the stress–energy tensor in Einstein’s field equations [28]. In fact, several cosmological observations like the discovery of the acceleration of the universe [46] suggest that the energy density of vacuum is non-zero, however, the measured value of the cosmological constant and the estimation due to zero point fluctuations differ by about 120 orders of magnitude [22]. Also, Casimir forces are closely related with van der Waals forces and may be interpreted as retarded van der Waals forces [31].

Many different theoretical approaches to the Casimir effect have been developed or revised in the last decade: Experiments are usually compared with results obtained using the proximity force approximation (PFA). The PFA is an approximation that links arbitrary geometries to the simple plane–plane geometry. Although no error estimates exist, the PFA is believed to become accurate when the separation between the objects becomes small [18]. Further methods include worldline numerics [20, 37] or approximations based on classical ray optics [29]. Yet another powerful method is the scattering approach [32] which links the scattering operators in vacuum with the Casimir free energy.

Moreover, negative entropies are found for some geometries and parameters in the Casimir effect. Negative entropies, for example, occur in the plane–plane geometry for metals described by the Drude model. In addition, this effect also occurs in the plane–sphere geometry even for perfect reflectors, thus suggesting a geometrical origin of negative entropies [36]. This is in general not a problem, since the Casimir free energy is an interaction energy and does not describe the entire physical system [36]. However, the origin of negative entropies is not understood very well.

In this thesis, we will apply the scattering approach to the Casimir effect in the plane–sphere geometry at finite temperature and study the effect of negative entropies for perfect reflectors. We will

show that the Maxwell equations in vacuum are equivalent to the vector Helmholtz equation, present the solutions to the scattering of plane waves at a sphere and a plane, and derive the matrix elements of the scattering operator. This enables us to compare the proximity force approximation with exact calculations. In the limit of large separations we will derive an analytical expression for the Casimir free energy and study the origin of negative entropies. For low temperatures we investigate and compare free energy and entropy with those obtained within the PFA. In the high temperature limit the evaluation of the scattering formula becomes notably simpler, which enables us to study smaller separations and check various suggested expressions for the free energy. Finally, we investigate negative entropies for arbitrary separations and temperatures. This will help us to gain a deeper understanding of the effect of negative entropies.

2. Plane wave basis and multipole basis

In this chapter, we show that the Maxwell equations in vacuum are equivalent to the vector Helmholtz equation. We introduce the plane wave basis and the multipole basis as solutions and derive the matrix elements implementing the change from the multipole basis to the plane wave basis. But before doing so, we first adapt the notation to our problem.

2.1. Notation

We adapt the notation of CANAGUIER–DURAND et al. [10, 13]: By \mathbf{k} we denote the projection of the wave vector $\mathbf{K} = (K_x, K_y, K_z)$ onto the xy -plane. The z -component K_z of the wave vector, the projection of the wave vector onto the xy -plane \mathbf{k} and the frequency ω are related by the dispersion relation

$$\omega^2 = c^2(K_x^2 + K_y^2 + K_z^2) = c^2(\mathbf{k}^2 + K_z^2). \quad (2.1)$$

Thus K_z is determined by the dispersion relation (2.1), the frequency ω , and the direction of propagation $\phi = \pm 1$ in positive or negative direction of z . We denote the unsigned value of the z -component of the wave vector by k_z , i.e. $K_z = +k_z$ when propagating in positive direction of z and otherwise $K_z = -k_z$. Similarly, we denote the vector (x, y, z) by \mathbf{R} and the projection onto the xy -plane by \mathbf{r} .

In conclusion, we define:

$$\mathbf{R} = (x, y, z), \quad \mathbf{r} = (x, y), \quad r = \sqrt{x^2 + y^2} \quad (2.2)$$

$$\mathbf{K} = (K_x, K_y, \phi k_z), \quad \mathbf{k} = (k_x, k_y), \quad k = \sqrt{k_x^2 + k_y^2} \quad (2.3)$$

$$K_z = \phi k_z = \phi \sqrt{\frac{\omega^2}{c^2} - \mathbf{k}^2}, \quad \phi = \pm 1, \quad k_z = \sqrt{\frac{\omega^2}{c^2} - \mathbf{k}^2} \quad (2.4)$$

In a spherical coordinate system the wave vector \mathbf{K} can be expressed as

$$\mathbf{K} = \frac{\omega}{c} (\sin \theta^\pm \cos \varphi, \sin \theta^\pm \sin \varphi, \cos \theta^\pm), \quad (2.5)$$

where θ^\pm and φ are polar and azimuthal angles in k -space. In particular, θ^\pm depends on the propagation of the wave in $\pm z$ -direction. Sine and cosine of the polar angle θ^\pm are related to ω/c , k and k_z by

$$\sin \theta^\pm = \frac{ck}{\omega}, \quad \cos \theta^\pm = \pm \frac{ck_z}{\omega}. \quad (2.6)$$

2.2. Maxwell equations in vacuum

In this section we show that in vacuum the electric and magnetic fields \mathbf{E} and \mathbf{B} obey the vector Helmholtz equation. A more detailed discussion can be found in common textbooks [6, 27, 38, 49].

In vacuum the Maxwell equations are given by

$$\nabla \cdot \mathbf{E}(\mathbf{R}, t) = 0 \qquad \nabla \cdot \mathbf{B}(\mathbf{R}, t) = 0 \qquad (2.7)$$

$$\nabla \times \mathbf{E}(\mathbf{R}, t) = -\frac{\partial \mathbf{B}}{\partial t} \qquad \nabla \times \mathbf{B}(\mathbf{R}, t) = \mu_0 \epsilon_0 \frac{\partial \mathbf{E}}{\partial t}. \qquad (2.8)$$

Applying the curl operator to the Maxwell–Faraday equation yields

$$\nabla \times (\nabla \times \mathbf{E}) = -\frac{\partial}{\partial t} \nabla \times \mathbf{B} = -\mu_0 \epsilon_0 \frac{\partial^2 \mathbf{E}}{\partial t^2}. \qquad (2.9)$$

On the other hand the vector identity $\nabla \times \nabla \times = \nabla \nabla - \Delta$ yields

$$\nabla \times (\nabla \times \mathbf{E}) = \nabla (\nabla \cdot \mathbf{E}) - \Delta \mathbf{E} = -\Delta \mathbf{E}. \qquad (2.10)$$

From (2.9) and (2.10) we see that the electric field obeys the wave equation

$$\left(\Delta - \frac{1}{c^2} \frac{\partial^2}{\partial t^2} \right) \mathbf{E}(\mathbf{R}, t) = 0, \qquad (2.11)$$

where $c = (\mu_0 \epsilon_0)^{-1/2}$ is the speed of light in vacuum. In a similar manner all steps can be carried out for the magnetic field as well and thus the electric field \mathbf{E} can be replaced by the magnetic field \mathbf{B} in (2.11). Electric and magnetic fields can be transformed into each other with use of (2.8):

$$\mathbf{B}(\mathbf{R}) = -\frac{i}{\omega} \nabla \times \mathbf{E} \qquad \mathbf{E}(\mathbf{R}) = \frac{ic^2}{\omega} \nabla \times \mathbf{B} \qquad (2.12)$$

Since the wave equation (2.11) is linear, arbitrary fields can be composed of harmonic solutions. Without loss of generality, we assume that the time dependence is given by $e^{-i\omega t}$ [6, 27, 49]:

$$\mathbf{E}(\mathbf{R}, t) = \mathbf{E}(\mathbf{R}) e^{-i\omega t} \qquad \mathbf{B}(\mathbf{R}, t) = \mathbf{B}(\mathbf{R}) e^{-i\omega t} \qquad (2.13)$$

By doing so, the wave equation (2.11) becomes the vector Helmholtz equation

$$(\Delta + k^2) \mathbf{E}(\mathbf{R}) = 0, \qquad (\Delta + k^2) \mathbf{B}(\mathbf{R}) = 0. \qquad (2.14)$$

We see that the Maxwell equations in vacuum are equivalent to the vector Helmholtz equation. As we consider vacuum and thus a source-free region of space, the divergence of the electric and magnetic fields \mathbf{E} and \mathbf{B} must vanish. For this reason, we are looking for solutions of the vector Helmholtz equation with vanishing divergence. In the following sections, we introduce two solutions, namely the plane wave basis and the multipole basis.

2.3. Plane wave basis

The vector Helmholtz equation (2.14) represents a wave equation in every component of \mathbf{E} . In a Cartesian coordinate system, solutions to the Helmholtz equation can be constructed by superposition of plane waves

$$\mathbf{E}(\mathbf{R}) = \int d^3\mathbf{K} \mathbf{A}(\mathbf{K}) e^{i\mathbf{K}\cdot\mathbf{R}}, \quad (2.15)$$

where $\mathbf{A}(\mathbf{K})$ is an arbitrary complex vector-valued function. Since the divergence of (2.15) has to vanish according to (2.7), only two of the three components of the electric field \mathbf{E} are independent and the wave vector \mathbf{K} is perpendicular to \mathbf{A} :

$$\nabla \cdot \mathbf{E} = 0 \quad \Leftrightarrow \quad \mathbf{K} \cdot \mathbf{A} = 0 \quad (2.16)$$

The absolute value of the z -component of the wave vector $K_z = \phi k_z$ is determined by the dispersion relation (2.1). Source-free solutions of the Helmholtz equation can thus be written in the form

$$\mathbf{E}(\mathbf{R}) = \sum_p \sum_{\phi=\pm 1} \int d^2\mathbf{k} \alpha_{\phi,p}(\mathbf{k}) A \hat{\mathbf{e}}_p e^{i(\mathbf{k}\cdot\mathbf{r} + \phi k_z z)}, \quad (2.17)$$

where $\hat{\mathbf{e}}_p$ are orthonormal polarization vectors and A is a normalizing constant. In addition, we have to sum over the two polarization vectors $\hat{\mathbf{e}}_p$ and the propagation directions $\phi = \pm 1$. The coefficients $\alpha_{\phi,p}$ correspond to expansion coefficients. The normalizing constant A is determined by the normalization condition

$$\langle \mathbf{k}', \omega', \phi', p' | \mathbf{k}, \omega, \phi, p \rangle \stackrel{!}{=} \delta_{pp'} \delta_{\phi\phi'} \delta(\mathbf{k} - \mathbf{k}') \delta\left(\frac{\omega}{c} - \frac{\omega'}{c}\right). \quad (2.18)$$

The calculation of A is carried out in appendix B.1. So we arrive at the basis functions

$$\langle \mathbf{R} | \mathbf{k}, \omega, \phi, p \rangle \equiv \mathbf{E}_{\mathbf{k},\omega,\phi,p}(\mathbf{R}) = \frac{\hat{\mathbf{e}}_p}{(2\pi)^{3/2}} \sqrt{\left|\frac{\omega}{ck_z}\right|} e^{i(\mathbf{k}\cdot\mathbf{r} + \phi k_z z)}. \quad (2.19)$$

We still have to pick the two polarization vectors. The actual choice of the polarization vectors is not unique, however, the divergence of (2.19) must vanish. Moreover, we demand the polarization vectors to be orthonormal as this will simplify our calculations. We will choose the polarization vectors in such a way that one basis function is transverse electric ($p = \text{TE}$), i.e., $E_z = 0$ and the other basis function is transverse magnetic ($p = \text{TM}$), i.e., $B_z = 0$. This choice is well adapted for the reflection of plane waves at a flat, planar and homogenous interface between dielectrics.

2.3.1. TE modes

We choose the polarization vector $\hat{\mathbf{e}}_{\text{TE}}$ so that the z -component E_z of the electric field vanishes. For this reason, the z -component of the polarization vector $\hat{\mathbf{e}}_{\text{TE}}$ is zero. As the wavevector \mathbf{K} is perpendicular

to $\hat{\mathbf{e}}_{\text{TE}}$

$$\hat{\mathbf{e}}_{\text{TE}} \cdot \mathbf{K} = (\hat{\mathbf{e}}_{\text{TE}})_x k_x + (\hat{\mathbf{e}}_{\text{TE}})_y k_y = 0, \quad (2.20)$$

the polarization vector possesses only one independent component. The polarization vector is thus given by

$$\hat{\mathbf{e}}_{\text{TE}} = (\hat{\mathbf{e}}_{\text{TE}})_x \begin{pmatrix} 1 \\ -k_x/k_y \\ 0 \end{pmatrix} = -\frac{k}{k_y} (\hat{\mathbf{e}}_{\text{TE}})_x \begin{pmatrix} -k_y/k \\ k_x/k \\ 0 \end{pmatrix} = -\frac{k}{k_y} (\hat{\mathbf{e}}_{\text{TE}})_x \hat{\mathbf{e}}_\varphi. \quad (2.21)$$

If we demand $\hat{\mathbf{e}}_{\text{TE}}$ to be a unit vector, the value of the x -component is determined up to a factor of ± 1 . We pick $\hat{\mathbf{e}}_{\text{TE}} \equiv \hat{\mathbf{e}}_\varphi$ and obtain

$$\langle \mathbf{R} | \mathbf{k}, \omega, \phi, p = \text{TE} \rangle = \frac{\hat{\mathbf{e}}_\varphi}{(2\pi)^{3/2}} \sqrt{\left| \frac{\omega}{ck_z} \right|} e^{i(\mathbf{k} \cdot \mathbf{r} + \phi k_z z)}. \quad (2.22)$$

2.3.2. TM modes

We determine the polarization vector for the TM mode in a similar manner like for the TE mode. From $B_z = 0$ we find

$$\mathbf{B}_{\mathbf{k}, \omega, \phi, \text{TM}}(\mathbf{R}) = N \hat{\mathbf{e}}_\varphi e^{i(\mathbf{k} \cdot \mathbf{r} + \phi k_z z)}, \quad (2.23)$$

where N is a constant. We are not interested in calculating N , because the constant will be canceled when we normalize the polarization vector. With use of (2.12) we obtain for the electric field

$$\mathbf{E}_{\mathbf{k}, \omega, \phi, \text{TM}}(\mathbf{R}) = \tilde{N} \nabla \times \hat{\mathbf{e}}_\varphi e^{i(\mathbf{k} \cdot \mathbf{r} + \phi k_z z)}, \quad (2.24)$$

where \tilde{N} is a new constant. The components of the curl operator act only on the exponential function, because polar and azimuthal angles are defined in k -space. Calculating (2.24) and normalizing yields $\hat{\mathbf{e}}_{\text{TM}} = \pm \hat{\mathbf{e}}_\theta$. We pick the solution with the plus sign and obtain

$$\langle \mathbf{R} | \mathbf{k}, \omega, \phi, p = \text{TM} \rangle = \frac{\hat{\mathbf{e}}_\theta}{(2\pi)^{3/2}} \sqrt{\left| \frac{\omega}{ck_z} \right|} e^{i(\mathbf{k} \cdot \mathbf{r} + \phi k_z z)}. \quad (2.25)$$

In contrast to the TE mode, the polarization vector $\hat{\mathbf{e}}_\theta$ depends on the polar angle and thus on the direction of the propagation ϕ .

2.3.3. Fourier transform

In order to obtain the matrix elements implementing the change from multipole basis to plane wave basis, we need the Fourier transforms of the basis functions of the plane wave basis. The Fourier

transforms are given by

$$\langle \mathbf{K} | \mathbf{k}', \omega', \phi', p \rangle = \sqrt{\left| \frac{\omega'}{c k'_z} \right|} \hat{\mathbf{e}}_p \delta(\mathbf{k} - \mathbf{k}') \delta(K_z - \phi' k'_z), \quad (2.26)$$

where $\hat{\mathbf{e}}_p$ corresponds to the polarization vectors for TE and TM polarization.

2.3.4. Conclusion

We briefly outline the main results: The basis functions $|\mathbf{k}, \omega, \phi, p\rangle$ are orthonormal

$$\langle \mathbf{k}', \omega', \phi', p' | \mathbf{k}, \omega, \phi, p \rangle = \delta_{pp'} \delta_{\phi\phi'} \delta(\mathbf{k} - \mathbf{k}') \delta\left(\frac{\omega}{c} - \frac{\omega'}{c}\right), \quad (2.27)$$

and the source-free solutions of the vector Helmholtz equation can be expanded by

$$\mathbf{E}(\mathbf{R}) = \sum_{\phi, p} \int d^2\mathbf{k} \alpha_{\phi, p}(\mathbf{k}) \langle \mathbf{R} | \mathbf{k}, \omega, \phi, p \rangle \quad (2.28)$$

and

$$\mathbf{E}(\mathbf{K}) = \sum_{\phi', p} \int d^2\mathbf{k}' \beta_{\phi', p}(\mathbf{k}') \langle \mathbf{K} | \mathbf{k}', \omega', \phi', p \rangle \quad (2.29)$$

using the plane wave basis.

The plane wave basis is well adapted to the homogeneity in space and time: The basis functions $|\mathbf{k}, \omega, \phi, p\rangle$ are eigenfunctions of the energy operator $\hat{E} = i\hbar \frac{\partial}{\partial t}$ and of the momentum operators $\hat{p}_j = -i\hbar \partial_j$, $j \in \{x, y, z\}$:

$$\hat{E} |\mathbf{k}, \omega, \phi, p\rangle = \hbar\omega |\mathbf{k}, \omega, \phi, p\rangle \quad (2.30)$$

$$\hat{p}_j |\mathbf{k}, \omega, \phi, p\rangle = \hbar K_j |\mathbf{k}, \omega, \phi, p\rangle \quad (2.31)$$

2.4. Multipole basis

Besides the plane wave basis, the source-free solutions of the vector Helmholtz equation can also be expanded in the multipole basis. The basis functions of the multipole basis are defined by the frequency ω , the total angular momentum $\ell(\ell + 1)$, the z -component of the angular momentum m , and the parity.

2. Plane wave basis and multipole basis

According to Ref. [15] the basis functions of the multipole basis in k -space are given by:

$$\begin{aligned}\langle \mathbf{K} | \omega', \ell, m, \mathbf{M} \rangle &= \frac{c}{\omega'} \delta \left(K - \frac{\omega'}{c} \right) \mathbf{X}_{\ell m}(\theta, \varphi) \\ &= \frac{c}{\omega'} \delta \left(K - \frac{\omega'}{c} \right) \left(\hat{\mathbf{e}}_\varphi \partial_\theta - \frac{\hat{\mathbf{e}}_\theta}{\sin \theta} \partial_\varphi \right) \frac{Y_{\ell m}(\theta, \varphi)}{\sqrt{\ell(\ell+1)}}\end{aligned}\quad (2.32)$$

$$\begin{aligned}\langle \mathbf{K} | \omega', \ell, m, \mathbf{E} \rangle &= \frac{c}{\omega'} \delta \left(K - \frac{\omega'}{c} \right) \mathbf{Z}_{\ell m}(\theta, \varphi) \\ &= \frac{c}{\omega'} \delta \left(K - \frac{\omega'}{c} \right) \left(\hat{\mathbf{e}}_\theta \partial_\theta + \frac{\hat{\mathbf{e}}_\varphi}{\sin \theta} \partial_\varphi \right) \frac{Y_{\ell m}(\theta, \varphi)}{\sqrt{\ell(\ell+1)}}\end{aligned}\quad (2.33)$$

The functions $\mathbf{X}_{\ell m}$ and $\mathbf{Z}_{\ell m}$ are usually called vector spherical harmonics (VSH). The VSH are orthonormal on the unit sphere

$$\int d^2 \hat{\mathbf{K}} \mathbf{X}_{\ell m}^*(\hat{\mathbf{K}}) \cdot \mathbf{X}_{\ell' m'}(\hat{\mathbf{K}}) = \int d^2 \hat{\mathbf{K}} \mathbf{Z}_{\ell m}^*(\hat{\mathbf{K}}) \cdot \mathbf{Z}_{\ell' m'}(\hat{\mathbf{K}}) = \delta_{\ell \ell'} \delta_{m m'}, \quad (2.34)$$

$$\int d^2 \hat{\mathbf{K}} \mathbf{X}_{\ell m}^*(\hat{\mathbf{K}}) \cdot \mathbf{Z}_{\ell' m'}(\hat{\mathbf{K}}) = 0, \quad (2.35)$$

and arbitrary vector fields defined on the unit sphere can be expanded using VSH. Confusingly, several different conventions for the VSH exist, for instance see Refs. [3, 4, 6, 35]. The VSH $X_{\ell m}$ and $Z_{\ell m}$ for $\ell = 1, m = 0$ and $\ell = 2, m = 1$ are depicted in Fig. 2.1.

The multipole basis is well adapted to the isotropy of space: The basis functions of the multipole basis are eigenfunctions to \hat{E} , $\hat{\mathbf{J}}^2$, \hat{J}_z und \hat{P} :

$$\hat{E} |\omega, \ell, m, P\rangle = \hbar \omega |\omega, \ell, m, P\rangle \quad (2.36)$$

$$\hat{\mathbf{J}}^2 |\omega, \ell, m, P\rangle = \hbar^2 \ell(\ell+1) |\omega, \ell, m, P\rangle \quad (2.37)$$

$$\hat{J}_z |\omega, \ell, m, P\rangle = \hbar m |\omega, \ell, m, P\rangle \quad (2.38)$$

$$\hat{P} |\omega, \ell, m, P\rangle = \pm |\omega, \ell, m, P\rangle \quad (2.39)$$

In the multipole basis the source-free solutions of the Helmholtz equation can be expanded by

$$\mathbf{E}(\mathbf{K}) = \sum_{P=\mathbf{E}, \mathbf{M}} \sum_{\ell=1}^{\infty} \sum_{m=-\ell}^{\ell} \alpha_{\ell, m, P} \langle \mathbf{K} | \omega, \ell, m, P \rangle. \quad (2.40)$$

2.5. Matrix elements for the change of basis

The matrix elements for the change of basis from plane wave basis to multipole basis can be calculated using their representations in k -space. For the change of a TE-polarized plane wave to an electric

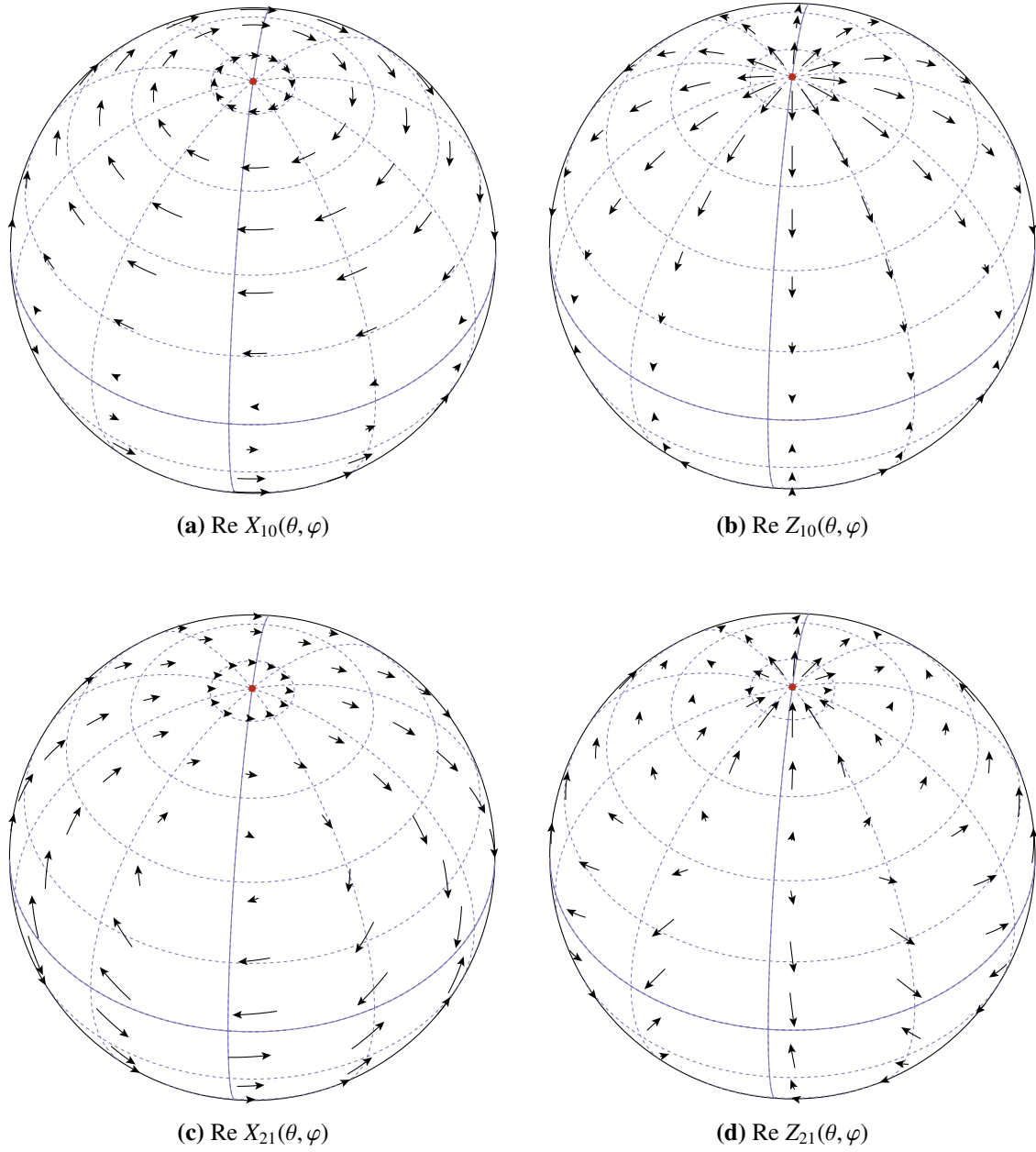


Figure 2.1.: Real part of $X_{\ell m}$ and $Z_{\ell m}$ for $\ell = 1, m = 0$ and $\ell = 2, m = 1$. The red point corresponds to the north pole, the solid lines to the equator, meridian and anti-meridian. For $m = 0$ the vector spherical harmonics $X_{\ell m}$ and $Z_{\ell m}$ are real and independent of φ .

2. Plane wave basis and multipole basis

multipole wave we obtain

$$\begin{aligned} \langle \mathbf{k}, \omega, \pm, \text{TE} | \omega', \ell, m, E \rangle &= \int d^3 \mathbf{K}' \langle \mathbf{k}, \omega, \pm, \text{TE} | \mathbf{K}' \rangle \langle \mathbf{K}' | \omega', \ell, m, E \rangle \\ &= \int d^3 \mathbf{K}' \frac{c}{\omega'} \sqrt{\left| \frac{\omega}{ck_z} \right|} \delta(\mathbf{k}' - \mathbf{k}) \delta(K'_z \mp k_z) \delta\left(K' - \frac{\omega'}{c}\right) \frac{\partial_\varphi Y_{\ell m}(\theta', \varphi')}{\sin \theta' \sqrt{\ell(\ell+1)}}. \end{aligned} \quad (2.41)$$

In order to evaluate the integral we change to spherical coordinates. The product of delta functions becomes

$$\delta(\mathbf{k}' - \mathbf{k}) \delta(K'_z \mp k_z) \delta\left(K' - \frac{\omega'}{c}\right) = \frac{\delta(\theta' - \theta^\pm) \delta(\varphi' - \varphi) \delta\left(K' - \frac{\omega}{c}\right)}{\frac{\omega^2}{c^2} \sin \theta^\pm} \delta\left(K' - \frac{\omega'}{c}\right) \quad (2.42)$$

and the integration variables are now K' , θ' , and φ' . Inserting (2.42) into (2.41) yields

$$\langle \mathbf{k}, \omega, \pm, \text{TE} | \omega', \ell, m, E \rangle = \int dK' d\theta' d\varphi' K'^2 \sin \theta' \frac{c}{\omega'} \sqrt{\left| \frac{\omega}{ck_z} \right|} \quad (2.43)$$

$$\times \frac{\delta(\theta' - \theta^\pm) \delta(\varphi' - \varphi) \delta\left(K' - \frac{\omega}{c}\right)}{\frac{\omega^2}{c^2} \sin \theta^\pm} \delta\left(K' - \frac{\omega'}{c}\right) \frac{\partial_\varphi Y_{\ell m}(\theta', \varphi')}{\sin \theta' \sqrt{\ell(\ell+1)}}. \quad (2.44)$$

The integration of the angular part changes $\theta' \rightarrow \theta^\pm$ and $\varphi' \rightarrow \varphi$, the integration of the radial part yields the delta function $\delta(\omega/c - \omega'/c)$. After cancelling we arrive at

$$\langle \mathbf{k}, \omega, \pm, \text{TE} | \omega', \ell, m, E \rangle = \frac{c}{\omega'} \sqrt{\left| \frac{\omega}{ck_z} \right|} \delta\left(\frac{\omega'}{c} - \frac{\omega}{c}\right) \frac{\partial_\varphi Y_{\ell m}(\theta^\pm, \varphi)}{\sin \theta^\pm \sqrt{\ell(\ell+1)}}. \quad (2.45)$$

The derivative with respect to φ brings up a factor im and after exploiting the identity (2.6) $k = \omega/c \sin \theta^\pm$ we finally obtain

$$\langle \mathbf{k}, \omega, \pm, \text{TE} | \omega', \ell, m, E \rangle = \frac{im}{k} \sqrt{\left| \frac{\omega}{ck_z} \right|} \delta\left(\frac{\omega}{c} - \frac{\omega'}{c}\right) \frac{Y_{\ell m}(\theta^\pm, \varphi)}{\sqrt{\ell(\ell+1)}}. \quad (2.46)$$

In a similar manner one finds for the change from a TE polarized plane wave to an electric multipole wave

$$\langle \mathbf{k}, \omega, \pm, \text{TE} | \omega', \ell, m, M \rangle = \frac{c}{\omega} \sqrt{\left| \frac{\omega}{ck_z} \right|} \delta\left(\frac{\omega}{c} - \frac{\omega'}{c}\right) \frac{\partial_\theta Y_{\ell m}(\theta^\pm, \varphi)}{\sqrt{\ell(\ell+1)}}. \quad (2.47)$$

The two remaining matrix elements are given by

$$\langle \mathbf{k}, \omega, \pm, \text{TM} | \omega', \ell, m, M \rangle = -\langle \mathbf{k}, \omega, \pm, \text{TE} | \omega', \ell, m, E \rangle, \quad (2.48)$$

$$\langle \mathbf{k}, \omega, \pm, \text{TM} | \omega', \ell, m, E \rangle = \langle \mathbf{k}, \omega, \pm, \text{TE} | \omega', \ell, m, M \rangle. \quad (2.49)$$

In this chapter we have derived the essentials for the description of the Casimir effect in the plane–sphere geometry. The plane wave basis is well adapted for the propagation and the reflection at the plane, while the multipole basis is well adapted for the reflection at the sphere. Before we apply the

scattering formula to the plane–sphere geometry in chapter 5, we first study the reflection properties of electromagnetic waves at planes and spheres in the next chapter, and apply the scattering formula to the plane–plane geometry in chapter 4.

3. Reflection properties of metals

Most of the experiments probing the Casimir effect use metallic mirrors. In the last decades the accuracy of such experiments was drastically improved and for an accurate description it is thus essential to use a realistic description of the reflection properties of the metals. The reflection properties of metals are described in terms of the dielectric function $\epsilon(\omega)$. In this chapter, we introduce the Drude model that takes finite conductivity and plasma oscillations into account. We derive from the Drude model the plasma model which neglects effects due to dissipation, and the model for perfect reflectors that assumes perfect conductivity at arbitrary frequencies. Given the dielectric function $\epsilon(\omega)$, we present the solutions of the scattering of plane waves at a plane and a sphere.

3.1. Drude model

The Drude model is based on the assumption that the valence electrons are detached from the atoms and can move freely within the metal. Although we consider a quantum mechanical problem, we assume the electrons to be classical particles. We consider an electric field with harmonic time dependence

$$\mathbf{E}(t) = \mathbf{E}(\omega) e^{-i\omega t}. \quad (3.1)$$

The electric field (3.1) will cause the electrons to accelerate. If we also assume that there is some kind of linear dissipation, the velocity of an electron is described by

$$m_e \dot{\mathbf{v}} + \gamma m_e \mathbf{v} = -e \mathbf{E}, \quad (3.2)$$

where m_e is the (effective) mass of an electron and γ is called relaxation frequency. The steady-state solution is given by

$$\mathbf{v} = \frac{-e}{m_e(\gamma - i\omega)} \mathbf{E}. \quad (3.3)$$

In an isotropic and linear medium electric field and current density are parallel with the factor of proportionality given by the AC conductivity $\sigma(\omega)$. For the Drude model we find

$$\mathbf{j} \equiv \sigma(\omega) \mathbf{E}(\omega) = -n_e e \mathbf{v} = \frac{n_e e^2}{m_e(\gamma - i\omega)} \mathbf{E}, \quad (3.4)$$

where the AC conductivity is given by

$$\sigma(\omega) \equiv \frac{n_e e^2}{m_e(\gamma - i\omega)} = \frac{\sigma_0}{1 - \frac{i\omega}{\gamma}}, \quad \sigma_0 \equiv \sigma(\omega = 0) = \frac{n_e e^2}{m_e \gamma}. \quad (3.5)$$

The Maxwell equations inside the metal read

$$\nabla \cdot \mathbf{E} = 0, \quad \nabla \cdot \mathbf{B} = 0, \quad \nabla \times \mathbf{E} = -\frac{\partial \mathbf{B}}{\partial t}, \quad \nabla \times \mathbf{B} = \mu_0 \mathbf{j} + \epsilon_0 \mu_0 \frac{\partial \mathbf{E}}{\partial t}. \quad (3.6)$$

The electric field obeys the wave equation

$$\nabla \times (\nabla \times \mathbf{E}) = -\nabla^2 \mathbf{E} = -\frac{\partial}{\partial t} \left(\mu_0 \mathbf{j} + \frac{1}{c^2} \frac{\partial \mathbf{E}}{\partial t} \right) \equiv \frac{\omega^2}{c^2} \epsilon(\omega) \mathbf{E}, \quad (3.7)$$

where the complex dielectric function $\epsilon(\omega)$ is given by

$$\epsilon(\omega) \equiv 1 - \frac{\omega_p^2}{\omega(\omega + i\gamma)}, \quad \omega_p^2 \equiv \frac{n_e e^2}{\epsilon_0 m_e}. \quad (3.8)$$

If $\omega \gg \gamma$, the metal becomes transparent for frequencies greater than the plasma frequency ω_p . A more complete discussion of the properties of metals and the Drude model can be found in standard textbooks of solid state physics like [2].

When studying the Casimir effect, we will perform a Wick rotation and change the axis of integration to imaginary frequencies. The dielectric function is then evaluated at imaginary frequencies $\omega = i\xi$. We are thus lead to study the dielectric function for imaginary frequencies. For imaginary frequencies the dielectric function becomes a real-valued function

$$\epsilon(i\xi) = 1 + \frac{\omega_p^2}{\xi(\xi + \gamma)}. \quad (3.9)$$

The high and low frequency limits are given by

$$\epsilon(i\xi) \simeq 1 + \frac{\omega_p^2}{\xi^2} \quad \text{for } \xi \gg \gamma, \quad (3.10)$$

$$\epsilon(i\xi) \simeq \frac{\omega_p^2}{\gamma \xi} \quad \text{for } \xi \rightarrow 0. \quad (3.11)$$

3.2. Plasma model and perfect reflectors

The plasma model neglects effects due to dissipation and can be obtained from the Drude model by taking the limit $\gamma \rightarrow 0$. The dielectric function at imaginary frequencies becomes

$$\epsilon(i\xi) = 1 + \frac{\omega_p^2}{\xi^2} \quad (3.12)$$

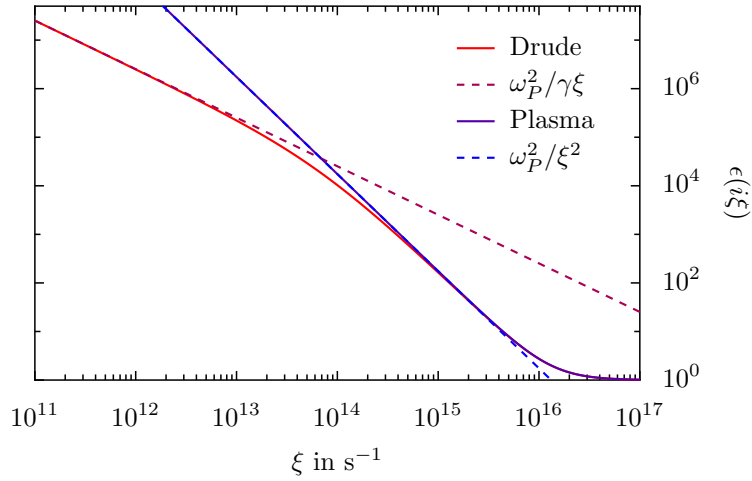


Figure 3.1.: Drude and plasma model with parameters $\omega_P = 1.32 \cdot 10^{16} \text{ s}^{-1}$, $\gamma = 6.90 \cdot 10^{13} \text{ s}^{-1}$ corresponding to silver [23]. The upper solid line corresponds to the plasma model, the lower solid line to the Drude model. The dashed lines correspond to the low frequency approximation of the Drude and plasma model. The dielectric functions for Drude and the plasma model are plotted together with the approximations (3.11) and (3.13) for imaginary frequencies.

and corresponds to the high frequency limit of the Drude model. In other words, Drude and plasma model agree for frequencies $\xi \gg \gamma$. The low frequency limit $\xi \ll \omega_P$ is given by

$$\epsilon(i\xi) \simeq \frac{\omega_P^2}{\xi^2}. \quad (3.13)$$

In Fig. 3.1 we show the dielectric functions of the Drude and plasma models and its approximations for imaginary frequencies.

The model of perfect reflectors can be obtained from the plasma model by taking the limit $\omega_P \rightarrow \infty$. The dielectric function $\epsilon(i\xi) = \infty$ is infinite at arbitrary frequencies.

3.3. Fresnel coefficients

The Fresnel coefficients are the reflection and transmission coefficients for an incident plane wave at a flat, planar and homogenous interface between dielectrics. In particular, we will consider a vacuum–metal interface at $z = 0$. The Fresnel coefficients are obtained by solving the boundary value problem at the interface. TE- and TM-polarization are well adapted to this boundary value problem and the reflection of a plane wave yields

$$|\mathbf{k}, \omega, -\phi, p\rangle_{\text{ref}} = r_p(\omega, \mathbf{k}) |\mathbf{k}, \omega, \phi, p\rangle_{\text{in}}. \quad (3.14)$$

The subscript “in” denotes the incident wave, the subscript “ref” the reflected wave. The frequency ω , the wave vector in the xy -plane \mathbf{k} , and the polarization $p = \text{TE, TM}$ remain constant during the scattering, but the direction of propagation changes. The reflection coefficient is given by the Fresnel coefficient r_p .

The Fresnel coefficients at imaginary frequencies $\omega = i\xi$ are [27]

$$r_{\text{TE}}(i\xi, k) = \frac{1 - \beta}{1 + \beta} \quad r_{\text{TM}}(i\xi, k) = \frac{\epsilon(i\xi) - \beta}{\epsilon(i\xi) + \beta}, \quad (3.15)$$

with the abbreviation

$$\beta = \sqrt{1 + \frac{\epsilon(i\xi) - 1}{\cos^2 \theta^\pm}}. \quad (3.16)$$

Because of the dispersion relation

$$k_z^2 = \frac{\omega^2}{c^2} - k^2 = -\frac{\xi^2}{c^2} - k^2, \quad (3.17)$$

the z -component of the wave vector k_z also becomes imaginary for imaginary frequencies. For this reason, we define

$$k_z \equiv i\kappa, \quad \kappa \equiv \sqrt{\frac{\xi^2}{c^2} + k^2}, \quad (3.18)$$

where $\kappa \in \mathbb{R}$. The relations (2.6) become

$$\sin \theta^\pm = -i \frac{ck}{\xi}, \quad \cos \theta^\pm = \pm \frac{c\kappa}{\xi}, \quad (3.19)$$

and we can express β in terms of ξ , κ and $\epsilon(i\xi)$:

$$\beta = \sqrt{1 + \frac{\xi^2}{c^2 \kappa^2} [\epsilon(i\xi) - 1]} \quad (3.20)$$

The Fresnel coefficients for perfect reflectors are obtained by taking the limit $\epsilon \rightarrow \infty$. The coefficients become

$$r_{\text{TM}}^{\text{perf}} = -r_{\text{TE}}^{\text{perf}} = 1. \quad (3.21)$$

and are independent of ξ and κ .

The properties of the Fresnel coefficients for low frequencies deserve a careful analysis for Drude and plasma mirrors. For $\xi \rightarrow 0$ the parameter β becomes in the Drude model

$$\beta^{\text{Drude}} = \sqrt{1 + \frac{\xi \omega_p^2}{c^2 \kappa (\xi + \gamma)}} \xrightarrow{\xi \rightarrow 0} 1. \quad (3.22)$$

3. Reflection properties of metals

The dielectric function diverges for $\xi \rightarrow 0$ and the Fresnel coefficients become

$$\lim_{\xi \rightarrow 0} r_{\text{TE}}^{\text{Drude}} = 0, \quad \lim_{\xi \rightarrow 0} r_{\text{TM}}^{\text{Drude}} = 1. \quad (3.23)$$

For Drude mirrors we see that the Fresnel coefficients become universal and independent of the particular properties of the metal for $\xi \rightarrow 0$. However, this is not true for the plasma model. In the plasma model the parameter β becomes

$$\beta^{\text{plasma}} = \sqrt{1 + \frac{\omega_p^2}{c^2 \kappa^2}} \xrightarrow{\xi \rightarrow 0} \sqrt{1 + \frac{\omega_p^2}{c^2 \kappa^2}} \quad (3.24)$$

and the Fresnel coefficients are given by

$$\lim_{\xi \rightarrow 0} r_{\text{TE}}^{\text{plasma}} = \frac{1 - \sqrt{1 + \frac{\omega_p^2}{c^2 \kappa^2}}}{1 + \sqrt{1 + \frac{\omega_p^2}{c^2 \kappa^2}}}, \quad \lim_{\xi \rightarrow 0} r_{\text{TM}}^{\text{plasma}} = 1. \quad (3.25)$$

In contrast to the Drude model, the Fresnel coefficient for the TE mode is not universal and still depends on κ and ω_p in the plasma model. For this reason, the limits $\xi \rightarrow 0$ and $\gamma \rightarrow 0$ do not interchange:

$$\lim_{\xi \rightarrow 0} \lim_{\gamma \rightarrow 0} r_{\text{TE}}^{\text{Drude}} = \lim_{\xi \rightarrow 0} r_{\text{TE}}^{\text{plasma}} = \frac{1 - \sqrt{1 + \frac{\omega_p^2}{c^2 \kappa^2}}}{1 + \sqrt{1 + \frac{\omega_p^2}{c^2 \kappa^2}}} \quad (3.26)$$

$$\lim_{\gamma \rightarrow 0} \lim_{\xi \rightarrow 0} r_{\text{TE}}^{\text{Drude}} = 0 \quad (3.27)$$

However, the limits $\xi \rightarrow 0$ and $\omega_p \rightarrow \infty$ do interchange:

$$\lim_{\xi \rightarrow 0} \lim_{\omega_p \rightarrow \infty} r_{\text{TE}}^{\text{plasma}} = \lim_{\xi \rightarrow 0} r_{\text{TE}}^{\text{perf}} = -1 \quad (3.28)$$

$$\lim_{\omega_p \rightarrow \infty} \lim_{\xi \rightarrow 0} r_{\text{TE}}^{\text{plasma}} = \lim_{\omega_p \rightarrow \infty} \frac{1 - \sqrt{1 + \frac{\omega_p^2}{c^2 \kappa^2}}}{1 + \sqrt{1 + \frac{\omega_p^2}{c^2 \kappa^2}}} = -1 \quad (3.29)$$

This means that there is no continuous transition for the TE-Fresnel coefficient from the Drude to the plasma model. As a consequence, there is neither a continuous transition from the Drude to the plasma model, nor a continuous transition from the Drude model to the model of perfect reflectors in the Casimir effect. More precisely, we will see that the high temperature limits for perfect reflectors and Drude mirrors differ by a factor 2.

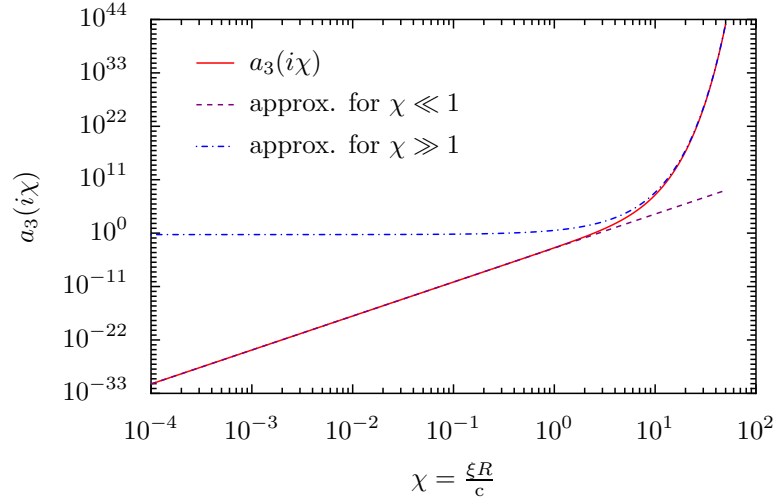


Figure 3.2.: The Mie coefficient $a_3(i\chi)$ with approximations. For small arguments the behaviour is polynomial, for large arguments it is exponential. The Mie coefficient covers about 80 orders of magnitude in the range $10^{-4} \leq \chi \leq 10^2$.

3.4. Mie coefficients

Mie scattering describes the scattering of electromagnetic waves by a sphere. The Mie coefficients for complex frequencies $\omega = i\xi$ are given by [6, 10, 13]

$$a_\ell(i\chi) = \frac{\pi}{2} \frac{n^2 s_\ell^{(a)} - s_\ell^{(b)}}{n^2 s_\ell^{(c)} - s_\ell^{(d)}}, \quad b_\ell(i\chi) = \frac{\pi}{2} \frac{s_\ell^{(a)} - s_\ell^{(b)}}{s_\ell^{(c)} - s_\ell^{(d)}}, \quad (3.30)$$

using the abbreviations

$$\begin{aligned} s_\ell^{(a)} &= I_{\ell+1/2}(n\chi) [I_{\ell+1/2}(\chi) - \chi I_{\ell-1/2}(\chi)], & s_\ell^{(b)} &= I_{\ell+1/2}(\chi) [I_{\ell+1/2}(n\chi) - n\chi I_{\ell-1/2}(n\chi)], \\ s_\ell^{(c)} &= I_{\ell+1/2}(n\chi) [K_{\ell+1/2}(\chi) + \chi K_{\ell-1/2}(\chi)], & s_\ell^{(d)} &= K_{\ell+1/2}(\chi) [I_{\ell+1/2}(n\chi) - n\chi I_{\ell-1/2}(n\chi)], \end{aligned} \quad (3.31)$$

where $n = \sqrt{\epsilon}$ is the refractive index of the sphere, and $\chi = \xi R/c$. The properties of the modified Bessel functions $I_\nu(x)$ and $K_\nu(x)$ are briefly described in appendix A.4. We also want to point out that the Mie coefficients are independent of \mathbf{k} and m , which is a consequence of the rotational symmetry.

We obtain the Mie coefficients for perfect reflectors by taking the limit $\epsilon \rightarrow \infty$ and find

$$a_\ell^{\text{perf}}(i\chi) = \frac{\pi}{2} (-1)^{\ell+1} \frac{\ell I_{\ell+1/2}(\chi) - \chi I_{\ell-1/2}(\chi)}{\ell K_{\ell+1/2}(\chi) + \chi K_{\ell-1/2}(\chi)}, \quad (3.32)$$

$$b_\ell^{\text{perf}}(i\chi) = \frac{\pi}{2} (-1)^{\ell+1} \frac{I_{\ell+1/2}(\chi)}{K_{\ell+1/2}(\chi)}. \quad (3.33)$$

For low frequencies $\xi R \ll c$, the Mie coefficients a_ℓ and b_ℓ can be simplified using the approximations

3. Reflection properties of metals

of the Bessel functions (A.21)

$$a_\ell^{\text{perf}} \simeq a_{\ell,0}^{\text{perf}} \left(\frac{\chi}{2}\right)^{2\ell+1}, \quad b_\ell^{\text{perf}} \simeq b_{\ell,0}^{\text{perf}} \left(\frac{\chi}{2}\right)^{2\ell+1}, \quad (3.34)$$

where

$$a_{\ell,0}^{\text{perf}} \equiv (-1)^\ell \frac{\pi \left(1 + \frac{1}{\ell}\right)}{\Gamma\left(\ell + \frac{1}{2}\right) \Gamma\left(\ell + \frac{3}{2}\right)}, \quad b_{\ell,0}^{\text{perf}} \equiv (-1)^{\ell+1} \frac{\pi}{\Gamma\left(\ell + \frac{1}{2}\right) \Gamma\left(\ell + \frac{3}{2}\right)}. \quad (3.35)$$

For high frequencies $\xi R \gg c$, the Mie coefficients can be approximated using (A.22)

$$a_\ell(i\chi) \simeq (-1)^\ell \frac{(\chi - \ell)e^{2\chi}}{2(\chi + \ell)} \stackrel{\chi \gg \ell}{\simeq} (-1)^\ell \frac{e^{2\chi}}{2}, \quad b_\ell(i\chi) \simeq (-1)^{\ell+1} \frac{e^{2\chi}}{2}. \quad (3.36)$$

We see that for low frequencies the Mie coefficients show polynomial, and for high frequencies exponential behaviour. Fig. 3.2 shows the Mie coefficient a_3 along with its high and low frequency approximations.

4. The scattering formula in the plane–plane geometry

In his original paper of 1984 [14], Casimir considered two parallel, perfectly conducting plates in vacuum at temperature $T = 0$ and found an attracting force due to vacuum fluctuations. Before we investigate the Casimir effect in the experimental more relevant plane–sphere configuration in the next chapter, we first apply the scattering formula to the much simpler plane–plane geometry. We will rederive Casimir’s famous formula, and also derive expressions for lossy Drude metals at nonzero temperatures. However, this chapter is not only of educational value, but we will use the results in chapter 7 for the description of the plane–sphere configuration in the proximity force approximation (PFA).

We consider two parallel plates which are infinite in the x - and y -directions and separated by a distance d . The lower plate is labeled as plate 1, the upper plate is labeled as plate 2. We also assume that the plates are thick enough to be considered as a bulk. This way, we may describe the dielectric function by the Drude, plasma or perfect reflectors model, and the reflection coefficients are given by the Fresnel coefficients. However, we will only consider Drude and perfect mirrors here.

4.1. Round-trip operator

The scattering approach is described in many publications with different focus on geometry, finite conductivity and temperature [10, 11, 13, 25, 32, 34, 44, 45]. The Casimir free energy is given as a sum over the Matsubara frequencies ω_n

$$\mathcal{F} = k_B T \sum_{n=0}^{\infty}{}' \ln \det \mathcal{D}(\omega_n), \quad \omega_n = \frac{2\pi n k_B T}{\hbar}, \quad (4.1)$$

where \mathcal{D} is the scattering operator and the primed sum indicates that the $n = 0$ term is weighted by $1/2$. The configuration is time-invariant, thus the frequency ω is preserved during scattering processes and the scattering operator is block diagonal with respect to ω . The scattering operator is related to the round-trip operator \mathcal{M} by

$$\mathcal{D}(\omega) = \mathbb{1} - \mathcal{M}(\omega). \quad (4.2)$$

The round-trip operator \mathcal{M} consists of the reflection operator at plane 1, the translation operator from plane 1 to plane 2, the reflection operator at plane 2, and the translation operator from plane 2 to

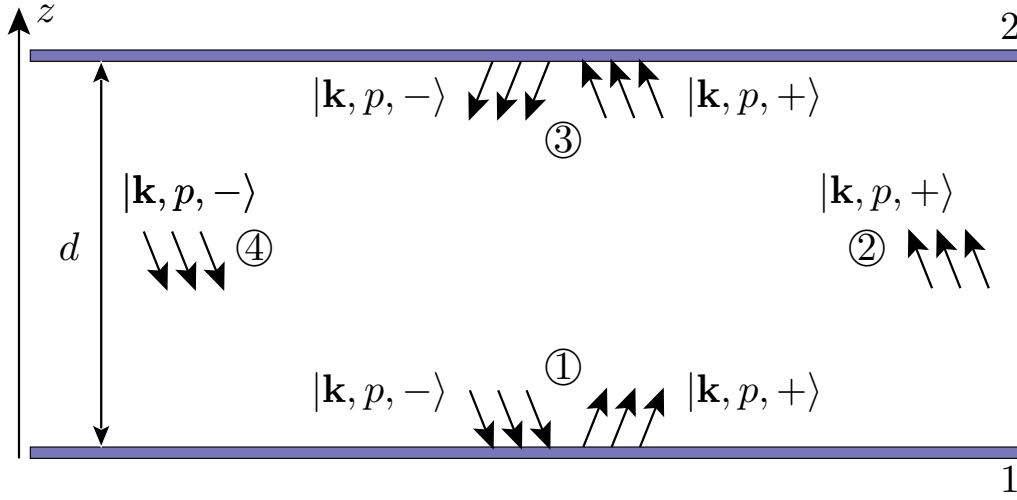


Figure 4.1.: The matrix \mathcal{M} describes a round trip within the cavity: ① The reflection on plane 1 yields the Fresnel coefficient r_p , ② the translation from plane 1 to plane 2 yields a phase factor $e^{ik_z d}$, ③ the reflection on plane 2 yields another Fresnel coefficient r_p , and ④ the translation back to plane 1 yields a second phase factor $e^{ik_z d}$.

plane 1

$$\mathcal{M} = \mathcal{T}_{1 \leftarrow 2} \mathcal{R}_2 \mathcal{T}_{2 \leftarrow 1} \mathcal{R}_1. \quad (4.3)$$

The operator \mathcal{M} thus corresponds to one round trip within the cavity. In a way, the scattering operator \mathcal{D} can be interpreted as the difference between doing a round trip and not doing a round trip [10]. The reader might note that the round-trip operator is only unique up to cyclic permutations. However, it follows from SYLVESTER’S determinant theorem

$$\det(\mathbb{1} - AB) = \det(\mathbb{1} - BA) \quad (4.4)$$

that the free energy \mathcal{F} is invariant under permutations.

The translation and the reflection operators of the plates are diagonal in the plane wave basis, because its basis functions are eigenfunctions of the momentum operator. The reflection of plane waves at a plane preserves the transverse wave vector and the polarization, but changes the direction of propagation:

$$\mathcal{R}_1 |\mathbf{k}, p, +\rangle = 0 \quad \mathcal{R}_2 |\mathbf{k}, p, +\rangle = r_p^{(2)}(\omega, k) |\mathbf{k}, p, -\rangle \quad (4.5)$$

$$\mathcal{R}_1 |\mathbf{k}, p, -\rangle = r_p^{(1)}(\omega, k) |\mathbf{k}, p, +\rangle \quad \mathcal{R}_2 |\mathbf{k}, p, -\rangle = 0 \quad (4.6)$$

The coefficients are given by the Fresnel coefficients $r_p(\omega, k)$. For the sake of simplicity, we assume that both plates have identical optical properties and set $r_p \equiv r_p^{(1)} = r_p^{(2)}$. However, the generalization to different Fresnel coefficients causes no problems. The translation operators are also diagonal in the

plane wave basis

$$\mathcal{T}_{2 \leftarrow 1} |\mathbf{k}, p, \phi\rangle = e^{i\phi k_z d} |\mathbf{k}, p, \phi\rangle, \quad \mathcal{T}_{1 \leftarrow 2} |\mathbf{k}, p, \phi\rangle = e^{-i\phi k_z d} |\mathbf{k}, p, \phi\rangle, \quad (4.7)$$

and yield a phase factor dependent on the direction of propagation.

We now derive the matrix elements of \mathcal{M} in the plane wave basis. The round-trip operator acting on a plane wave propagating in upward direction yields

$$\mathcal{M} |\mathbf{k}, p, +\rangle = \mathcal{T}_{1 \leftarrow 2} \mathcal{R}_2 \mathcal{T}_{2 \leftarrow 1} \mathcal{R}_1 |\mathbf{k}, p, +\rangle = 0. \quad (4.8)$$

For a plane wave propagating in downward direction, we find

$$\mathcal{M} |\mathbf{k}, p, -\rangle = \mathcal{T}_{1 \leftarrow 2} \mathcal{R}_2 \mathcal{T}_{2 \leftarrow 1} \mathcal{R}_1 |\mathbf{k}, p, -\rangle = r_p^2(\omega, k) e^{2ik_z d} |\mathbf{k}, p, -\rangle. \quad (4.9)$$

We see that the round-trip operator is diagonal in the plane wave basis. The transverse wave vector and the polarization remain spectators within a round trip. The round trip is illustrated in Fig. 4.1.

4.2. Free energy

As the round-trip operator is diagonal in the plane wave basis, the determinant is given by the product of the diagonal matrix elements. Thus the product is given as a sum

$$\ln \det \mathcal{D}(\omega) = \ln \prod_{\mathbf{k}, p} (1 - r_p^2 e^{2ik_z d}) = \sum_{\mathbf{k}, p} \ln(1 - r_p^2 e^{2ik_z d}) \quad (4.10)$$

over the polarizations $p = \text{TE, TM}$ and the wave vectors

$$k_{x,y} = \frac{2\pi n_{x,y}}{L_{x,y}}, \quad n_{x,y} \in \mathbb{Z}. \quad (4.11)$$

Eq. (4.11) can be deduced using box quantization and L_x, L_y correspond to the lengths of the plates in x - and y -direction. When the area $A \equiv L_x L_y$ of the plates tends to infinity, the summation over the wave vectors becomes dense and we can replace the sum by an integral [50]

$$\sum_{\mathbf{k}} \rightarrow \frac{A}{(2\pi)^2} \int d^2 \mathbf{k} = \frac{A}{(2\pi)^2} \int_0^\infty dk k \int_0^{2\pi} d\varphi_k = \frac{A}{2\pi} \int_0^\infty dk k. \quad (4.12)$$

The Fresnel coefficients as well as the phase factor depend on k only and therefore the integration over φ_k yields 2π . The logarithm of the determinant of the scattering operator simplifies to an integration over k

$$\ln \det \mathcal{D}(\omega) = \frac{A}{2\pi} \int_0^\infty dk k \ln \left[(1 - r_{\text{TE}}^2 e^{2ik_z d}) (1 - r_{\text{TM}}^2 e^{2ik_z d}) \right]. \quad (4.13)$$

4. The scattering formula in the plane-plane geometry

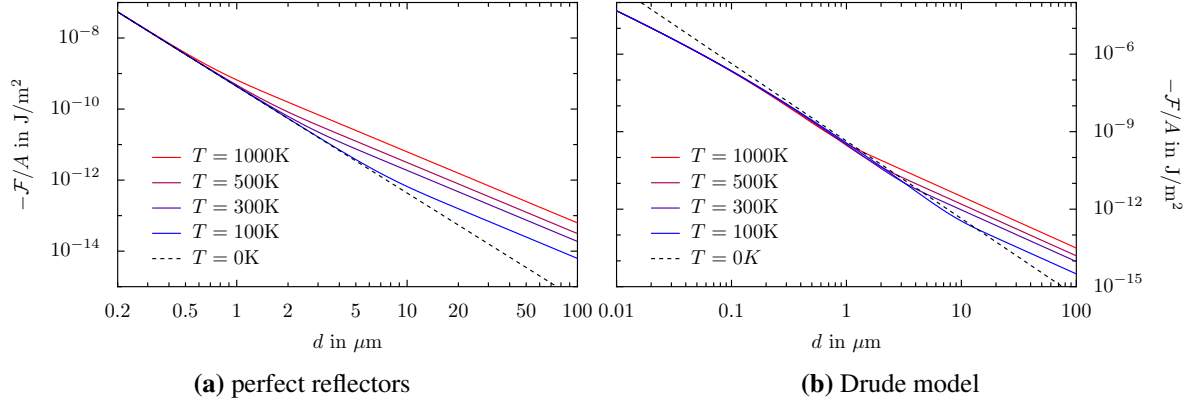


Figure 4.2.: The Casimir free energy for different temperatures for a) perfect reflectors and b) Drude metals. The values of the parameters for the Drude model are $\omega_p = 1.385 \cdot 10^{16} \text{s}^{-1}$, $\gamma = 5.54 \cdot 10^{13} \text{s}^{-1}$ and correspond to gold. The dashed lines correspond to $T = 0$ for perfect reflectors in both plots.

The integral (4.13) is an oscillatory integral and hard to evaluate numerically. As the integrand is analytic in the upper complex half-space [19], we can change the axis of integration according to CAUCHY's integral theorem to imaginary frequencies $\omega = i\xi$, where $\xi \in \mathbb{R}$. We will use the definitions $k_z \equiv i\kappa$ and $\kappa \equiv \sqrt{\xi^2/c^2 + k^2}$ that we have introduced in section 3.3. This Wick rotation changes $\omega \rightarrow i\xi$ and $k_z \rightarrow i\kappa$ in (4.13). After the Wick rotation, the free energy at finite temperature can be written as

$$\frac{\mathcal{F}}{A} = \frac{k_B T}{2\pi} \sum_{n=0}^{\infty} \int_{\xi_n/c}^{\infty} d\kappa \kappa \ln[(1 - \rho_{TE})(1 - \rho_{TM})], \quad \rho_p(\xi, \kappa) = r_p^2(i\xi_n, \kappa) e^{-2\kappa d}. \quad (4.14)$$

The integrand is now damped by an exponential factor which ensures fast convergence of the integral. The Fresnel coefficient r_p depends on the dielectric function $\epsilon(i\xi)$ of the metal. Eq. (4.14) has a wide range of validity: We have made no assumptions on the reflection coefficients r_p . The dielectric function may be given by the Drude or plasma model, the model of perfect reflectors or from experimental data. We will consider Drude and perfect mirrors in the following sections.

4.3. Perfect reflectors

For perfect reflectors integral (4.14) can be computed analytically. The Fresnel coefficients for perfect reflectors are given by $r_{TM} = -r_{TE} = 1$. After substituting $t = 2\kappa d$ the free energy becomes

$$\frac{\mathcal{F}^{\text{perf}}}{A} = \frac{k_B T}{4\pi d^2} \sum_n \int_{2\xi_n d/c}^{\infty} dt t \ln(1 - e^{-t}) \quad (4.15)$$

and the integral can be evaluated in terms of the polylogarithms Li_2 and Li_3

$$\frac{\mathcal{F}^{\text{perf}}}{A} = -\frac{k_B T}{4\pi d^2} \sum_n \left[\text{Li}_3 \left(e^{-2\xi_n d/c} \right) + \frac{2\xi_n d}{c} \text{Li}_2 \left(e^{-2\xi_n d/c} \right) \right]. \quad (4.16)$$

A short description about basic properties of polylogarithms can be found in appendix A.5. As the Matsubara frequency is proportional to nT , the argument of the polylogarithms becomes small for high temperatures. For small arguments the polylogarithms may be approximated by $\text{Li}_s(x) \simeq x$. In the high temperature limit the contributions to the free energy become negligible for $n > 0$ and we find for the free energy

$$\frac{\mathcal{F}_{\text{HT}}^{\text{perf}}}{A} = -\frac{k_B T \zeta(3)}{8\pi d^2} \quad \text{for } \lambda_T \ll 2\pi d, \quad (4.17)$$

where ζ is the Riemann zeta function, $\zeta(3) = \text{Li}_3(1) \approx 1.20206$, and $\lambda_T = \hbar c/(k_B T)$ is the thermal wavelength. For temperature $T = 0$ the sum becomes dense and we can replace it by an integral

$$k_B T \sum_n \rightarrow \hbar \int_0^\infty \frac{d\xi}{2\pi}. \quad (4.18)$$

This integral can also be evaluated analytically and we find Casimir's famous formula

$$\frac{\mathcal{F}_{T=0}^{\text{perf}}}{A} = -\frac{\pi^2 \hbar c}{720 d^3}. \quad (4.19)$$

This expression is remarkable as it only depends on fundamental constants like the Planck constant \hbar , the speed of light c , and the separation between the plates d . In particular, this result seems to be independent of the fine structure constant α . However, this is just an artefact of the idealized description of the metals as perfect reflectors [28].

In Fig. 4.2 a) the Casimir free energy for perfect reflectors dependent on the separation d is plotted for different temperatures. The dashed line corresponds to the zero temperature limit. For small separations the free energy coincides with the zero temperature limit. In general, the absolute value of the free energy increases with increasing temperature.

4.4. Drude mirrors

Real metals show a more complicated behaviour. The qualitative effect can be understood by a simple argument. Due to finite conductivity, electromagnetic waves are able to penetrate the metal. This effect is known as skin effect and the penetration depth δ is called skin depth. The skin depth increases the effective distance between the two plates to $d_{\text{eff}} \approx d + 2\delta$. Thus we expect the absolute value of the Casimir free energy to be smaller for Drude metals than for perfect mirrors. Small separations of the plates correspond to high temperatures and thus high frequencies at which the mirrors become

transparent. The penetration depth becomes large and the free energy deviates from the result for perfect mirrors [28].

For high temperatures it is sufficient to consider only the $n = 0$ term. In this case the Matsubara frequency is $\xi_0 = 0$ and the Fresnel coefficients become $r_{\text{TE}} = 0$ and $r_{\text{TM}} = 1$. Then (4.14) can be solved analytically and we obtain

$$\frac{\mathcal{F}_{\text{HT}}^{\text{Drude}}}{A} = -\frac{k_{\text{B}}T\zeta(3)}{16\pi d^2}, \quad (4.20)$$

which differs by a factor 2 from the result for perfect reflectors. This is a consequence of the different behaviour of the Fresnel coefficient for the TE mode: For Drude mirrors the reflection coefficient is $r_{\text{TE}} = 0$, while it is $r_{\text{TE}} = -1$ for perfect mirrors.

Fig. 4.2 b) shows the free energy for Drude mirrors dependent on the separation d for different temperatures. The dashed line corresponds to the zero temperature limit for perfect reflectors. For small separations the free energy differs from the zero temperature limit for perfect reflectors because of plasma oscillations.

4.5. Entropy

The entropy can be derived from the free energy by

$$S = -\frac{\partial \mathcal{F}}{\partial T}. \quad (4.21)$$

While the entropy is non-negative for perfect reflectors, we find negative values of the entropy in the Drude model over a wide separation distance range and for not too high temperatures. Fig. 4.3 shows negative entropies dependent on temperature and separation in the Drude model. We will delay the discussion of the physical implications of negative entropies and come back to this question in chapter 10. We just notice at this point that parameters for which the entropy becomes negative exist in the plane–plane geometry for Drude mirrors.

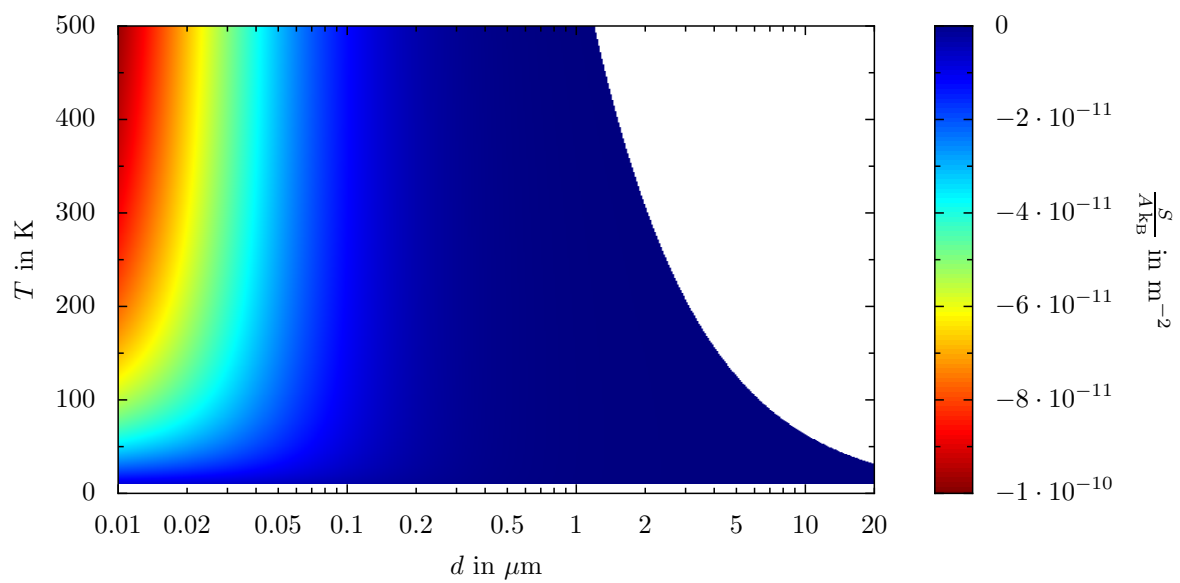


Figure 4.3.: Negative Casimir entropy dependent on temperature T and separation d in the Drude model in the range $11\text{K} \leq T \leq 499\text{K}$ and $0.01\mu\text{m} \leq d \leq 20\mu\text{m}$. White areas in this range correspond to positive entropies. While we find parameters for which the entropy is negative, the third law of thermodynamics is not violated as $S(T \rightarrow 0) \rightarrow 0$. The material parameters in this plot are those of gold: $\omega_P = 1.385 \cdot 10^{16} \text{ s}^{-1}$, $\gamma = 5.54 \cdot 10^{13} \text{ s}^{-1}$

5. The scattering formula in the plane–sphere geometry

In this chapter, we apply the scattering formula to the plane–sphere geometry. The plate is located at $z = 0$ and assumed to be infinite in the xy -plane. The center of the sphere is located above the plate at $z = L + R \equiv \mathcal{L}$, where R is the radius of the sphere and L is the distance between the plate and the sphere. The geometry is shown in Fig. 5.1. Moreover, we assume plate and sphere to be thick enough to be considered as bulk.

We derive the matrix elements of the scattering operator in the multipole basis and perform a Wick rotation. The free energy \mathcal{F} depends on the temperature, the reflection properties of the plate and the sphere, the sphere’s radius R and the separation L . We study the contribution to the free energy for the Matsubara frequency $\xi = 0$ in more detail, because the numerical evaluation causes problems. Given the free energy $\mathcal{F}(L, T)$, we can derive the force F and the entropy S from

$$F = -\frac{\partial \mathcal{F}}{\partial L}, \quad S = -\frac{\partial \mathcal{F}}{\partial T}. \quad (5.1)$$

We follow the reasoning of DURAND et al. [10, 13] to derive the matrix elements of the round-trip operator. However, we want to be more rigorous and explicit in our line of argumentation. Although equivalent, our matrix elements will differ from those of DURAND et al. and avoid Wigner (small) d-matrix elements. Moreover, the matrix elements have symmetries that can be exploited to decrease computational effort.

The Casimir effect in the plane–sphere geometry contains five length scales: the geometrical scales L and R , the thermal wavelength $\lambda_T = \hbar c / k_B T$, the plasma wavelength $\lambda_P = 2\pi c / \omega_P$, and the wavelength $\lambda_\gamma = 2\pi c / \gamma$ associated with the finite conductivity of the metals. We scale the quantities involved and show that only four length scales are independent. In particular, the free energy for perfect mirrors depends only on the temperature and the ratio of L and R : $\mathcal{F} = \mathcal{F}(T, L/R)$. In the last section, we give a conclusion and present the results of this chapter in condensed form.

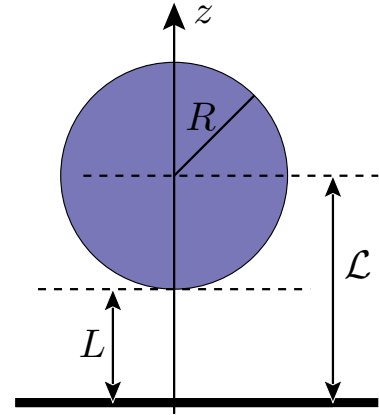


Figure 5.1.: Sphere of radius R and plate separated by a distance L with center-to-plate distance $\mathcal{L} \equiv L + R$.

5.1. Round-trip operator \mathcal{M}

In the plane–sphere geometry, the round-trip operator consists of the translation operator from sphere to plane $\mathcal{T}_{\text{P} \leftarrow \text{S}}$, the reflection operator at the plane \mathcal{R}_{P} , the translation operator from plane to sphere $\mathcal{T}_{\text{S} \leftarrow \text{P}}$, and the reflection operator at the sphere \mathcal{R}_{S} :

$$\mathcal{M}(\omega) = \mathcal{R}_{\text{S}}(\omega) \mathcal{T}_{\text{S} \leftarrow \text{P}}(\omega) \mathcal{R}_{\text{P}}(\omega) \mathcal{T}_{\text{P} \leftarrow \text{S}}(\omega) \quad (5.2)$$

The round-trip operator represents a round trip within the cavity. Except for the temperature, \mathcal{M} contains the whole information about the physical system: The separation L of sphere and plate affects the translation operators $\mathcal{T}_{\text{S} \leftarrow \text{P}}$ and $\mathcal{T}_{\text{P} \leftarrow \text{S}}$, the radius R of the sphere and the reflection properties of the sphere enter the reflection operator \mathcal{R}_{S} , and the reflection properties of the plane enter \mathcal{R}_{P} .

Before we express the round-trip operator in the multipole basis, let us first take a closer look at the symmetries of the plane–sphere configuration: The configuration is time invariant, so the frequency ω is preserved during a round trip. Moreover, the geometry is invariant under rotations around the z -axis and the round-trip operator \mathcal{M} commutes with the angular momentum operator \hat{J}_z . Therefore, the round-trip operator \mathcal{M} is block-diagonal with respect to m and each block $\mathcal{M}^{(m)}$ yields an independent contribution to the free energy

$$\mathcal{F} = k_{\text{B}} T \sum_{n=0}^{\infty} \sum_{m=-\infty}^{\infty} \ln \det [\mathbb{1} - \mathcal{M}^{(m)}(\omega)]. \quad (5.3)$$

The conservation of m is discussed in more detail in appendix B.2.

5.2. Round-trip operator in multipole basis

We want to express the matrix elements of \mathcal{M} in the multipole basis. The multipole basis is well adapted to the rotational symmetry around the z -axis and \mathcal{M} is block diagonal with respect to m . Although infinite, the rows and columns of the round-trip matrix are countable. The round-trip operator in the multipole basis reads

$$\mathcal{M}_{(\ell_1, P_1; \ell_2, P_2)}^{(m)}(\omega) = \langle \ell_1, m, P_1 | \mathcal{R}_{\text{S}} \mathcal{T}_{\text{S} \leftarrow \text{P}} \mathcal{R}_{\text{P}} \mathcal{T}_{\text{P} \leftarrow \text{S}} | \ell_2, m, P_2 \rangle. \quad (5.4)$$

When acting on plane waves, the translation operators yield phase factors

$$\mathcal{T}_{\text{P} \leftarrow \text{S}} | \mathbf{k}, p, \phi \rangle = e^{-i\phi k_z \mathcal{L}} | \mathbf{k}, p, \phi \rangle, \quad \mathcal{T}_{\text{S} \leftarrow \text{P}} | \mathbf{k}, p, \phi \rangle = e^{+i\phi k_z \mathcal{L}} | \mathbf{k}, p, \phi \rangle, \quad (5.5)$$

that depend on the direction of propagation. The reflection operator at the plane yields

$$\mathcal{R}_{\text{P}} | \mathbf{k}, p, + \rangle = 0, \quad \mathcal{R}_{\text{P}} | \mathbf{k}, p, - \rangle = r_p(\omega, \mathbf{k}) | \mathbf{k}, p, + \rangle, \quad (5.6)$$

where r_p is a Fresnel coefficient.

5. The scattering formula in the plane–sphere geometry

Let us insert the identity operator in the plane wave basis in (5.4) and evaluate the propagation from sphere to plate:

$$\mathcal{M}_{(\ell_1, P_1; \ell_2, P_2)}^{(m)}(\omega) = \sum_{p, \phi} \int d^2 \mathbf{k} e^{-\phi i k_z \mathcal{L}} \langle \ell_1, m, P_1 | \mathcal{R}_S \mathcal{T}_{S \leftarrow P} \mathcal{R}_P | \mathbf{k}, p, \phi \rangle \langle \mathbf{k}, p, \phi | \ell_2, m, P_2 \rangle \quad (5.7)$$

The reflection operator \mathcal{R}_p yields only a nonvanishing term for waves travelling in downward direction. Therefore, the sum over ϕ has only one contribution for $\phi = -1$ and the reflection operator introduces the Fresnel coefficient r_p . The evaluation of the translation operator yields another phase factor and we find

$$\mathcal{M}_{(\ell_1, P_1; \ell_2, P_2)}^{(m)}(\omega) = \sum_p \int d^2 \mathbf{k} r_p(\omega, \mathbf{k}) e^{2i k_z \mathcal{L}} \langle \ell_1, m, P_1 | \mathcal{R}_S | \mathbf{k}, p, + \rangle \langle \mathbf{k}, p, - | \ell_2, m, P_2 \rangle. \quad (5.8)$$

By inserting the identity operator in multipole basis, we get

$$\begin{aligned} \langle \ell, m, P | \mathcal{R}_S | \mathbf{k}, +, p \rangle &= \sum_{\ell'=1}^{\infty} \sum_{m'=-\ell'}^{\ell'} \sum_{P'=E, M} \langle \ell, m, P | \mathcal{R}_S | \ell', m', P' \rangle \langle \ell', m', P' | \mathbf{k}, +, p \rangle \\ &= \langle \ell, m, P | \mathcal{R}_S | \ell, m, P \rangle \langle \ell, m, P | \mathbf{k}, +, p \rangle. \end{aligned} \quad (5.9)$$

The operator \mathcal{R}_S is diagonal in the multipole basis with matrix elements proportional to the Mie coefficients a_ℓ and b_ℓ . The matrix elements of \mathcal{R}_S are given by

$$\langle \ell, m, E | \mathcal{R}_S | \ell, m, E \rangle = -2a_\ell(\omega), \quad \langle \ell, m, M | \mathcal{R}_S | \ell, m, M \rangle = -2b_\ell(\omega), \quad (5.10)$$

where we have used the definition of BOHREN and HUFFMAN for the Mie coefficients a_ℓ , b_ℓ [6]. The reader finds a discussion of the origin of the factor -2 in appendix B.8. We also want to point out that the Mie coefficients only depend on ℓ and the frequency ω , but not on m or \mathbf{k} .

In conclusion, we find for the matrix elements of the round-trip operator

$$\begin{aligned} \mathcal{M}_{(\ell_1, P_1; \ell_2, P_2)}^{(m)}(\omega) &= \sum_{p=\text{TE, TM}} \int d^2 \mathbf{k} r_p(\omega, \mathbf{k}) e^{2i k_z \mathcal{L}} \langle \ell_1, m, P_1 | \mathcal{R}_S | \ell_1, m, P_1 \rangle \\ &\quad \times \langle \ell_1, m, P_1 | \mathbf{k}, p, + \rangle \langle \mathbf{k}, p, - | \ell_2, m, P_2 \rangle \end{aligned} \quad (5.11)$$

and organize the round-trip matrix as a block matrix:

$$\mathcal{M}^{(m)}(\omega) = \begin{pmatrix} \mathcal{M}^{(m)}(E, E) & \mathcal{M}^{(m)}(E, M) \\ \mathcal{M}^{(m)}(M, E) & \mathcal{M}^{(m)}(M, M) \end{pmatrix} \quad (5.12)$$

Eq. (5.11) has a simple interpretation when read from right to left (cf. Fig. 5.2):

- ① $\langle \mathbf{k}, p, - | \ell_2, m, P_2 \rangle$: The multipole wave $|\ell_2, m, P_2\rangle$ is decomposed into plane waves.

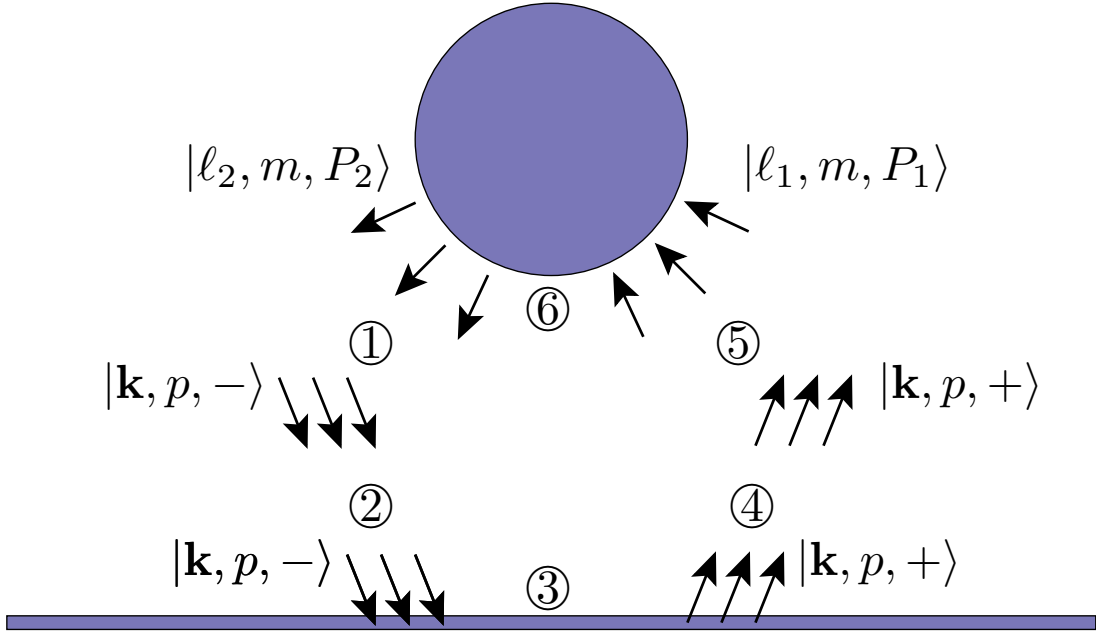


Figure 5.2.: Visualization of the components of the matrix elements of M in (5.11). Plane waves are used for propagation and reflection at the plate, multipole waves are used for the reflection at the sphere. (cf. [10])

- ② $e^{ik_z\mathcal{L}}$: The plane waves $|\mathbf{k}, -, p\rangle$ propagate the distance \mathcal{L} towards the plate. The propagation yields a phase factor $e^{ik_z\mathcal{L}}$.
- ③ $r_p(\omega, \mathbf{k})$: The plane waves $|\mathbf{k}, p, -\rangle$ are reflected at the plate. The reflection preserves the wave vector \mathbf{k} and the polarization p , but changes the direction of propagation. The reflection coefficient is given by the Fresnel coefficient r_p .
- ④ $e^{ik_z\mathcal{L}}$: The plane waves $|\mathbf{k}, +, p\rangle$ propagate the distance \mathcal{L} towards the sphere.
- ⑤ $\langle \ell_1, m, P_1 | \mathbf{k}, p, + \rangle$: The plane waves $|\mathbf{k}, +, p\rangle$ are decomposed into multipole waves $|\ell_1, m, P_1\rangle$.
- ⑥ $\langle \ell_1, m, P_1 | \mathcal{R}_S | \ell_1, m, P_1 \rangle$: The multipole waves are reflected at the sphere. The reflection preserves the polarization, the total angular momentum and the z -component of the angular momentum. In conclusion, the quantum numbers ℓ, m and P_1 are preserved.

5.3. Matrix elements in multipole basis

In this chapter, we derive explicit matrix elements for the scattering matrix. We substitute the spherical harmonics in the matrix elements performing the change of basis (2.46)–(2.49) by associated Legendre

5. The scattering formula in the plane–sphere geometry

polynomials:

$$Y_{\ell m}(\theta^\pm, \varphi) = N_{\ell m} P_\ell^m(\cos \theta^\pm) \frac{e^{im\varphi}}{\sqrt{2\pi}} = N_{\ell m} P_\ell^m\left(\pm \frac{ck_z}{\omega}\right) \frac{e^{im\varphi}}{\sqrt{2\pi}} \quad (5.13)$$

$$\partial_\theta Y_{\ell m}(\theta^\pm, \varphi) = N_{\ell m} P_\ell^{m'}(\cos \theta^\pm)(-\sin \theta^\pm) \frac{e^{im\varphi}}{\sqrt{2\pi}} = -\frac{ck}{\omega} N_{\ell m} P_\ell^{m'}\left(\pm \frac{ck_z}{\omega}\right) \frac{e^{im\varphi}}{\sqrt{2\pi}} \quad (5.14)$$

Descriptions of the properties of spherical harmonics, associated Legendre polynomials, the phase convention we use, and the normalizing constant $N_{\ell m}$ can be found in the sections A.1 and A.2 of the appendix. As the geometry is invariant under rotations around the z -axis, the matrix elements become independent of φ . An integration over φ yields 2π and the matrix elements are given as an integral over k

$$\mathcal{M}^{(m)}(E, E)_{\ell_1 \ell_2} = \Lambda_{\ell_1 \ell_2}^{(m)} a_{\ell_1}(\omega) [A_{\ell_1 \ell_2, \text{TE}}^{(m)}(\omega) + B_{\ell_1 \ell_2, \text{TM}}^{(m)}(\omega)], \quad (5.15)$$

$$\mathcal{M}^{(m)}(M, M)_{\ell_1 \ell_2} = \Lambda_{\ell_1 \ell_2}^{(m)} b_{\ell_1}(\omega) [A_{\ell_1 \ell_2, \text{TM}}^{(m)}(\omega) + B_{\ell_1 \ell_2, \text{TE}}^{(m)}(\omega)], \quad (5.16)$$

$$\mathcal{M}^{(m)}(E, M)_{\ell_1 \ell_2} = \Lambda_{\ell_1 \ell_2}^{(m)} a_{\ell_1}(\omega) [C_{\ell_1 \ell_2, \text{TE}}^{(m)}(\omega) + D_{\ell_1 \ell_2, \text{TM}}^{(m)}(\omega)], \quad (5.17)$$

$$\mathcal{M}^{(m)}(M, E)_{\ell_1 \ell_2} = -\Lambda_{\ell_1 \ell_2}^{(m)} b_{\ell_1}(\omega) [C_{\ell_1 \ell_2, \text{TM}}^{(m)}(\omega) + D_{\ell_1 \ell_2, \text{TE}}^{(m)}(\omega)], \quad (5.18)$$

where we have defined the prefactor

$$\Lambda_{\ell_1 \ell_2}^{(m)} \equiv \frac{-2 N_{\ell_1 m} N_{\ell_2 m}}{\sqrt{\ell_1(\ell_1 + 1) \ell_2(\ell_2 + 1)}} = -\sqrt{\frac{(2\ell_1 + 1)(2\ell_2 + 1)(\ell_1 - m)!(\ell_2 - m)!}{(\ell_1 + m)!(\ell_2 + m)!\ell_1(\ell_1 + 1)\ell_2(\ell_2 + 1)}}, \quad (5.19)$$

and the integrals

$$A_{\ell_1 \ell_2, p}^{(m)}(\omega) \equiv \int_0^\infty dk \frac{m^2}{ck} \left| \frac{\omega}{k_z} \right| r_p(\omega, k) e^{2ik_z \mathcal{L}} P_{\ell_1}^m\left(\frac{ck_z}{\omega}\right) P_{\ell_2}^m\left(-\frac{ck_z}{\omega}\right), \quad (5.20)$$

$$B_{\ell_1 \ell_2, p}^{(m)}(\omega) \equiv \int_0^\infty dk \frac{c^3 k^3}{\omega^4} \left| \frac{\omega}{k_z} \right| r_p(\omega, k) e^{2ik_z \mathcal{L}} P_{\ell_1}^{m'}\left(\frac{ck_z}{\omega}\right) P_{\ell_2}^{m'}\left(-\frac{k_z}{\omega}\right), \quad (5.21)$$

$$C_{\ell_1 \ell_2, p}^{(m)}(\omega) \equiv \int_0^\infty dk \frac{imck}{\omega^2} \left| \frac{\omega}{k_z} \right| r_p(\omega, k) e^{2ik_z \mathcal{L}} P_{\ell_1}^m\left(\frac{ck_z}{\omega}\right) P_{\ell_2}^{m'}\left(-\frac{ck_z}{\omega}\right), \quad (5.22)$$

$$D_{\ell_1 \ell_2, p}^{(m)}(\omega) \equiv \int_0^\infty dk \frac{imck}{\omega^2} \left| \frac{\omega}{k_z} \right| r_p(\omega, k) e^{2ik_z \mathcal{L}} P_{\ell_1}^{m'}\left(\frac{ck_z}{\omega}\right) P_{\ell_2}^m\left(-\frac{ck_z}{\omega}\right). \quad (5.23)$$

The Mie coefficients a_ℓ, b_ℓ are placed in front of the integral, because they are independent of k . The reader is warned that the absolute value functions are important to account for evanescent waves: We integrate over k for a fixed value of ω . The absolute value of the z -component of the wavevector is given by $k_z = \sqrt{\omega^2/c^2 - k^2}$ and becomes imaginary for $k > \omega/c$. Moreover, in the next chapter we perform a Wick rotation and therefore ω will also become imaginary.

5.4. Wick rotation

In an analog manner to the Wick rotation in the plane–plane geometry in section 4.2, we rotate the axis of integration to imaginary frequencies. This Wick rotation changes $\omega \rightarrow i\xi$ and $k_z \rightarrow i\kappa$ in the integrands and the matrix elements of the round-trip matrix become

$$\mathcal{M}^{(m)}(E, E)_{\ell_1 \ell_2} = \Lambda_{\ell_1 \ell_2}^{(m)} a_{\ell_1}(i\xi) \left[A_{\ell_1 \ell_2, \text{TE}}^{(m)}(\xi) + B_{\ell_1 \ell_2, \text{TM}}^{(m)}(\xi) \right], \quad (5.24)$$

$$\mathcal{M}^{(m)}(M, M)_{\ell_1 \ell_2} = \Lambda_{\ell_1 \ell_2}^{(m)} b_{\ell_1}(i\xi) \left[A_{\ell_1 \ell_2, \text{TM}}^{(m)}(\xi) + B_{\ell_1 \ell_2, \text{TE}}^{(m)}(\xi) \right], \quad (5.25)$$

$$\mathcal{M}^{(m)}(E, M)_{\ell_1 \ell_2} = \Lambda_{\ell_1 \ell_2}^{(m)} a_{\ell_1}(i\xi) \left[C_{\ell_1 \ell_2, \text{TE}}^{(m)}(\xi) + D_{\ell_1 \ell_2, \text{TM}}^{(m)}(\xi) \right], \quad (5.26)$$

$$\mathcal{M}^{(m)}(M, E)_{\ell_1 \ell_2} = -\Lambda_{\ell_1 \ell_2}^{(m)} b_{\ell_1}(i\xi) \left[C_{\ell_1 \ell_2, \text{TM}}^{(m)}(\xi) + D_{\ell_1 \ell_2, \text{TE}}^{(m)}(\xi) \right], \quad (5.27)$$

with the integrals

$$A_{\ell_1 \ell_2, p}^{(m)}(\xi) = \frac{m^2 \xi}{c} \int_0^\infty dk \frac{1}{k\kappa} r_p(i\xi, k) e^{-2\kappa\mathcal{L}} P_{\ell_1}^m\left(\frac{\kappa c}{\xi}\right) P_{\ell_2}^m\left(-\frac{\kappa c}{\xi}\right), \quad (5.28)$$

$$B_{\ell_1 \ell_2, p}^{(m)}(\xi) = \frac{c^3}{\xi^3} \int_0^\infty dk \frac{k^3}{\kappa} r_p(i\xi, k) e^{-2\kappa\mathcal{L}} P_{\ell_1}^{m'}\left(\frac{\kappa c}{\xi}\right) P_{\ell_2}^{m'}\left(-\frac{\kappa c}{\xi}\right), \quad (5.29)$$

$$C_{\ell_1 \ell_2, p}^{(m)}(\xi) = -\frac{imc}{\xi} \int_0^\infty dk \frac{k}{\kappa} r_p(i\xi, k) e^{-2\kappa\mathcal{L}} P_{\ell_1}^m\left(\frac{\kappa c}{\xi}\right) P_{\ell_2}^{m'}\left(-\frac{\kappa c}{\xi}\right), \quad (5.30)$$

$$D_{\ell_1 \ell_2, p}^{(m)}(\xi) = -\frac{imc}{\xi} \int_0^\infty dk \frac{k}{\kappa} r_p(i\xi, k) e^{-2\kappa\mathcal{L}} P_{\ell_1}^{m'}\left(\frac{\kappa c}{\xi}\right) P_{\ell_2}^m\left(-\frac{\kappa c}{\xi}\right). \quad (5.31)$$

The integrals are damped by an exponential function which ensures fast convergence. The argument of the associated Legendre polynomials is given by $\kappa c/\xi \geq 1$. The Legendre polynomials can be generalized to arguments greater than unity by analytic continuation. However, for odd values of m the analytic continuation is only unique up to a phase factor ± 1 . Nonetheless, when multiplying two associated Legendre polynomials (or their derivatives) of the same order m , the phase factor cancels. Thus the values of the integrals are independent of the choice of the phase factor. A brief discussion about the analytic continuation can be found in appendix A.2.

Although the matrix elements of the round-trip operator look different than those of DURAND et al. [10, 13], the matrix elements are equivalent. In appendix B.4 we proof this equivalence for the matrix element $\mathcal{M}_{\text{TE}}^{(m)}(E, E)_{\ell_1 \ell_2}$. The proofs for the remaining matrix elements can be carried out in a similar manner.

5.5. Properties of the scattering matrix

In this section, we show useful properties of the scattering matrix and its matrix elements. We will show that the determinant of the scattering matrix is real and that the matrix elements can be written in terms of real quantities. Moreover, we investigate symmetries among the matrix elements that can be exploited to decrease computational effort.

5.5.1. Determinant of the scattering matrix

All quantities in the integrands of (5.28)–(5.31) are real except for the associated Legendre polynomials. The product of two associated Legendre polynomials or their derivatives for the same degree m are either real or pure imaginary for arguments $x \geq 1$. In appendix A.2 we show that for $x \geq 1$

$$\mathbf{P}_{\ell_1}^m(x)\mathbf{P}_{\ell_2}^m(x) \in \mathbb{R}, \quad \mathbf{P}_{\ell_1}^{m'}(x)\mathbf{P}_{\ell_2}^{m'}(x) \in \mathbb{R}, \quad \mathbf{P}_{\ell_1}^m(x)\mathbf{P}_{\ell_2}^{m'}(x) \in i\mathbb{R}. \quad (5.32)$$

Hence, the block matrices $A_{\ell_1\ell_2}^{(m)}$ and $B_{\ell_1\ell_2}^{(m)}$ are real, while $\mathcal{M}^{(m)}(E, M)$ and $\mathcal{M}^{(m)}(M, E)$ are pure imaginary. With (B.14) we can write the scattering matrix with real matrix elements

$$\det \mathcal{D}^{(m)} = \det \begin{pmatrix} \mathbb{1} - \mathcal{M}^{(m)}(E, E) & -\text{Im}[\mathcal{M}^{(m)}(E, M)] \\ \text{Im}[\mathcal{M}^{(m)}(M, E)] & \mathbb{1} - \mathcal{M}^{(m)}(M, M) \end{pmatrix}. \quad (5.33)$$

From this it follows immediately that the determinant is a real number. As the energy is a real quantity, it follows from a physical point of view that the determinant must be positive as well. However, we have not proven the last point.

5.5.2. Symmetries

The prefactor $\Lambda_{\ell_1\ell_2}^{(m)}$ is invariant when interchanging ℓ_1 and ℓ_2 . Using this symmetry together with the parity of the associated Legendre polynomials (cf. (A.10)), one can show that

$$A_{\ell_2\ell_1,p}^{(m)} = (-1)^{\ell_1+\ell_2} A_{\ell_1\ell_2,p}^{(m)}, \quad B_{\ell_2\ell_1,p}^{(m)} = (-1)^{\ell_1+\ell_2} B_{\ell_1\ell_2,p}^{(m)}, \quad D_{\ell_1\ell_2,p}^{(m)} = (-1)^{\ell_1+\ell_2+1} C_{\ell_2\ell_1,p}^{(m)}. \quad (5.34)$$

By exploiting these relations, it is sufficient to evaluate $N^2 + N$ integrals for a block matrix $\mathcal{M}^{(m)}(P_1, P_2)$ of dimension N instead of $2N^2$ integrals. If we consider perfect mirrors, the Fresnel coefficients are given by $r_{\text{TM}} = -r_{\text{TE}} = 1$ and integrals for different polarization $p = \text{TE}, \text{TM}$ differ only in sign

$$X_{\ell_1\ell_2,\text{TE}} = -X_{\ell_1\ell_2,\text{TM}}, \quad (5.35)$$

where $X = A, B, C, D$. Therefore, for perfect mirrors we just have to evaluate $(N^2 + N)/2$ integrals.

When changing from $m \rightarrow -m$ the prefactor Λ can be expressed as

$$\Lambda_{\ell_1\ell_2}^{(-m)} = \frac{(\ell_1 + m)! (\ell_2 + m)!}{(\ell_1 - m)! (\ell_2 - m)!} \Lambda_{\ell_1\ell_2}^{(m)}, \quad (5.36)$$

and the integrals (5.28)–(5.31) as

$$X_{\ell_1\ell_2}^{(-m)} = \pm \frac{(\ell_1 - m)! (\ell_2 - m)!}{(\ell_1 + m)! (\ell_2 + m)!} X_{\ell_1\ell_2}^{(m)}, \quad (5.37)$$

with $+$ for $X = A, B$ and $-$ for $X = C, D$. Indeed, we see that

$$\Lambda_{\ell_1\ell_2}^{(-m)} X_{\ell_1\ell_2}^{(-m)} = \pm \Lambda_{\ell_1\ell_2}^{(m)} X_{\ell_1\ell_2}^{(m)}. \quad (5.38)$$

Hence, the diagonal blocks of the round-trip matrix are invariant for $m \rightarrow -m$ while the nondiagonal blocks change sign:

$$\mathcal{M}^{(-m)}(\xi_n) = \begin{pmatrix} \mathcal{M}^{(m)}(E, E) & -\mathcal{M}^{(m)}(E, M) \\ -\mathcal{M}^{(m)}(M, E) & \mathcal{M}^{(m)}(M, M) \end{pmatrix} \quad (5.39)$$

However, the determinant of the matrix $\mathcal{D}^{(m)}$ is invariant for $m \rightarrow -m$ which is shown in appendix B.3. The summation over m in the formula for the free energy can thus be limited to non-negative values of m by weighting every term but $m = 0$ with a factor 2, and therefore the free energy becomes

$$\mathcal{F} = 2k_B T \sum_{n=0}^{\infty} \sum_{m=0}^{\infty} \ln \det [\mathbb{1} - \mathcal{M}^{(m)}(\xi_n)]. \quad (5.40)$$

Exploiting the properties of the scattering matrix we found in this section will help to significantly reduce the computational time in a numerical implementation.

5.6. Scaling

In this master thesis, we are more interested in effects due to geometry and temperature than in effects due to finite conductivity and dissipation of the mirrors. For this reason, we will mainly consider perfect reflectors in the next chapters. In the case of perfect reflectors, only two length scales are independent. We change over to dimensionless units, thereby simplify the equations and get rid of one length scale. The free energy is then determined by the temperature T and the ratio L/R : $\mathcal{F} = \mathcal{F}(T, L/R)$

We introduce the scaled quantities:

$$\tilde{\mathcal{F}} = \frac{\mathcal{L}}{\hbar c} \mathcal{F}, \quad \tilde{T} = \frac{2\pi k_B \mathcal{L}}{\hbar c} T, \quad \tilde{k} = \mathcal{L}k, \quad d\tilde{k} = \mathcal{L}dk, \quad \tilde{\kappa} = \mathcal{L}\kappa = \sqrt{n^2 \tilde{T}^2 + \tilde{k}^2} \quad (5.41)$$

We also define dimensionless quantities for ξ , ω_P and γ :

$$\tilde{\xi}_n = \frac{\xi_n \mathcal{L}}{c} = n\tilde{T}, \quad \tilde{\omega}_P = \frac{\omega_P \mathcal{L}}{c}, \quad \tilde{\gamma} = \frac{\gamma \mathcal{L}}{c} \quad (5.42)$$

The Mie coefficients are now evaluated at

$$\tilde{\chi} = \frac{nTR}{\mathcal{L}}. \quad (5.43)$$

Changing over to dimensionless quantities, the free energy becomes

$$\tilde{\mathcal{F}} = \frac{\tilde{T}}{\pi} \sum_{n=0}^{\infty} \sum_{m=0}^{\infty} \ln \det [\mathbb{1} - \mathcal{M}^{(m)}(n\tilde{T})] \quad (5.44)$$

with the integrals

$$A_{\ell_1 \ell_2, p}^{(m)}(n\tilde{T}) = m^2 n\tilde{T} \int_0^\infty d\tilde{k} \frac{1}{\tilde{k}\tilde{\kappa}} r_p(i\tilde{\xi}, \tilde{k}) e^{-2\tilde{\kappa}} P_{\ell_1}^m\left(\frac{\tilde{k}}{n\tilde{T}}\right) P_{\ell_2}^m\left(-\frac{\tilde{k}}{n\tilde{T}}\right), \quad (5.45)$$

$$B_{\ell_1 \ell_2, p}^{(m)}(n\tilde{T}) = \frac{1}{(n\tilde{T})^3} \int_0^\infty d\tilde{k} \frac{\tilde{k}^3}{\tilde{\kappa}} r_p(i\tilde{\xi}, \tilde{k}) e^{-2\tilde{\kappa}} P_{\ell_1}^{m'}\left(\frac{\tilde{k}}{n\tilde{T}}\right) P_{\ell_2}^{m'}\left(-\frac{\tilde{k}}{n\tilde{T}}\right), \quad (5.46)$$

$$C_{\ell_1 \ell_2, p}^{(m)}(n\tilde{T}) = -\frac{im}{n\tilde{T}} \int_0^\infty d\tilde{k} \frac{\tilde{k}}{\tilde{\kappa}} r_p(i\tilde{\xi}, \tilde{k}) e^{-2\tilde{\kappa}} P_{\ell_1}^m\left(\frac{\tilde{k}}{n\tilde{T}}\right) P_{\ell_2}^{m'}\left(-\frac{\tilde{k}}{n\tilde{T}}\right), \quad (5.47)$$

$$D_{\ell_1 \ell_2, p}^{(m)}(n\tilde{T}) = -\frac{im}{n\tilde{T}} \int_0^\infty d\tilde{k} \frac{\tilde{k}}{\tilde{\kappa}} r_p(i\tilde{\xi}, \tilde{k}) e^{-2\tilde{\kappa}} P_{\ell_1}^{m'}\left(\frac{\tilde{k}}{n\tilde{T}}\right) P_{\ell_2}^m\left(-\frac{\tilde{k}}{n\tilde{T}}\right). \quad (5.48)$$

We now drop the tildes and label quantities measured in SI units with a subscript “SI”.

5.7. Matsubara frequency $\xi = 0$

The argument of the associated Legendre polynomials in the integrals (5.45)–(5.48) diverge for the Matsubara frequency $n = 0$. However, the limit $nT \rightarrow 0$ exists and the contribution to the free energy is finite. In this section, we assume that the Fresnel coefficients r_p are independent of k for $nT \rightarrow 0$. We have seen in section 3.3 that this assumption is valid for perfect reflectors and Drude mirrors.

As the argument becomes large, we may approximate the associated Legendre polynomials by (A.15) and (A.16). We conclude that the integrals scale as

$$A_{\ell_1 \ell_2, p}^{(m)} \sim (nT)^{-\ell_1 - \ell_2 + 1}, \quad B_{\ell_1 \ell_2, p}^{(m)} \sim (nT)^{-\ell_1 - \ell_2 - 1}, \quad C_{\ell_1 \ell_2, p}^{(m)} \sim D_{\ell_1 \ell_2, p}^{(m)} \sim (nT)^{-\ell_1 - \ell_2}, \quad (5.49)$$

and the matrix elements of the round-trip operator scale as

$$\mathcal{M}^{(m)}(E, E)_{\ell_1 \ell_2} \sim \mathcal{M}^{(m)}(M, M)_{\ell_1 \ell_2} \sim (nT)^{\ell_1 - \ell_2}, \quad (5.50)$$

$$\mathcal{M}^{(m)}(E, M)_{\ell_1 \ell_2} \sim \mathcal{M}^{(m)}(M, E)_{\ell_1 \ell_2} \sim (nT)^{\ell_1 - \ell_2 + 1}. \quad (5.51)$$

The main contribution to the free energy comes from the integral $B_{\ell_1, \ell_2}^{(m)}$, all other integrals are at least one power of nT greater and therefore smaller than $B_{\ell_1, \ell_2}^{(m)}$. For this reason, we may neglect the integrals $A_{\ell_1 \ell_2, p}^{(m)}$, $C_{\ell_1 \ell_2, p}^{(m)}$ and $D_{\ell_1 \ell_2, p}^{(m)}$. Moreover, the scattering matrix becomes block diagonal, because the nondiagonal blocks $\mathcal{M}^{(m)}(E, M)$ and $\mathcal{M}^{(m)}(M, E)$ only depend on $C_{\ell_1 \ell_2, p}^{(m)}$ and $D_{\ell_1 \ell_2, p}^{(m)}$.

The integral $B_{\ell_1, \ell_2, p}^{(m)}$ can be evaluated analytically and we find for the matrix elements of the diagonal blocks

$$\mathcal{M}^{(m)}(E, E)_{\ell_1 \ell_2} \simeq \Lambda_{\ell_1 \ell_2}^{(m)} a_{\ell_1} B_{\ell_1 \ell_2, \text{TM}}^{(m)} = \Xi_{\ell_1 \ell_2}^{(m)} r_{\text{TM}}^{\xi \rightarrow 0} a_{\ell, 0}^{\text{perf}} \left(\frac{R}{\mathcal{L}}\right)^{\ell_1 + \ell_2 + 1} \left(\frac{nTR}{\mathcal{L}}\right)^{\ell_1 - \ell_2}, \quad (5.52)$$

$$\mathcal{M}^{(m)}(M, M)_{\ell_1 \ell_2} \simeq \Lambda_{\ell_1 \ell_2}^{(m)} b_{\ell_1} B_{\ell_1 \ell_2, \text{TE}}^{(m)} = \Xi_{\ell_1 \ell_2}^{(m)} r_{\text{TE}}^{\xi \rightarrow 0} b_{\ell, 0}^{\text{perf}} \left(\frac{R}{\mathcal{L}}\right)^{\ell_1 + \ell_2 + 1} \left(\frac{nTR}{\mathcal{L}}\right)^{\ell_1 - \ell_2}, \quad (5.53)$$

where we have defined

$$\Xi_{\ell_1 \ell_2}^{(m)} \equiv \Lambda_{\ell_1 \ell_2}^{(m)} \frac{(-1)^{\ell_2+1} (2\ell_1)! (2\ell_2)! (\ell_1 + \ell_2)!}{4^{2\ell_1+\ell_2+1} (\ell_1 - 1)! (\ell_2 - 1)! (\ell_1 - m)! (\ell_2 - m)!}. \quad (5.54)$$

The prefactors $a_{\ell,0}^{\text{perf}}$ and $b_{\ell,0}^{\text{perf}}$ have been defined in (3.35). The calculation of $B_{\ell_1, \ell_2, p}^{(m)}$ is carried out in appendix B.5. We see that the diagonal matrix elements are finite, while the matrix elements vanish beneath the diagonal and diverge above the diagonal. However, the determinant is finite in the limit $nT \rightarrow 0$. This is proven in appendix B.6.

For perfect reflectors the Fresnel coefficients are $r_{\text{TM}} = -r_{\text{TE}} = 1$ and we find for the logarithm of the determinant of the scattering matrix

$$\ln \det \mathcal{D}^{(m)} = \ln \det [\mathbb{1} - \mathcal{M}^{(m)}(E, E)] + \ln \det [\mathbb{1} - \mathcal{M}^{(m)}(M, M)] \quad (5.55)$$

with the matrix elements

$$\mathcal{M}^{(m)}(E, E)_{\ell_1 \ell_2}^{\xi \rightarrow 0} = +\Xi_{\ell_1 \ell_2}^{(m)} a_{\ell_1, 0}^{\text{perf}} \left(\frac{R}{\mathcal{L}} \right)^{\ell_1 + \ell_2 + 1}, \quad (5.56)$$

$$\mathcal{M}^{(m)}(M, M)_{\ell_1 \ell_2}^{\xi \rightarrow 0} = -\Xi_{\ell_1 \ell_2}^{(m)} b_{\ell_1, 0}^{\text{perf}} \left(\frac{R}{\mathcal{L}} \right)^{\ell_1 + \ell_2 + 1}. \quad (5.57)$$

In the Drude model the Fresnel coefficients are $r_{\text{TE}} = 0$ and $r_{\text{TM}} = 1$ for $\xi \rightarrow 0$ and we obtain

$$\ln \det \mathcal{D}^{(m)} = \ln \det [\mathbb{1} - \mathcal{M}^{(m)}(E, E)] \quad (5.58)$$

with matrix elements of $\mathcal{M}^{(m)}(E, E)$ identical to (5.56).

5.8. Conclusion

In this chapter, we have expressed the matrix elements of the scattering operator in the multipole basis and derived explicit expressions. We have both simplified the scattering formula and the matrix elements, changed over to scaled quantities, and investigated the symmetries of the matrix elements as well as their behaviour for $\xi \rightarrow 0$. For the sake of clearness and for reference, we want to collect the important results of this chapter.

The free energy is given as a sum

$$\mathcal{F} = \frac{T}{\pi} \sum_{n=0}^{\infty} \sum_{m=0}^{\infty} \ln \det [\mathbb{1} - \mathcal{M}^{(m)}(nT)], \quad (5.59)$$

where the round-trip matrix is organized as a block matrix

$$\mathcal{M}^{(m)}(nT) = \begin{pmatrix} \mathcal{M}^{(m)}(E, E) & -\text{Im} [\mathcal{M}^{(m)}(E, M)] \\ \text{Im} [\mathcal{M}^{(m)}(M, E)] & \mathcal{M}^{(m)}(M, M) \end{pmatrix}. \quad (5.60)$$

5. The scattering formula in the plane–sphere geometry

The matrix elements of the block matrices are given by

$$\mathcal{M}^{(m)}(E, E)_{\ell_1 \ell_2} = \Lambda_{\ell_1 \ell_2}^{(m)} a_{\ell_1}(i\xi) \left[A_{\ell_1 \ell_2, \text{TE}}^{(m)}(\xi) + B_{\ell_1 \ell_2, \text{TM}}^{(m)}(\xi) \right], \quad (5.61)$$

$$\mathcal{M}^{(m)}(M, M)_{\ell_1 \ell_2} = \Lambda_{\ell_1 \ell_2}^{(m)} b_{\ell_1}(i\xi) \left[A_{\ell_1 \ell_2, \text{TM}}^{(m)}(\xi) + B_{\ell_1 \ell_2, \text{TE}}^{(m)}(\xi) \right], \quad (5.62)$$

$$\mathcal{M}^{(m)}(E, M)_{\ell_1 \ell_2} = \Lambda_{\ell_1 \ell_2}^{(m)} a_{\ell_1}(i\xi) \left[C_{\ell_1 \ell_2, \text{TE}}^{(m)}(\xi) + D_{\ell_1 \ell_2, \text{TM}}^{(m)}(\xi) \right], \quad (5.63)$$

$$\mathcal{M}^{(m)}(M, E)_{\ell_1 \ell_2} = -\Lambda_{\ell_1 \ell_2}^{(m)} b_{\ell_1}(i\xi) \left[C_{\ell_1 \ell_2, \text{TM}}^{(m)}(\xi) + D_{\ell_1 \ell_2, \text{TE}}^{(m)}(\xi) \right], \quad (5.64)$$

with the integrals

$$A_{\ell_1 \ell_2, p}^{(m)}(nT) = m^2 nT \int_0^\infty dk \frac{1}{k\kappa} r_p(i\xi, k) e^{-2\kappa} P_{\ell_1}^m\left(\frac{\kappa}{nT}\right) P_{\ell_2}^m\left(-\frac{\kappa}{nT}\right), \quad (5.65)$$

$$B_{\ell_1 \ell_2, p}^{(m)}(nT) = \frac{1}{(nT)^3} \int_0^\infty dk \frac{k^3}{\kappa} r_p(i\xi, k) e^{-2\kappa} P_{\ell_1}^{m'}\left(\frac{\kappa}{nT}\right) P_{\ell_2}^{m'}\left(-\frac{\kappa}{nT}\right), \quad (5.66)$$

$$C_{\ell_1 \ell_2, p}^{(m)}(nT) = -\frac{im}{nT} \int_0^\infty dk \frac{k}{\kappa} r_p(i\xi, k) e^{-2\kappa} P_{\ell_1}^m\left(\frac{\kappa}{nT}\right) P_{\ell_2}^{m'}\left(-\frac{\kappa}{nT}\right), \quad (5.67)$$

$$D_{\ell_1 \ell_2, p}^{(m)}(nT) = -\frac{im}{nT} \int_0^\infty dk \frac{k}{\kappa} r_p(i\xi, k) e^{-2\kappa} P_{\ell_1}^{m'}\left(\frac{\kappa}{nT}\right) P_{\ell_2}^m\left(-\frac{\kappa}{nT}\right). \quad (5.68)$$

For $\xi = nT = 0$ the logarithm of the determinant of the scattering matrix is given by

$$\ln \det \mathcal{D}^{(m)} = \ln \det \left[\mathbb{1} - \mathcal{M}^{(m)}(E, E) \right] + \ln \det \left[\mathbb{1} - \mathcal{M}^{(m)}(M, M) \right] \quad (5.69)$$

with the matrix elements

$$\mathcal{M}^{(m)}(E, E)_{\ell_1 \ell_2}^{\xi \rightarrow 0} = r_{\text{TM}}^{\xi \rightarrow 0} \Xi_{\ell_1 \ell_2}^{(m)} a_{\ell_1, 0}^{\text{perf}} \left(\frac{R}{\mathcal{L}} \right)^{\ell_1 + \ell_2 + 1}, \quad (5.70)$$

$$\mathcal{M}^{(m)}(M, M)_{\ell_1 \ell_2}^{\xi \rightarrow 0} = r_{\text{TE}}^{\xi \rightarrow 0} \Xi_{\ell_1 \ell_2}^{(m)} b_{\ell_1, 0}^{\text{perf}} \left(\frac{R}{\mathcal{L}} \right)^{\ell_1 + \ell_2 + 1}. \quad (5.71)$$

In the limit $\xi \rightarrow 0$ the Fresnel coefficients become $r_{\text{TM}} = -r_{\text{TE}} = 1$ for perfect reflectors, and $r_{\text{TM}} = 1$, $r_{\text{TE}} = 0$ for Drude mirrors.

6. Numerical issues

The numerical implementation of the Casimir effect in the plane–sphere geometry is a challenging task. The main problem is the competing demands on the numerical implementation: stability and performance. On the one hand, the numerics is supposed to be stable over a wide range of parameters. On the other hand, the implementation is supposed to be fast in order to obtain results in tolerable time.

Luckily, we do not have to reinvent the wheel, but we may profit from the experience of CANAGUIER–DURAND [10]. In this chapter, we will focus on the problems that are either not covered by CANAGUIER–DURAND or that we have solved in a different way.

6.1. Truncation of the vector space

For the implementation one has to truncate the dimension of the scattering matrix \mathcal{D} to a finite value. This means that we only take multipole waves up to a moment ℓ_{\max} into account. As the scattering matrix consists of four block matrices, its dimension is thus $2\ell_{\max} \times 2\ell_{\max}$.

From a physical point of view it is reasonable that for values of ℓ_{\max} high enough the value of the free energy converges. This is argued qualitatively in Ref. [10]. It turns out that for smaller separations

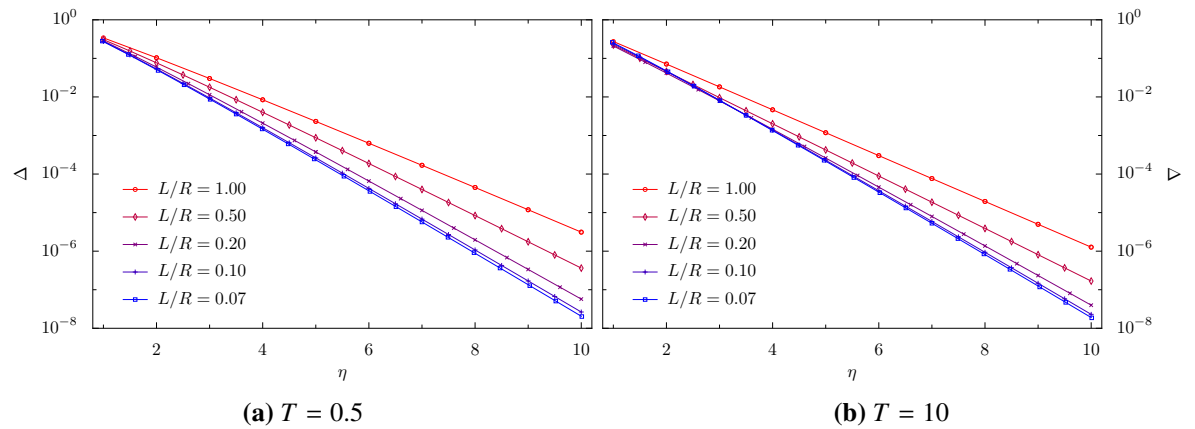


Figure 6.1.: Accuracy of the free energy as a function of the coefficient η . We show the achieved accuracy for several separations L/R for a) $T = 0.5$ and b) $T = 10$. ($\eta_c = 20$)

more multipole moments are needed in order to obtain the same accuracy. For this reason, we define a coefficient η and determine ℓ_{\max} by

$$\ell_{\max} = \eta \frac{R}{L}. \quad (6.1)$$

Fig. 6.1 shows the dependence of the accuracy on η . The accuracy is defined by

$$\Delta = \left| \frac{\mathcal{F}(\eta) - \mathcal{F}(\eta \rightarrow \infty)}{\mathcal{F}(\eta \rightarrow \infty)} \right| \approx \left| \frac{\mathcal{F}(\eta) - \mathcal{F}(\eta_c)}{\mathcal{F}(\eta_c)} \right| \quad \text{for } \eta_c \gg \eta, \quad (6.2)$$

and corresponds to the deviation from the exact result. Fig. 6.1 reveals that the accuracy Δ depends exponentially on η . Also, the accuracy depends only weakly on the temperature and for a chosen value of η the accuracy becomes better for smaller separations. To obtain an accuracy of 10^{-4} one has to choose $\eta = 6$ for separations $L/R \leq 0.2$.

6.2. Modified Bessel functions and Mie coefficients

The definition of the Mie coefficients a_ℓ , b_ℓ involves modified Bessel functions of the first $I_\nu(x)$ and of the second kind $K_\nu(x)$. We briefly outline the ideas of CANAGUIER–DURAND [10].

The modified Bessel functions for half-integer indices obey for $\ell > 2$ the recurrence relations (cf. (A.20))

$$I_{\ell+\frac{1}{2}}(x) = I_{\ell-\frac{3}{2}}(x) - \frac{(2\ell-1)I_{\ell-\frac{1}{2}}(x)}{x}, \quad K_{\ell+\frac{1}{2}}(x) = K_{\ell-\frac{3}{2}}(x) + \frac{(2\ell-1)K_{\ell-\frac{1}{2}}(x)}{x}. \quad (6.3)$$

With the initial functions

$$I_{\frac{1}{2}}(x) = \sqrt{\frac{2}{\pi x}} \sinh x, \quad I_{\frac{3}{2}} = \sqrt{\frac{2}{\pi x}} \left(\cosh x - \frac{\sinh x}{x} \right), \quad (6.4)$$

$$K_{\frac{1}{2}}(x) = \sqrt{\frac{\pi}{2x}} e^{-x}, \quad K_{\frac{3}{2}} = \sqrt{\frac{\pi}{2x}} \left(1 + \frac{1}{x} \right) e^{-x}, \quad (6.5)$$

the recurrence relations can be exploited to calculate the modified Bessel functions. This procedure works fine for $K_{\ell+\frac{1}{2}}(x)$, however, it is unstable for $I_{\ell+\frac{1}{2}}(x)$. The subtraction of two almost identical numbers is numerically ill-conditioned and causes a loss of significance. The recurrence formula for $I_{\ell+\frac{1}{2}}(x)$ contains such a subtraction which renders this method unusable for the calculation of $I_{\ell+\frac{1}{2}}(x)$.

The function $I_{\ell+\frac{1}{2}}(x)$ can be computed by a downward recurrence relation

$$I_{\ell+\frac{1}{2}}(x) = \frac{1}{x} \left(K_{\ell+\frac{3}{2}}(x) + f_{\ell+\frac{1}{2}}(x) K_{\ell+\frac{1}{2}}(x) \right)^{-1}, \quad (6.6)$$

where

$$f_{\ell+\frac{1}{2}}(x) = \frac{I_{\ell+\frac{3}{2}}(x)}{I_{\ell+\frac{1}{2}}(x)} = \frac{1}{\frac{2(\ell+1)+1}{x} + \frac{1}{\frac{2(\ell+2)+1}{x} + \dots}} = [a_1, a_2, a_3, \dots] \quad (6.7)$$

is a continued fraction with coefficients

$$a_n = \frac{2(\ell + n) + 1}{x}. \quad (6.8)$$

Eq. (6.6) has the disadvantage that the accuracy of $f_{\ell+\frac{1}{2}}$ cannot be improved in an iterative way: if the accuracy is unsatisfactory the calculation has to be repeated from the beginning. However, $f_{\ell+\frac{1}{2}}$ can be transferred to

$$f_{\ell+\frac{1}{2}}^N(x) = [a_1, a_2, \dots, a_N] = \frac{[a_1] \cdot [a_2, a_1] \cdot \dots \cdot [a_N, \dots, a_2, a_1]}{[a_2] \cdot [a_3, a_2] \cdot \dots \cdot [a_N, \dots, a_3, a_2]} \quad (6.9)$$

and the continued fraction can be computed up to the desired accuracy.

Given the modified Bessel functions, it is easy to compute the Mie coefficients. The Mie coefficients are evaluated at the argument $\chi = nTR/\mathcal{L}$ which only depends on n . For a given value of $n > 0$ it is thus sufficient to compute the Mie coefficients $a_1, \dots, a_{\ell_{\max}}$ and $b_1, \dots, b_{\ell_{\max}}$ once and store the results. For this reason, the time needed to calculate the Mie coefficients is negligible compared to the total computational time.

6.3. Integration

For the numerical evaluation of the integrals we first perform a change of variable. We substitute

$$x = 2\kappa - 2nT, \quad k = \sqrt{\frac{x^2}{4} + nTx}, \quad \kappa = \frac{x}{2} + nT, \quad dx = \frac{2k}{\kappa} dk, \quad (6.10)$$

and obtain

$$A_{\ell_1 \ell_2, p}^{(m)} = (-1)^{\ell_2+m} m^2 \tau e^{-\tau} \int_0^\infty dx \frac{r_p e^{-x}}{x^2 + 2\tau x} P_{\ell_1}^m \left(1 + \frac{x}{\tau}\right) P_{\ell_1}^m \left(1 + \frac{x}{\tau}\right), \quad (6.11)$$

$$B_{\ell_1 \ell_2, p}^{(m)} = \frac{(-1)^{\ell_2+m+1} e^{-\tau}}{\tau^3} \int_0^\infty dx r_p e^{-x} (x^2 + 2\tau x) P_{\ell_1}^{m'} \left(1 + \frac{x}{\tau}\right) P_{\ell_1}^{m'} \left(1 + \frac{x}{\tau}\right), \quad (6.12)$$

$$C_{\ell_1 \ell_2, p}^{(m)} = im \frac{(-1)^{\ell_2+m} e^{-\tau}}{\tau} \int_0^\infty dx r_p e^{-x} P_{\ell_1}^m \left(1 + \frac{x}{\tau}\right) P_{\ell_2}^{m'} \left(1 + \frac{x}{\tau}\right), \quad (6.13)$$

$$D_{\ell_1 \ell_2, p}^{(m)} = (-1)^{\ell_1+\ell_2+1} C_{\ell_1 \ell_2, p}^{(m)}, \quad (6.14)$$

where we have introduced the abbreviation $\tau \equiv 2nT$ and used the parity of the associated Legendre polynomials (cf. (A.10)). The integrals have now the form $\int_0^\infty dx f(x) e^{-x}$ and we can use Gauss-Laguerre quadrature. Gauss-Laguerre quadrature is a Gaussian quadrature with weighting function

$W(x) = e^{-x}$. The integral can be evaluated by

$$\int_0^\infty dx f(x) e^{-x} = \sum_{k=1}^N w_k f(x_k) + R_N, \quad (6.15)$$

where w_k are Christoffel coefficients

$$w_k = \frac{1}{(N+1)L'_N(x_k)L_{N+1}(x_k)}, \quad (6.16)$$

and $L_N(x)$ are Laguerre polynomials [1]. The remainder is given by

$$R_N = \frac{2N!}{(2N)!} f^{(2N)}(c), \quad c \in [0, \infty). \quad (6.17)$$

In particular, if $f(x)$ is a polynomial of degree p , Gauss-Laguerre quadrature becomes exact for $p \leq 2N - 1$. The Christoffel coefficients can be precomputed or copied from tables like [1, 43].

We now show that for perfect reflectors $f(x)$ is a polynomial. The reflection coefficients of perfect reflectors are mere numbers $r_{\text{TM}} = -r_{\text{TE}} = 1$. For $m = 0$ only the integral $B_{\ell_1 \ell_2, p}^{(0)}$ is nonzero. In this case the associated Legendre polynomials become ordinary Legendre polynomials which are polynomials. As derivatives of polynomials are also polynomials, the integrand consists of polynomials and the exponential function and thus $f(x)$ is a polynomial. For $m \neq 0$ we can transform the integrals (6.11)–(6.14) to

$$A_{\ell_1 \ell_2, p}^{(m)} = (-1)^{\ell_2} m^2 \frac{e^{-\tau}}{\tau^{2m-1}} \int_0^\infty dx r_p e^{-x} (x^2 + 2\tau x)^{m-1} P_{\ell_1}^{(m)}\left(1 + \frac{x}{\tau}\right) P_{\ell_2}^{(m)}\left(1 + \frac{x}{\tau}\right), \quad (6.18)$$

$$\begin{aligned} B_{\ell_1 \ell_2, p}^{(m)} &= \frac{(-1)^{\ell_2+1} e^{-\tau}}{\tau^{2m-1}} \int_0^\infty dx e^{-x} r_p (x^2 + 2\tau x)^{m-1} \\ &\quad \times \left[(\ell_1 - m + 1) P_{\ell_1+1}^{(m)}\left(1 + \frac{x}{\tau}\right) - (\ell_1 + 1) \left(1 + \frac{x}{\tau}\right) P_{\ell_1}^{(m)}\left(1 + \frac{x}{\tau}\right) \right] \\ &\quad \times \left[(\ell_2 - m + 1) P_{\ell_2+1}^{(m)}\left(1 + \frac{x}{\tau}\right) - (\ell_2 + 1) \left(1 + \frac{x}{\tau}\right) P_{\ell_2}^{(m)}\left(1 + \frac{x}{\tau}\right) \right], \end{aligned} \quad (6.19)$$

$$\begin{aligned} C_{\ell_1 \ell_2, p}^{(m)} &= im \frac{(-1)^{\ell_2} e^{-\tau}}{\tau^{2m-1}} \int_0^\infty dx e^{-x} r_p (x^2 + 2\tau x)^{m-1} P_{\ell_1}^{(m)}\left(1 + \frac{x}{\tau}\right) \\ &\quad \times \left[(\ell_2 - m + 1) P_{\ell_2+1}^{(m)}\left(1 + \frac{x}{\tau}\right) - (\ell_2 + 1) \left(1 + \frac{x}{\tau}\right) P_{\ell_2}^{(m)}\left(1 + \frac{x}{\tau}\right) \right], \end{aligned} \quad (6.20)$$

where we have used (A.6) and (A.8). By $P_\ell^m(x)$ we denote the associated Legendre polynomial of degree ℓ and order m , whereas by

$$P_\ell^{(m)}(x) = \frac{d^m}{dy^m} P_\ell(y) \Big|_{y=x} \quad (6.21)$$

we denote the m -th derivative of the ordinary Legendre polynomial of degree ℓ . We thus see that $f(x)$ is also a polynomial for $m > 0$. For this reason, Gauss-Laguerre quadrature can be used to compute the integrals exactly.

However, in the numerical implementation we use a different approach. The integral

$$\int_0^\infty dx x^n e^{-x} = n! \quad (6.22)$$

can be calculated analytically. If the coefficients of the polynomial $f(x)$ are known, the integrals (6.18)–(6.20) can be calculated by

$$\int_0^\infty dx f(x) e^{-x} = \int_0^\infty dx e^{-x} \sum_{k=0}^N c_k x^k = \sum_{k=0}^N c_k k!. \quad (6.23)$$

A look at (6.18)–(6.20) reveals that $f(x)$ consists of three polynomials $f(x) = f_1(x)f_2(x)f_3(x)$. First, the coefficients of the polynomials f_1 , f_2 and f_3 must be determined and afterwards the three polynomials must be multiplied. On the one hand, the coefficients can be determined using (A.13) and (A.14), however, this is not very efficient. On the other hand, the polynomial multiplications are done by a naive algorithm instead of the faster Karatsuba or Schönhage–Strassen algorithm. For this reason, the integration takes up a considerable part of the total computational time and is thus a good candidate for further optimizations.

6.4. Matrix elements

Due to the Mie coefficients and the integrals, the matrix elements may become very small or very large. This is a very challenging numerical problem for two reasons: The matrix elements must be computed and stored, and the algorithm that calculates the determinant must handle an ill-conditioned matrix whose entries differ by hundreds of orders of magnitude. Fig. 6.2 shows two examples of ill-conditioned matrices.

Modern computers use the IEEE 754 standard [24] for floating point computations. The standard defines arithmetic formats with single (32 bits) and double precision (64 bits). A double can represent numbers in the range from $4.94 \cdot 10^{-324}$ to $1.80 \cdot 10^{308}$. However, this is not sufficient for small separations. We present here three different solutions that all have been implemented in the numerical program.

6.4.1. Using logarithms

The idea of this solution is to represent matrix elements by its logarithms. This way we drastically expand the range of representable numbers. In doing so, we also increase the holes between representable numbers. However, numerical tests show that this raises no computational problems.

The logarithm of a negative number is complex. As we want to use real numbers, we have to store the sign separately. So, we represent a number a by

$$\tilde{a} = (-1)^{s_a} \ln|a|, \quad (6.24)$$

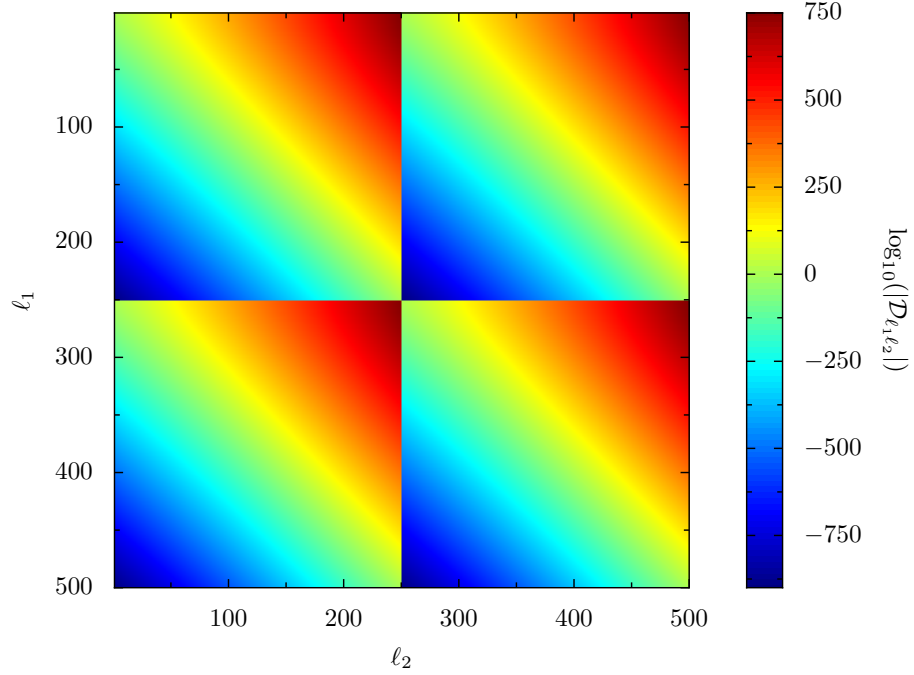
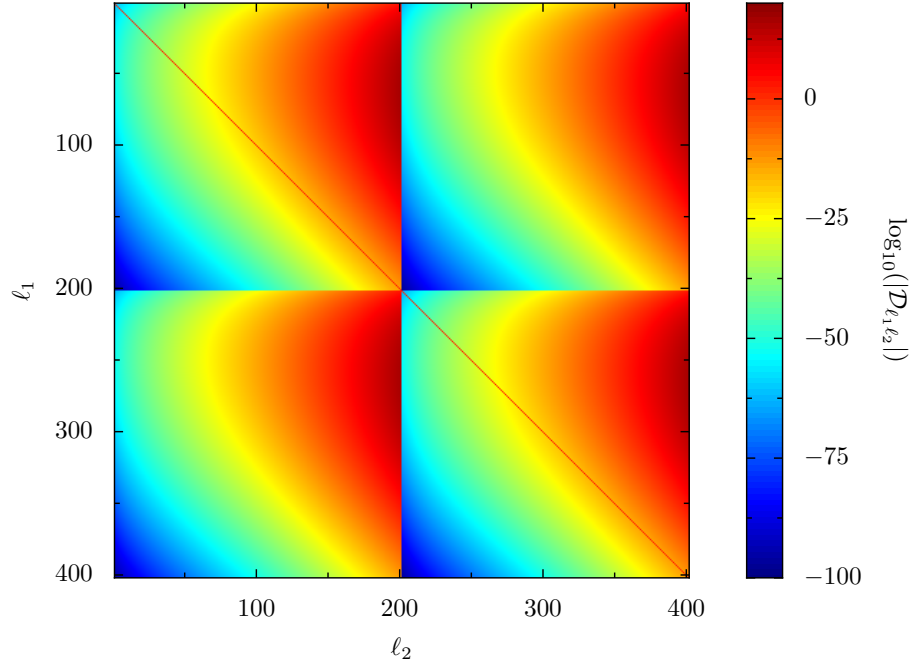
(a) $T = 0.1, n = 1, m = 1$ (b) $T = 5, n = 50, m = 50$

Figure 6.2.: Two scattering matrices for $L/R = 0.02$ and different values of T, n and m . The matrix elements in a) differ by more than thousand orders of magnitude, in b) by more than hundred orders of magnitude. In a) the Matsubara frequency is $\xi_1 = 0.1$ and the matrix elements scale similar to the $\xi \rightarrow 0$ case. For this reason, the condition of the matrix can be improved by multiplying each matrix element with a factor $(nTR/\mathcal{L})^{\ell_2 - \ell_1}$ (cf. section 5.7, in particular eqs. (5.52) and (5.53)). The structure of matrix b) is more complicated and no simple transformation that improves the condition is known. The red line on the diagonal in b) corresponds to the identity matrix, $\mathcal{D} = \mathbb{1} - \mathcal{M}$.

where $s_a = \text{sgn}(a)$. A major drawback of this method is that we cannot use basic arithmetic operations like addition or multiplication anymore. Multiplication of two numbers a and b becomes trivial, as it becomes an addition

$$\widetilde{ab} = (-1)^{s_a+s_b} (\ln|a| + \ln|b|). \quad (6.25)$$

The addition of two numbers is more complicated. We must take care of the signs of both numbers and avoid over- and underflows:

$$(\widetilde{a+b}) = \begin{cases} (-1)^{s_b} \ln|b|, & \text{if } \ln|a| = -\infty \\ (-1)^{s_a} \ln|a|, & \text{if } \ln|b| = -\infty \\ (-1)^{s_a} \left[\ln|a| + \ln\left(1 + (-1)^{s_a+s_b} e^{\ln|b| - \ln|a|}\right) \right], & \text{if } \ln|a| > \ln|b| \\ (-1)^{s_b} \left[\ln|b| + \ln\left(1 + (-1)^{s_a+s_b} e^{\ln|a| - \ln|b|}\right) \right], & \text{otherwise} \end{cases} \quad (6.26)$$

Many programming languages provide a function $\log1p(x)$ that returns the natural logarithm of $1+x$ in a way which is accurate for small values of x .

This method only depends on double arithmetics. Double arithmetics is fast and supported on almost every platform. But additions become costly, as they usually involve the computation of the exponential and the logarithm function. Besides, the code becomes obfuscated.

6.4.2. Quadruple precision

Another way to solve the problem is the use of 128 bits quadruple precision. Quadruple precision is supported by the GNU C Compiler (gcc) and the Intel C Compiler (icc). Quads have an exponent of 15 bits and cover almost 9900 orders of magnitude. However, usually processors do not support quads and the operations have to be carried out in software which makes quad arithmetics very slow. The increase of computational time renders this method impractical for actual calculations, yet it is a good way to estimate the numerical stability of the two faster methods.

6.4.3. Extended double precision

On x86 and x86-64 processors the floating point unit (FPU) supports the extended precision format with 80 bits and 15 bits exponent. The extended double format covers the same range of numbers like quadruple precision, is more precise than the double format, but less precise than the quadruple format. Gcc and icc support the extended double format and also provide a library with basic mathematical functions. The actual calculations are performed in the floating point unit. Extensions to the x86 instruction set like SSE only support the double format and thus the compiler cannot use these extensions for optimizations and parallelizations. However, this is still the fastest solution. It is about a factor of 10 faster than quads and a factor of 2 faster than the logarithm approach.

	logarithm approach	extended double precision	quadruple precision
runtime	$\approx 2x$	1x	$\approx 10x$
accuracy	ok	good	excellent
portability	almost all platforms	most compilers on x86, x86-64	few compilers
readability	poor	good	good

Table 6.1.: Comparison of the three different solutions. The runtime is given compared to the runtime using the extended double format.

6.4.4. Conclusion

All calculations in this master thesis are carried out using extended double precision unless otherwise stated. This is the fastest method with a good accuracy and in most cases the best choice. On non x86 or x86-64 platforms the logarithm approach still gives good results, but it is about a factor of 2 slower. The quadruple precision is only useful when comparing results with one of the other methods, in all other cases quadruple precision is too slow for actual computations. The three approaches are compared in table 6.1.

6.5. Determinant

The scattering matrix \mathcal{D} is ill-conditioned and the calculation of its determinant is sensitive to round-
ing errors. In order to improve the accuracy, the matrix must be balanced before computing the determinant. The balancing procedure uses similarity transformations to make corresponding rows and columns have comparable norms, while leaving the determinant of the matrix unchanged [42, 51]. This is the key point of the calculation of the determinant: Without balancing, the calculation of the determinant is numerically unstable.

After balancing, the determinant is calculated using a QR decomposition of the scattering matrix into a product of an orthogonal matrix Q and an upper triangle matrix R :

$$\mathcal{D} = QR \tag{6.27}$$

The QR decomposition is computed with a series of Givens rotations [21]. After the QR decomposition, the logarithm of the determinant of the scattering matrix can be computed easily:

$$\ln \det \mathcal{D} = \ln \det R = \ln \det \begin{pmatrix} a_{11} & a_{12} & a_{13} & \dots \\ & a_{22} & a_{23} & \dots \\ & & a_{33} & \dots \\ 0 & & & \ddots \end{pmatrix} = \ln \prod_{k=1}^N a_{kk} = \sum_{k=1}^N \ln a_{kk} \tag{6.28}$$

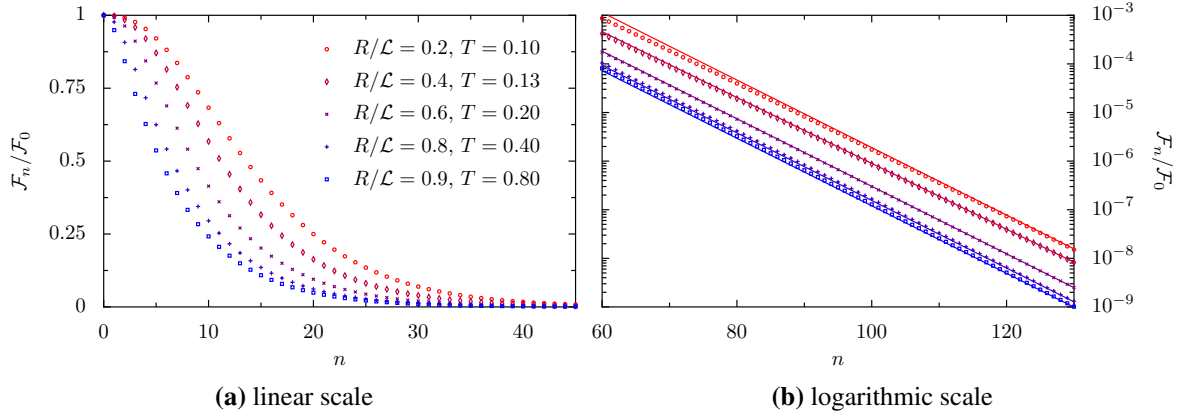


Figure 6.3.: Contributions of the n -th Matsubara frequency to the free energy: In a) we plot $\mathcal{F}_n/\mathcal{F}_0$ for different temperatures T and aspect ratios R/\mathcal{L} . For $nT \gg 1$ the contributions fall off exponentially. In b) we use a logarithmic scale for $\mathcal{F}_n/\mathcal{F}_0$. The symbols correspond to the same parameters as in plot a). The solid lines correspond to $\mathcal{F}_n/\mathcal{F}_0 = \mathcal{F}_{130} e^{-2nT(1-R/\mathcal{L})}/\mathcal{F}_0$.

6.6. Truncation of the infinite sum over n

The free energy is given as an infinite sum over the Matsubara frequencies $\xi_n = nT$ and every frequency ξ_n yields an independent contribution \mathcal{F}_n to the free energy

$$\mathcal{F} = \sum_{n=0}^{\infty} \mathcal{F}_n. \quad (6.29)$$

From a physical point of view it is obvious that this sum converges. While the Mie coefficients grow exponentially for large Matsubara frequencies $nT \gg 1$ (cf. (3.36))

$$a_\ell \sim b_\ell \sim e^{2nT \frac{R}{\mathcal{L}}}, \quad (6.30)$$

the integrals (5.45)–(5.48) decrease exponentially

$$A_{\ell_1, \ell_2, p}^{(m)} \sim B_{\ell_1, \ell_2, p}^{(m)} \sim C_{\ell_1, \ell_2, p}^{(m)} \sim D_{\ell_1, \ell_2, p}^{(m)} \sim e^{-2nT}. \quad (6.31)$$

In fact, the behaviour of the integrals is more complicated, however, for our argumentation it is sufficient that they decrease somehow exponentially. If we also assume that for $nT \gg 1$ the matrix elements become small, we can approximate the logarithm of the determinant of the scattering matrix by a trace

$$\ln \det(\mathbb{1} - \mathcal{M}) \approx -\text{Tr } \mathcal{M}. \quad (6.32)$$

So we expect that the contributions to the free energy \mathcal{F}_n decrease like

$$\mathcal{F}_n \sim \exp \left[-2nT \left(1 - \frac{R}{\mathcal{L}} \right) \right] \quad \text{for } nT \gg 1. \quad (6.33)$$

Although our argumentation is oversimplifying, it is surprising that the result is not too bad: Fig. 6.3 shows that the contributions to the free energy decrease vaguely as predicted by (6.33).

The numerical implementation cannot sum up infinite elements, but we have to crop the sum at some point. Therefore, we split the series in a finite sum that we compute and a remainder that we neglect:

$$\sum_{n=0}^{\infty} \mathcal{F}_n = \sum_{n=0}^k \mathcal{F}_n + R_k. \quad (6.34)$$

We determine the value of k using the inequality

$$\frac{\mathcal{F}_k}{\mathcal{F}_0} \leq \epsilon_p, \quad \text{where } \epsilon_p \in (0, 1). \quad (6.35)$$

Smaller values of ϵ_p yield better accuracies. The remainder may be estimated using (6.33):

$$R_k = \sum_{n=k+1}^{\infty} \mathcal{F}_n \simeq \mathcal{F}_k \sum_{n=1}^{\infty} q^n = \mathcal{F}_k \frac{q}{1-q}, \quad q = e^{-2T(1-\frac{R}{L})} \quad (6.36)$$

Eq. (6.36) can be used to increase the accuracy for a given value of ϵ_p . However, the implementation does not use this estimation yet.

6.7. Truncation of the sum over m

After the truncation of the vector space, the sum over m is finite

$$\mathcal{F}_n = \sum_{m=0}^{\ell_{\max}} \mathcal{F}_n^m \quad (6.37)$$

and all terms can be computed. Fig. 6.4 shows the contributions to \mathcal{F}_n dependent on m for different temperatures and separations. The contributions to the free energy fall off exponentially. This means that terms for high values of m are extremely slight and can be neglected. This improves the run-time of the numerics as less terms have to be computed. The summation is aborted when

$$\frac{\mathcal{F}_n^k}{\sum_{m=0}^k \mathcal{F}_n^m} \leq \epsilon_p, \quad (6.38)$$

where ϵ_p is as in section 6.6. As the contributions decrease exponentially, the remainder R_k may be estimated by

$$R_k = \sum_{m=k+1}^{\ell_{\max}} \mathcal{F}_n^m \approx \mathcal{F}_n^k \sum_{m=1}^{\ell_{\max}-k} q^k, \quad (6.39)$$

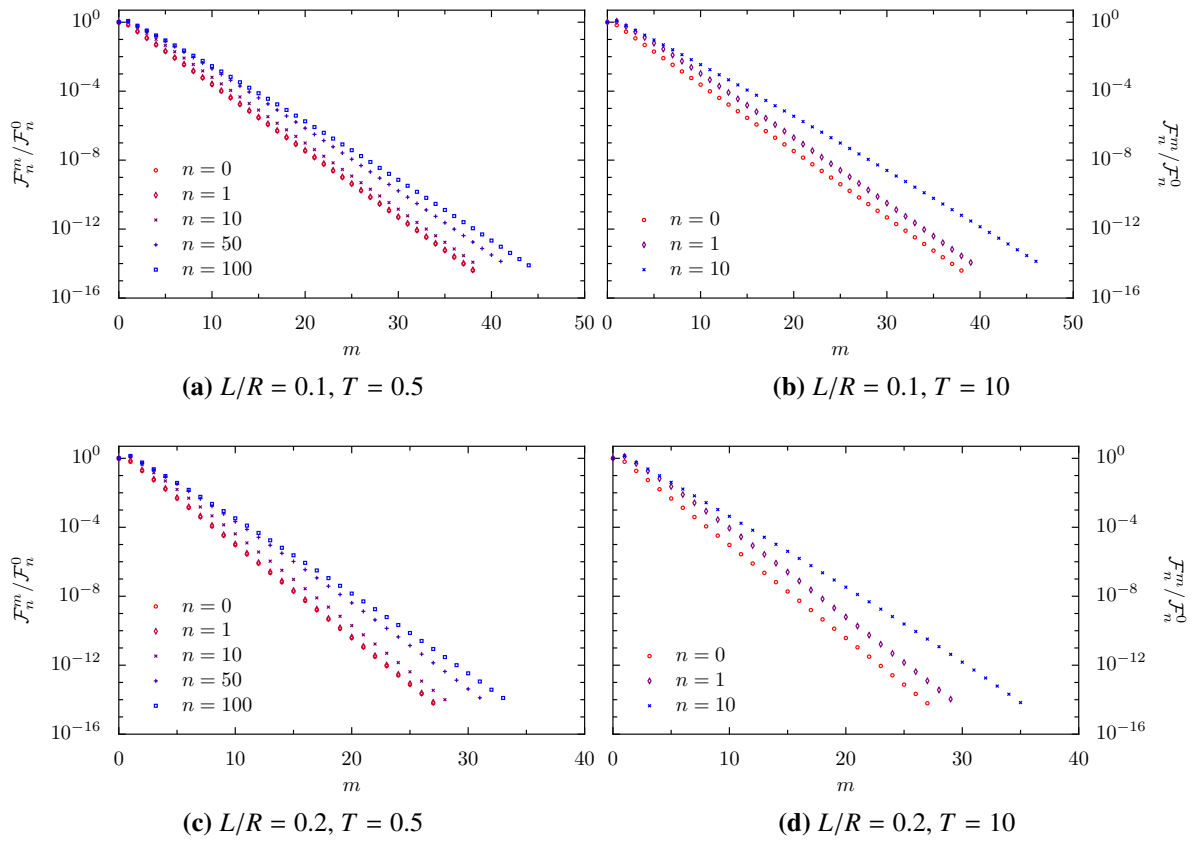


Figure 6.4.: Decrease of the contributions to the free energy dependent on m for fixed values of n .

where q can be obtained by linear regression. Although this would increase the accuracy of the result, the implementation does not support this feature yet.

6.8. Numerical differentiation

The force and the entropy are given as derivatives of the Casimir free energy

$$F = -\frac{\partial \mathcal{F}}{\partial L}, \quad S = -\frac{\partial \mathcal{F}}{\partial T}. \quad (6.40)$$

In order to calculate the derivative of a function $f(x)$ we use the finite difference formula of order 4 [17]

$$f'(x) = \frac{-f(x+2h) + 8f(x+h) - 8f(x-h) + f(x-2h)}{12h} + \frac{h^4}{30}f^{(5)}(c), \quad (6.41)$$

where $c \in [x-2h, x+2h]$. A detailed discussion about problems and errors of numerical differentiation can be found in [42].

6.9. Numerical stability

The accuracy of the result depends on the choices of ℓ_{\max} and ϵ_p as well as on round-off and other numerical errors. The first kind of errors, i.e. the dependence of the accuracy on ℓ_{\max} and ϵ_p , was investigated in previous sections. In this section, we want to investigate the numerical stability of the program. Under stability we understand the stability of the program for fixed parameters. In simple words, we ask: “Does the result change if we calculate with higher precision while keeping the values of ℓ_{\max} and ϵ_p fixed?”

Most numerical results of this master thesis have been computed using extended double format. However, the numerical program also supports the more accurate quad format. The extended double format gives about 18 significant decimal digits while the quad format gives about 33. This way we can compare the results of both implementations. The program is believed to be reliable if both implementations yield (almost) same results. “Almost same results” means that the deviation of both implementations

$$\Delta = \left| \frac{\mathcal{F}^{\text{extended double}}\left(T, \frac{L}{R}\right) - \mathcal{F}^{\text{quad}}\left(T, \frac{L}{R}\right)}{\mathcal{F}^{\text{quad}}\left(T, \frac{L}{R}\right)} \right| \quad (6.42)$$

is not larger than the estimated numerical error due to the truncation of the scattering matrix, and the truncations of the sums over n and m .

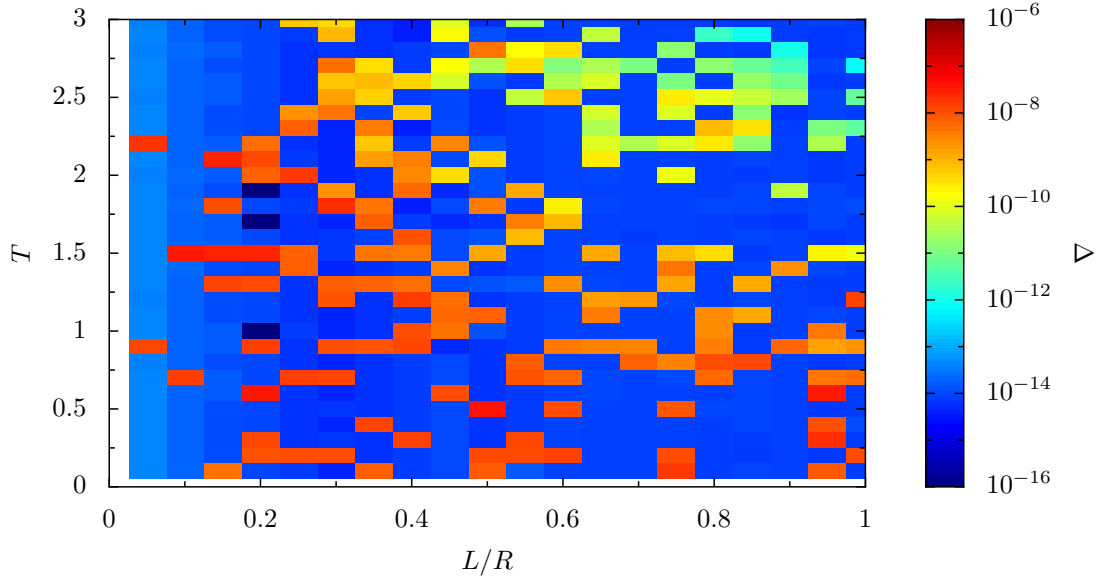


Figure 6.5.: Deviations of the free energy calculated using extended double and quad format. Both computations yield almost same results.

In Fig. 6.5 we plot the deviations of the results obtained using extended double and quad format. We have used $\ell_{\max} = \max(20, \lceil \eta R/L \rceil)$ with $\eta = 6$ and $\epsilon_p = 10^{-7}$. The error due to ℓ_{\max} and ϵ_p is believed to be about 10^{-4} to 10^{-5} . We see that the deviations are smaller than the accuracy.

The resolution of Fig. 6.5 is 30 points for T and 20 points for L/R . This is the reason why the points look like bricks. The numerical results were obtained using parallelization. The parallelized algorithm is non-deterministic, because the conditions for the truncation of the sums over m and n may be checked too late and more terms than necessary have been computed. So, the non-deterministic algorithm is the main reason for the “noise” in Fig. 6.5.

7. The proximity force approximation

Another method to calculate the free Casimir energy between arbitrary shaped smooth objects is the proximity force approximation (PFA). The PFA links arbitrary geometries to the much simpler plane–plane geometry and also accounts for thermal effects and finite conductivity of the mirrors. For this reason, the PFA is commonly used for comparisons with experiments. Although the approximation is believed to become accurate for small separations, no error estimates exist [18].

In this chapter, we want to compare numerical results obtained using the scattering approach with predictions of the PFA. We will only consider perfect reflectors here. We will see that for small separations the PFA becomes a good approximation. However, even for separations $L/R \sim 0.02$ the error of the approximation is still in the percent range.

7.1. The PFA for the plane–sphere geometry

We will follow the derivation from Ref. [7]. Let us consider two bodies: the surface of the upper body may be described by $z_1 = z_1(x, y)$ and the surface of the lower by $z_2 = z_2(x, y)$. Then the separation between both bodies is given by

$$d(x, y) \equiv z_1(x, y) - z_2(x, y). \quad (7.1)$$

For a given point (x, y) we now replace the infinitesimal surface elements dS_1 of the upper and dS_2 of the lower body by parallel surface elements $dxdy$ around the points $z_1(x, y)$ and $z_2(x, y)$. Thereby we link the unknown interaction energy to the well-known energy of the plane–plane geometry. In this way we can calculate the free energy of this geometry by integration

$$\mathcal{F}_{\text{PFA}} = \int_{\Sigma} \frac{\mathcal{F}_{\text{PP}}(d(x, y))}{A} dxdy, \quad (7.2)$$

where Σ is the area of the xy -plane where the function $d(x, y)$ is defined. For the plane–sphere geometry the idea of the PFA is sketched in Fig. 7.1.

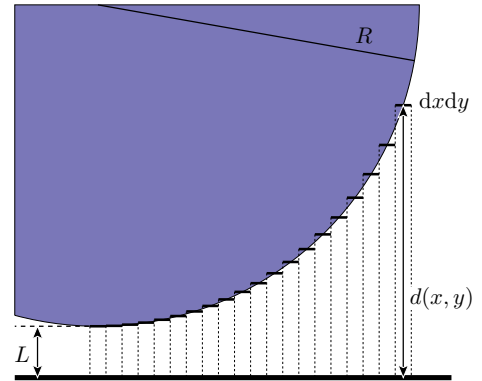


Figure 7.1.: PFA for the plane–sphere geometry. The sphere is approximated by infinitesimal plates that are parallel to the plane.

Let us now apply the PFA to the plane–sphere geometry. The separation between plane and sphere is given by

$$d(x, y) = L + R - \sqrt{R^2 - x^2 - y^2} = L + R(1 - \cos \theta) \quad (7.3)$$

and the integration can be carried out in spherical coordinates

$$\mathcal{F}_{\text{PFA}} = \int_0^{2\pi} d\varphi \int_0^{\pi/2} d\theta \frac{\mathcal{F}_{\text{PP}}(L + R(1 - \cos \theta))}{A} R^2 \sin \theta, \quad (7.4)$$

where $R^2 \sin \theta d\theta d\varphi$ is the surface element in spherical coordinates. The integrand is independent of φ and the integration over θ can be simplified by substituting $t = 1 + (1 - \cos \theta)R/L$. Doing so, we obtain for the free energy in the plane–sphere geometry

$$\mathcal{F}_{\text{PFA}} = 2\pi RL \int_1^{1+R/L} dt \frac{\mathcal{F}_{\text{PP}}(Lt)}{A}. \quad (7.5)$$

The evaluation of (7.5) is notably simpler than the formulas we obtained in the scattering formalism. However, the PFA neglects some intrinsic properties of the plane–sphere geometry:

- The PFA ignores the finite curvature of the sphere. In particular, the curvature alters the way waves are scattered. While the curvature causes waves to be scattered in different directions, wave scattering is resonant in the PFA. This is the reason why the PFA usually overestimates the value of the free energy.
- The PFA uses the free energy of the plane–plane geometry. In this geometry the polarizations $p = \text{TE}, \text{TM}$ are uncoupled and yield independent contributions to the free energy. However, in the plane–sphere geometry the polarizations are coupled. This will become important in the study of the large–distance limit in chapter 8.
- The Casimir free energy is non-additive. However, the PFA assumes that the sphere can be divided into small parallel area elements and the contributions of these area elements with the plane are additive.
- For perfect reflectors the entropy is always positive in the plane–plane geometry. In the PFA approximation the free energy is given as an integral over the free energy in the plane–plane geometry and the entropy obtained is always positive. However, in the plane–sphere geometry the entropy becomes negative for a wide range of parameters.

In the next section we will compare our numerical results obtained using the scattering approach with the PFA approximation.

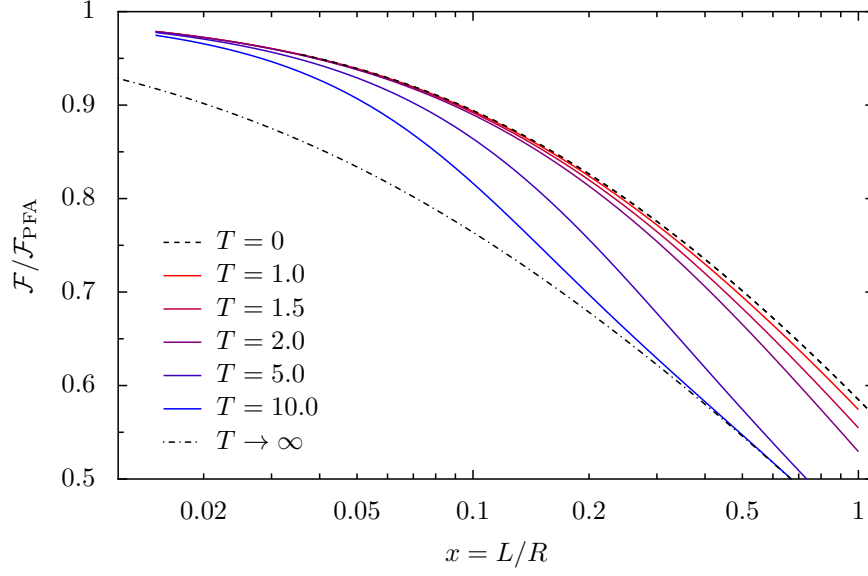


Figure 7.2.: Comparison of the PFA approximation with numerical results obtained using the scattering formalism versus the aspect ratio $x = L/R$. We plot the ratio $\mathcal{F}/\mathcal{F}_{\text{PFA}}$ for different temperatures, including the zero temperature and the high temperature limit. The numerical data for the zero temperature limit (for $x > 0.035$) are obtained by interpolation (cf. section 9.1), the data for the high temperature limit are obtained by calculating the $n = 0$ Matsubara term (cf. section 9.2).

7.2. Comparison with scattering approach

The aspect ratio L/R will play a crucial role in our considerations and for this reason we define $x \equiv L/R$. For perfect reflectors we can insert (4.16) into (7.5) and obtain

$$\mathcal{F}_{\text{PFA}} = \frac{T}{4\pi x} \int_1^{1+x^{-1}} dt \frac{1}{t^2} \sum_n \left[\text{Li}_3 \left(e^{-2nTtx/(x+1)} \right) + \frac{2nTtx}{1+x} \text{Li}_2 \left(e^{-2nTtx/(x+1)} \right) \right], \quad (7.6)$$

where we use the dimensionless quantities defined in section 5.6. From (4.17) and (4.19) we find the behaviour for $T = 0$ and high temperatures:

$$\mathcal{F}_{\text{PFA}}^{T=0} = -\frac{\pi^3}{720} \frac{1+2x}{x^3+x^2} \approx -\frac{\pi^3}{720 x^2} \quad (7.7)$$

$$\mathcal{F}_{\text{PFA}}^{\text{HT}} = -\frac{T\xi(3)}{8\pi} \frac{1}{x^2+x} \approx -\frac{T\xi(3)}{8\pi x} \quad (7.8)$$

The free energy in the Drude model becomes independent of the particular properties of the metal for high temperatures and we find

$$\mathcal{F}_{\text{PFA}}^{\text{HT,D}} = -\frac{T\xi(3)}{16\pi} \frac{1}{x^2+x} \approx -\frac{T\xi(3)}{16\pi x}. \quad (7.9)$$

The expressions obtained for the high temperature limit for perfect reflectors and Drude mirrors differ by a factor of 2. The reason is the same as in section 4.4: The Fresnel coefficient for TE polarization for $\xi \rightarrow 0$ becomes $r_{\text{TE}} = 0$ in the Drude model, but $r_{\text{TE}} = -1$ for perfect reflectors.

In Fig. 7.2 we plot the ratio $\mathcal{F}/\mathcal{F}_{\text{PFA}}$ in the range $0.015 \leq L/R \leq 1$ for different temperatures including $T = 0$ and the high temperature limit. The numerical results were obtained using $\ell_{\text{max}} = \max(25, \lceil \eta R/L \rceil)$ with $\eta = 5.8$ and $\epsilon_p = 2 \cdot 10^{-7}$. For small separations the ratio $\mathcal{F}/\mathcal{F}_{\text{PFA}}$ tends to unity. The accuracy of the PFA becomes better for small separations and for low temperatures. For $L/R = 0.015$ the ratio is 0.9788 for $T = 1$, and 0.9747 for $T = 10$. However, the PFA approximation is a good approximation for small separations and only for small separations. For separations $L/R \approx 0.1$ the ratio $\mathcal{F}/\mathcal{F}_{\text{PFA}}$ is only about 0.9 even for very small temperatures. We also want to remind the reader that the PFA does not cover effects like negative entropies in the plane–sphere geometry. Moreover, the PFA is in a sense an uncontrolled approximation as no error estimates exist.

We want to stress one more point: The PFA becomes a good approximation for small separations. This means that it captures the main physical effects in its limits of validity. However, entropies obtained using the PFA are always positive. From that we may conclude that the effect of negative entropies must vanish or become negligible for small separations. This argument can also be understood in terms of geometry: Small separations correspond to small curvatures of the sphere and the plane–sphere geometry becomes similar to the plane–plane geometry. This is in fact the main idea of the PFA approximation. As no parameters for which the entropy becomes negative exist in the plane–plane geometry, we expect negative entropies to disappear for small separations. We will investigate this question in more detail in chapter 10.

8. Large-distance limit

In this chapter, we investigate the large-distance limit of the Casimir effect in the plane-sphere geometry. The large-distance limit may also be interpreted as the small-sphere limit. Thus, large separations of sphere and plane correspond to high curvatures of the sphere. We will derive an analytical expression for perfect reflectors which will help us to understand the origin of the occurrence of negative entropies. We will mainly follow the derivation of Refs. [10, 13].

For large separations of plane and sphere $\mathcal{L} \gg R$ the dominant contribution to the free energy comes from the dipole moment $\ell = 1$. The matrix elements become small and we may approximate the logarithm of the determinant of the scattering matrix by the trace of the round-trip matrix

$$\ln \det(\mathbb{1} - \mathcal{M}^{(m)}) \approx - \sum_{P=E,M} \mathcal{M}_{1,1}^{(m)}(P, P). \quad (8.1)$$

The free energy simplifies to

$$\mathcal{F}_{\text{LD}} = -\frac{T}{\pi} \sum_{n=0}^{\infty} \left[\frac{1}{2} \mathcal{M}_{1,1}^{(0)}(E, E) + \frac{1}{2} \mathcal{M}_{1,1}^{(0)}(M, M) + \mathcal{M}_{1,1}^{(1)}(E, E) + \mathcal{M}_{1,1}^{(1)}(M, M) \right], \quad (8.2)$$

whereas the first two summands enclosed within the brackets correspond to $m = 0$ and are weighted by a factor $1/2$. The matrix elements $\mathcal{M}_{1,1}^{(m)}(P, P)$ contain the prefactor $\Lambda_{1,1}^{(m)}$, the integrals $A_{1,1,p}^{(m)}$ and $B_{1,1,p}^{(m)}$, and the Mie coefficients a_1 and b_1 . The Mie coefficients are evaluated at the argument $\chi = nTR/\mathcal{L}$ and may be approximated by the low frequency limit (3.34)

$$a_1^{\text{perf}} \simeq -\frac{2}{3} \left(\frac{nTR}{\mathcal{L}} \right)^3, \quad b_1^{\text{perf}} \simeq \frac{1}{3} \left(\frac{nTR}{\mathcal{L}} \right)^3. \quad (8.3)$$

The values of Λ are given by

$$\Lambda_{1,1}^{(0)} = -\frac{3}{2}, \quad \Lambda_{1,1}^{(1)} = -\frac{3}{4}, \quad (8.4)$$

and the integrals can easily be evaluated analytically

$$\begin{aligned} A_{1,1,p}^{(0)} &= 0, & A_{1,1,p}^{(1)} &= -r_p \frac{e^{-2nT}}{2nT}, \\ B_{1,1,p}^{(0)} &= r_p \frac{(2nT + 1) e^{-2nT}}{4n^3 T^3}, & B_{1,1,p}^{(1)} &= r_p \frac{(2n^2 T^2 + 2nT + 1) e^{-2nT}}{4n^3 T^3}. \end{aligned} \quad (8.5)$$

By inserting (8.3), (8.4) and (8.5) into (8.2) the free energy simplifies to an infinite sum over the

Matsubara frequencies $\xi_n = nT$. The sum can be evaluated analytically and one obtains an expression for the free energy. However, in order to understand the origin of negative entropies, we split the free energy in contributions regarding polarization.

Following an idea of G.-L. INGOLD, we calculate the free energy separately for the contributions

$$\mathcal{F}_{\text{LD}} = -\frac{T}{\pi} \sum_{n=0}^{\infty} \left[\sum_{m=0}^1 \sum_{P=\text{E,M}} \sum_{p=\text{TE,TM}} \mathcal{M}_{1,1,p}^{(m)} \right] = \sum_{m=0}^1 \sum_P \sum_p \mathcal{F}_{P \rightarrow p \rightarrow P}^{(m)}. \quad (8.6)$$

So, we split up the free energy in eight contributions. The infinite sums can be evaluated using (B.33)–(B.35). For $m = 0$ we find

$$\mathcal{F}_{\text{E} \rightarrow \text{TM} \rightarrow \text{E}}^{(0)} = -\frac{T}{16\pi} \left(\frac{R}{\mathcal{L}} \right)^3 \frac{T + \sinh T \cosh T}{\sinh^2 T}, \quad (8.7)$$

$$\mathcal{F}_{\text{E} \rightarrow \text{TE} \rightarrow \text{E}}^{(0)} = 0, \quad (8.8)$$

$$\mathcal{F}_{\text{M} \rightarrow \text{TM} \rightarrow \text{M}}^{(0)} = 0, \quad (8.9)$$

$$\mathcal{F}_{\text{M} \rightarrow \text{TE} \rightarrow \text{M}}^{(0)} = \frac{1}{2} \mathcal{F}_{\text{E} \rightarrow \text{TM} \rightarrow \text{E}}^{(0)}, \quad (8.10)$$

and for $m = 1$

$$\mathcal{F}_{\text{E} \rightarrow \text{TM} \rightarrow \text{E}}^{(1)} = -\frac{T}{16\pi} \left(\frac{R}{\mathcal{L}} \right)^3 \left[\frac{\cosh T}{\sinh T} + \frac{T}{\sinh^2 T} + T^2 \frac{\cosh T}{\sinh^3 T} \right], \quad (8.11)$$

$$\mathcal{F}_{\text{E} \rightarrow \text{TE} \rightarrow \text{E}}^{(1)} = -\frac{T^3}{16\pi} \left(\frac{R}{\mathcal{L}} \right)^3 \frac{\cosh T}{\sinh^3 T}, \quad (8.12)$$

$$\mathcal{F}_{\text{M} \rightarrow \text{TM} \rightarrow \text{M}}^{(1)} = \frac{1}{2} \mathcal{F}_{\text{E} \rightarrow \text{TE} \rightarrow \text{E}}^{(1)}, \quad (8.13)$$

$$\mathcal{F}_{\text{M} \rightarrow \text{TE} \rightarrow \text{M}}^{(1)} = \frac{1}{2} \mathcal{F}_{\text{E} \rightarrow \text{TM} \rightarrow \text{E}}^{(1)}. \quad (8.14)$$

The polarization TM on the plane corresponds to the polarization E on the sphere, and TE on the plane corresponds to M on the sphere.

Adding the contributions of $m = 0$ and $m = 1$ for the contributions without change of polarization yields

$$\mathcal{F}_{\text{E} \rightarrow \text{TM} \rightarrow \text{E}} = \frac{-T}{16\pi \sinh^3 T} \left(\frac{R}{\mathcal{L}} \right)^3 \left[2 \cosh T \sinh^2 T + 2T \sinh T + T^2 \cosh T \right], \quad (8.15)$$

$$\mathcal{F}_{\text{M} \rightarrow \text{TE} \rightarrow \text{M}} = \frac{1}{2} \mathcal{F}_{\text{E} \rightarrow \text{TM} \rightarrow \text{E}}. \quad (8.16)$$

Both contributions differ by a factor of 2 with $\mathcal{F}_{\text{M} \rightarrow \text{TE} \rightarrow \text{M}}$ being larger in amount. The two contributions to the free energy are depicted in Fig 8.1 a). The contributions to the free energy have zero slope for $T = 0$ and decrease linear for high temperatures. As the slope of the functions are negative for arbitrary temperatures, the contributions to the entropy are positive. Moreover, the contributions to the entropy become constant for high temperatures.

8. Large-distance limit

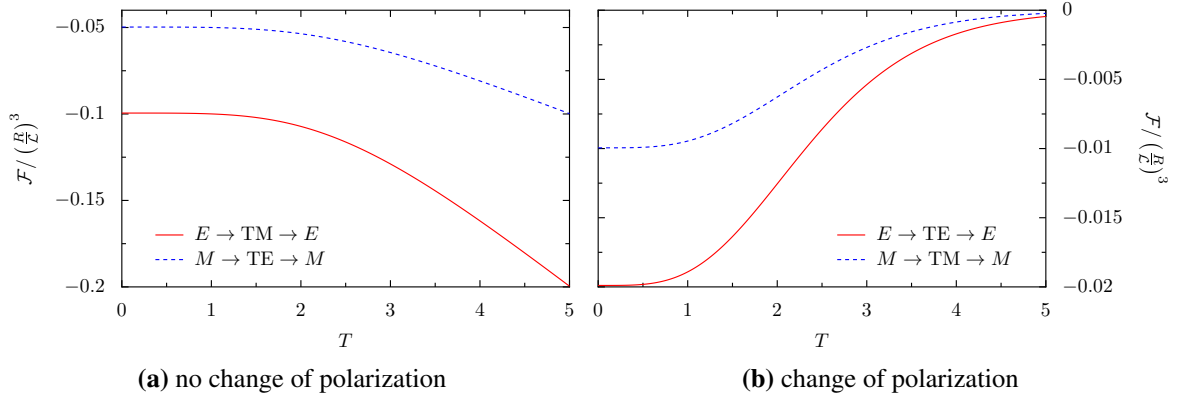


Figure 8.1.: Contributions to the free energy in the large-distance limit for a) no change of polarization and b) change of polarization. The solid and dashed lines differ by a factor of 2. The contributions in a) decrease and yield a positive contribution to the entropy. The contributions in b) increase and thus yield a negative contribution to the entropy.

Adding the contributions of $m = 0$ and $m = 1$ for the contributions with change of polarization yields

$$\mathcal{F}_{E \rightarrow TE \rightarrow E} = \frac{-T^3}{16\pi} \left(\frac{R}{\mathcal{L}}\right)^3 \frac{\cosh T}{\sinh^3 T}, \quad (8.17)$$

$$\mathcal{F}_{M \rightarrow TM \rightarrow M} = \frac{1}{2} \mathcal{F}_{E \rightarrow TE \rightarrow E}. \quad (8.18)$$

Once more both contributions differ by a factor of 2 with $\mathcal{F}_{E \rightarrow TE \rightarrow E}$ being larger in amount. The two contributions to the free energy are depicted in Fig 8.1 b). Also, the contributions to the free energy have slope zero for $T = 0$. However, the functions increase and tend to zero for high temperatures. Thus, the contribution to the entropy is zero for $T = 0$, negative for intermediate temperatures, and tends to zero for high temperatures.

We see that the terms with a change of polarization yield a positive contribution to the entropy. This means that the change of polarization is the reason of negative entropies in the plane-sphere geometry. This is certainly true in the large-distance limit and at least reasonable for arbitrary separations. For perfect reflectors the entropy is always non-negative in the plane-plane geometry. For this reason, the entropy in the proximity force approximation (PFA) is also non-negative. However, we have seen in the last chapter that for small separations of sphere and plane the PFA becomes accurate. Therefore the entropy must become non-negative or at least arbitrary small. As the PFA neglects contributions due to polarization changes, it is thus at least reasonable that negative entropies are associated with polarization changes.

By summation of all contributions we obtain for the free energy

$$\mathcal{F}_{LD} = -\frac{3T}{16\pi} \left(\frac{R}{\mathcal{L}}\right)^3 \frac{T \sinh T + \cosh T (T^2 + \sinh^2 T)}{\sinh^3 T}. \quad (8.19)$$

Interestingly, the effects due to finite temperature and curvature are separated in this limit. For low

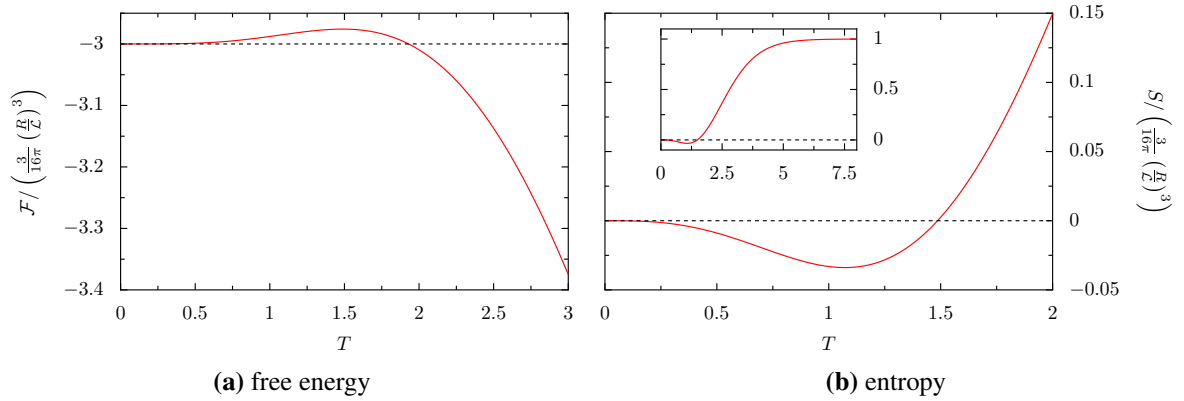


Figure 8.2.: We plot a) the free energy and b) the entropy dependent on T . The free energy increases for small temperatures to a local maximum and decreases afterwards, thus yielding negative entropies for $0 < T \lesssim 1.48584$.

temperatures (8.19) can be approximated by a Taylor series and we find

$$\mathcal{F}_{\text{LD}}^{\text{LT}} \approx -\frac{9}{16\pi} \left(\frac{R}{\mathcal{L}}\right)^3 \left(1 - \frac{T^4}{135} + \frac{4T^6}{945} - \frac{T^8}{945}\right). \quad (8.20)$$

The first finite temperature correction is positive and thus yields a negative contribution to the entropy. Also, for large separations the factor R/\mathcal{L} decreases and the free energy, the force and the entropy become small. For high temperatures one obtains

$$\mathcal{F}_{\text{LD}}^{\text{HT}} \approx -\frac{3T}{16\pi} \left(\frac{R}{\mathcal{L}}\right)^3. \quad (8.21)$$

In the high temperature limit the free energy decreases proportional to the temperature, thus yielding a positive and constant entropy.

The free energy and the entropy are depicted in Fig. 8.2. For low temperatures the free energy increases up to a maximum at $T \approx 1.48584$ and decreases for higher temperatures. In the high temperature limit the function decreases proportional to the temperature. The maximum of the free energy yields negative entropies in the range $0 \leq T \lesssim 1.48584$. As the effect of negative entropies is caused by a change of polarization, we may assume that the entropy is always positive for temperatures $T \gtrsim 1.48584$. We will verify this assumption in chapter 10.

9. Thermal effects

In this chapter, we put a focus on thermal effects. For low temperatures we find the entropy to be negative for separations $L/R \gtrsim 0.04$. The numerical results suggest that the entropy is still negative for smaller separations and vanishes for $L/R \rightarrow 0$. In the high temperature limit the free energy becomes independent of the particular properties of the metal in the Drude model. This enables us to study this limit for perfect reflectors as well as Drude mirrors. We compare our numerical results with expressions obtained by PFA and various suggested expansion of the free energy for small separations. In the last section, we investigate thermal effects for perfect mirrors at intermediate separations.

9.1. Low temperatures

The expansion of the free energy for low temperatures is given by

$$\mathcal{F}(T) \approx a + bT^4. \quad (9.1)$$

The coefficient a corresponds to the free energy at $T = 0$

$$a \equiv \mathcal{F}(T = 0), \quad (9.2)$$

and b to the low temperature entropy divided by $-4T^3$:

$$S = -\frac{\partial \mathcal{F}}{\partial T} = -4bT^3 \quad \Rightarrow \quad b = -\frac{S}{4T^3} \quad (9.3)$$

We have derived analytical expressions for the free energy for small separations (7.7) using the PFA approximation in chapter 7, and for large separations (8.20) using the dipole approximation in chapter 8. In order to obtain a and b for arbitrary separations, the free energy is computed numerically for 20 temperatures in the range $T = 0.05 \dots 0.25$. The coefficients a and b are then obtained using linear regression in the variable T^4 .

In order to obtain meaningful results it is important to discuss the reliability and the accuracy of the fit parameters a and b . On the one hand, the points $P_i = (T_i, \mathcal{F}(T_i))$ used for the fit must not be computed for too high temperatures, because (9.1) is only valid for small temperatures. On the other hand, for low temperatures the free energy hardly changes. For the numerical computation we used $\epsilon_p = 10^{-10}$ and $\ell_{\max} = \max(25, \lceil \eta L/R \rceil)$, where $\eta = 6.2$. For separations $L/R \geq 1$ this yields a very high accuracy of about 10^{-8} – 10^{-9} . However, for smaller separations the accuracy is limited by the choice of ℓ_{\max} and is in the order of 10^{-4} – 10^{-5} . Fig. 9.1 shows two fits for $L/R \approx 0.05$ and $L/R \approx 1.0$.

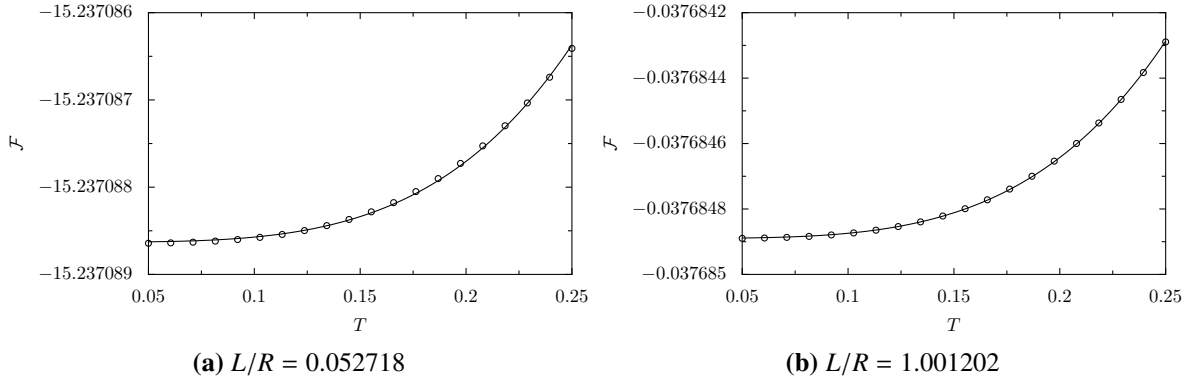


Figure 9.1.: Low temperature fits for the free energy using $\mathcal{F} \approx a + bT^4$ for a) $L/R \approx 0.05$ and b) $L/R \approx 1$. The points correspond to numerical data, the solid lines to (9.1) with parameters a and b obtained using linear regression.

The agreement of the numerical points and the fit functions are in both cases good. However, the deviation of the fits from the numerical points becomes stronger for smaller separations.

The change of the free energy in Fig. 9.1 a) is smaller than the accuracy of the free energy. Nevertheless, the following two examples show that this causes no numerical problems. For $L/R = 0.1$ and $L/R = 0.07$ we compare the parameters a and b obtained using $\epsilon_p = 10^{-10}$, $\eta = 6.2$, and a much preciser computation using $\eta = 12.4$.

	$L/R = 0.1$		$L/R = 0.07$	
η	6.2	12.4	6.2	12.4
ℓ_{\max}	62	124	89	178
a	-4.200585	-4.200709	-8.613663	-8.613869
b	$6.279343 \cdot 10^{-4}$	$6.279350 \cdot 10^{-4}$	$6.094080 \cdot 10^{-4}$	$6.094146 \cdot 10^{-4}$

Both parameters a and b hardly change and we see that $\eta = 6.2$ yields satisfactory results. The reason for this is as following: The accuracy is not limited by ϵ_p , but by the choice of η . For increasing values of η the computed free energy converges monotonic to the exact free energy. The convergence hardly depends on the temperature (cf. Fig 6.1) and thus the points used for the fits are shifted in the order of the accuracy. Therefore, the accuracy of a and b is in the order of the free energy.

In Fig. 9.2 we plot the free energy and the entropy for $T = 0$ versus the separation. For small separations the free energy coincides with the approximation obtained by the PFA, and for large separations the free energy coincides with the approximation obtained in the large-distance limit. The entropy for low temperatures is negative for separations $0.036 \leq L/R \leq 10$. For large separations the parameter b is given by (cf. (8.20))

$$b = \frac{1}{240\pi} \left(\frac{R}{\mathcal{L}} \right)^3 = \frac{1}{240\pi (1 + L/R)^3}. \quad (9.4)$$

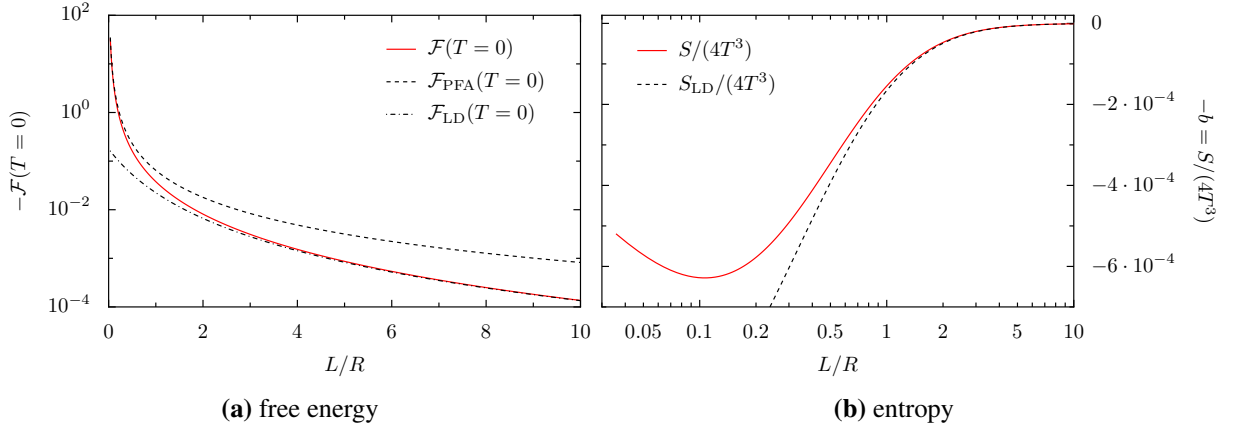


Figure 9.2.: We plot a) the free energy and b) the low temperature entropy versus the separation of plane and sphere. For small separations the free energy coincides with the PFA result, for large separations the free energy coincides with the large-distance limit. For large separations the entropy tends to zero, for smaller separations it decreases and reaches a minimum at $L/R \approx 0.104$ and $S/(4T^3) \approx 6.28 \cdot 10^{-4}$.

Thus the entropy is negative and tends to zero for $L/R \rightarrow \infty$. The entropy reaches a minimum at $L/R \approx 0.104$ and $S/(4T^3) \approx -6.28 \cdot 10^{-4}$. In the PFA approximation the Casimir entropy is always positive. As the PFA is a good approximation for small separations, it is plausible that the entropy tends to zero for $L/R \rightarrow 0$.

9.2. High temperatures

For perfect reflectors the free energy is a universal function depending only on the temperature T and the ratio $x = L/R$. In this section, we study the high temperature limit of the Casimir effect. In this limit the free energy is dominated by the $n = 0$ term and higher Matsubara frequencies may be neglected. The matrix elements of the scattering operator are given by the analytical expressions (5.70) and (5.71). These expressions are also for Drude metals independent of the particular properties of the metal. For this reason, the free energy only depends on temperature and separation in the high temperature limit. This, however, is not true for the plasma model, because the Fresnel coefficient r_{TE} still depends on ω_p and κ for $\xi \rightarrow 0$. Moreover, the numerical evaluation of the free energy in the high temperature limit is considerably simpler than for low and intermediate temperatures. This enables us to study notably smaller separations. In this section, we will mainly follow Ref. [12].

In the high temperature limit we may only consider the $n = 0$ term and the free energy becomes

$$\mathcal{F}^{\text{HT}}(T, L/R) = \frac{T}{2\pi} \sum_m' \mathcal{D}^{(m)}(nT=0). \quad (9.5)$$

As the free energy depends linear on the temperature, the entropy becomes constant. The scattering

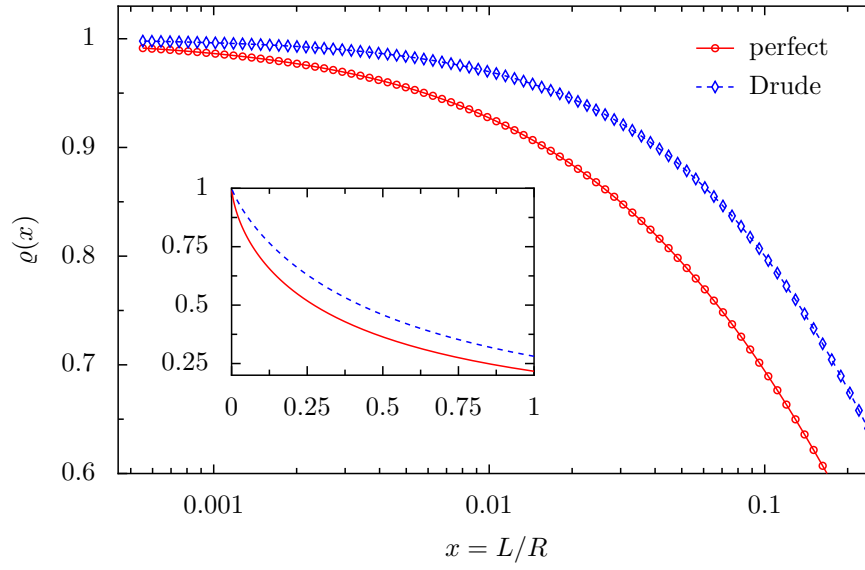


Figure 9.3.: The ratio ϱ of the exact free energy and the PFA approximation in the Drude model and for perfect reflectors versus the separation L/R . The inset shows ϱ for separations up to $L/R = 1$.

matrices $\mathcal{D}^{(m)}$ depend on the ratio $x = L/R$ and we are lead to define

$$\mathcal{F}^{\text{HT}}(T, L/R) = \frac{T}{2\pi} \Phi(L/R), \quad \Phi(L/R) \equiv \sum_m \mathcal{D}^{(m)}(nT = 0). \quad (9.6)$$

The function Φ is universal in the Drude model and for perfect reflectors, however, both functions are not identical. We will distinguish both functions using superscripts “D” for Drude model and “P” for perfect reflectors.

With (7.8) and (7.9) the ratio of the exact result and the PFA approximation is given by

$$\varrho^{\text{D,P}}(x) \equiv \frac{\mathcal{F}^{\text{HT}}}{\mathcal{F}^{\text{PFA}}} = -\frac{x \Phi^{\text{D,P}}}{C^{\text{D,P}}}, \quad C^{\text{D}} \equiv \frac{\xi(3)}{8}, \quad C^{\text{P}} \equiv \frac{\xi(3)}{4}, \quad (9.7)$$

where we have used the approximated PFA results. The discrepancy between the ratio ϱ for Drude and perfect mirrors is caused by the different behaviour of r_{TE} for $\xi \rightarrow 0$. In Fig. 9.3 the ratio ϱ versus the separation $x = L/R$ is plotted. The ratio ϱ tends to one for separations $x \rightarrow 0$. For a given ratio L/R the accuracy of the PFA is better for the Drude model than for perfect reflectors. The accuracy of the leftmost points $L/R \approx 5.53 \cdot 10^{-4}$ is only $\varrho^{\text{P}} \approx 0.9914$ for perfect reflectors, but $\varrho^{\text{D}} \approx 0.9979$ for Drude mirrors. In Fig. 9.4 a) we plot the universal function $\Phi(x)$ for the Drude model and perfect reflectors. For perfect reflectors $-\Phi$ is greater than for Drude mirrors. The ratio $\Phi^{\text{P}}/\Phi^{\text{D}}$ tends to 2 for $L/R \rightarrow 0$ and reaches a value of $3/2$ for $L/R \rightarrow \infty$ [13]. The numerical results were obtained using $\epsilon_p = 5 \cdot 10^{-9}$ and $\eta = 8$, for the leftmost point $\ell_{\text{max}} = 14465$ was used for the calculation.

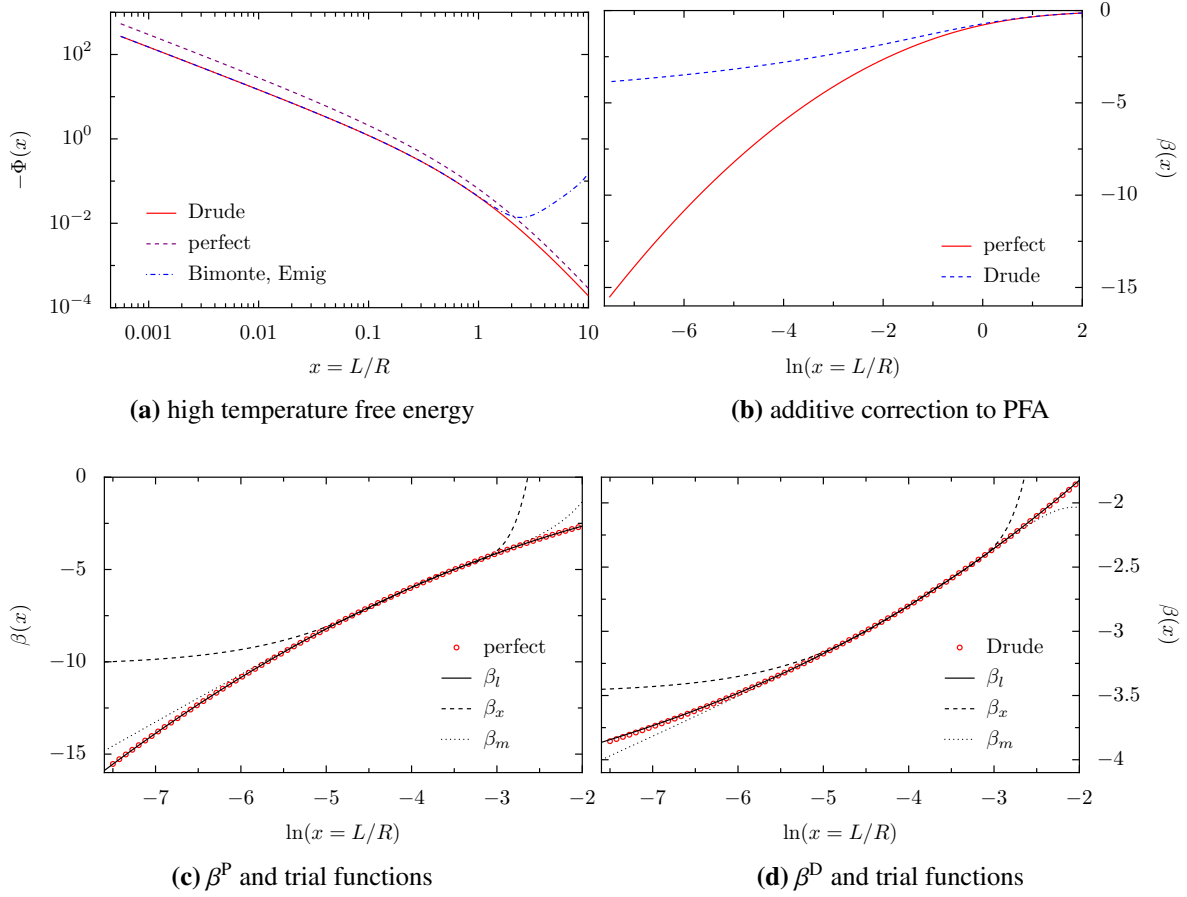


Figure 9.4.: In a) we show the universal function $-\Phi(x)$ versus the separation $x = L/R$ for the Drude model and for the model of perfect reflectors. The function $\Phi = 2\pi\mathcal{F}/T$ is proportional to the free energy. We also plot an expansion of Φ for small separations derived by BIMONTE and EMIG [5]. In b) the additive correction β to PFA is plotted for Drude mirrors and perfect reflectors in the range $-7.5 \leq \ln(L/R) \leq 2$. We plot the function $\beta(x)$ together with the trial functions β_l , β_x and β_m in c) for perfect reflectors and in d) for the Drude model.

Following an idea of CANAGUIER–DURAND, INGOLD, JACKEL et al. [12], we express the ratio ϱ by

$$\beta^{\text{D,P}}(x) \equiv \frac{\varrho^{\text{D,P}}(x) - 1}{x}, \quad (9.8)$$

where $\beta^{\text{D,P}}$ corresponds to an additive correction to PFA

$$\Phi^{\text{D,P}}(x) = -C^{\text{D,P}} \left(\frac{1}{x} + \beta^{\text{D,P}}(x) \right). \quad (9.9)$$

The functions $\beta^{\text{D,P}}$ are depicted in Fig. 9.4 b) in the range $-7.5 \leq L/R \leq 2$. For large separations the functions β^{D} and β^{P} coincide. For the function β we consider following trial functions:

$$\beta_l(x) = a_0 + a_1 \ln x + a_2 \ln^2 x + a_3 \ln^3 x \quad (9.10)$$

$$\beta_x(x) = b_0 + b_1 x + b_2 x^2 + b_3 x^3 \quad (9.11)$$

$$\beta_m(x) = c_0 + c_1 \ln x + c_2 x + c_3 x^2 \quad (9.12)$$

The first function is a polynomial in the variable $\ln x$, the second function is a polynomial in x , and the last function is a mixed form that results from the assumption that the force in the high temperature limit can be expressed as a Laurent series in x . The parameters are obtained from the numerical results using fits in the interval $\ln x \in [-5, -3]$. In total, 27 points were used for the fits. The function β and the trial functions β_l , β_x and β_m are depicted in Fig. 9.4 for c) perfect reflectors and d) for the Drude model. The fit parameters for the trial functions for perfect reflectors are

$$\begin{aligned} a_0^{\text{P}} &= -0.824834, & a_1^{\text{P}} &= 0.545277, & a_2^{\text{P}} &= -0.181948, & a_3^{\text{P}} &= 0.000932, \\ b_0^{\text{P}} &= -10.187688, & b_1^{\text{P}} &= 364.692140, & b_2^{\text{P}} &= -8750.230389, & b_3^{\text{P}} &= 78825.984591, \\ c_0^{\text{P}} &= 5.222405, & c_1^{\text{P}} &= 2.634690, & c_2^{\text{P}} &= -40.064506, & c_3^{\text{P}} &= 226.000366, \end{aligned}$$

and for the Drude model

$$\begin{aligned} a_0^{\text{D}} &= -0.474404, & a_1^{\text{D}} &= 0.780873, & a_2^{\text{D}} &= 0.056193, & a_3^{\text{D}} &= 0.001597, \\ b_0^{\text{D}} &= -3.478220, & b_1^{\text{D}} &= 53.680980, & b_2^{\text{D}} &= -1075.234122, & b_3^{\text{D}} &= 9158.452023, \\ c_0^{\text{D}} &= -1.715240, & c_1^{\text{D}} &= 0.301137, & c_2^{\text{D}} &= 7.149318, & c_3^{\text{D}} &= -37.457065. \end{aligned}$$

The trial functions β_x and β_m behave similar for perfect reflectors and in the Drude model. The numerical results show that β_x coincides with β only in a small window. The function β_m agrees with β in a broader domain, but it also differs significantly from β for small separations. Therefore β cannot be expressed as a polynomial in x , and the assumption that the force can be expressed as a Laurent series in x is not valid in general. The trial function β_l behaves different for perfect reflectors and in the Drude model. For perfect reflectors β_l is in perfect agreement with β for small separations. For the Drude model β_l is still in good agreement, however, the trial function differs from β noticeably for small separations. So, the numerical results suggest that β can be approximated by a polynomial in $\ln x$ for perfect reflectors, but not in the Drude model. Our results are in agreement with [12], however, as we arrive at smaller separations, we can also show that β_l differs from β for the Drude model.

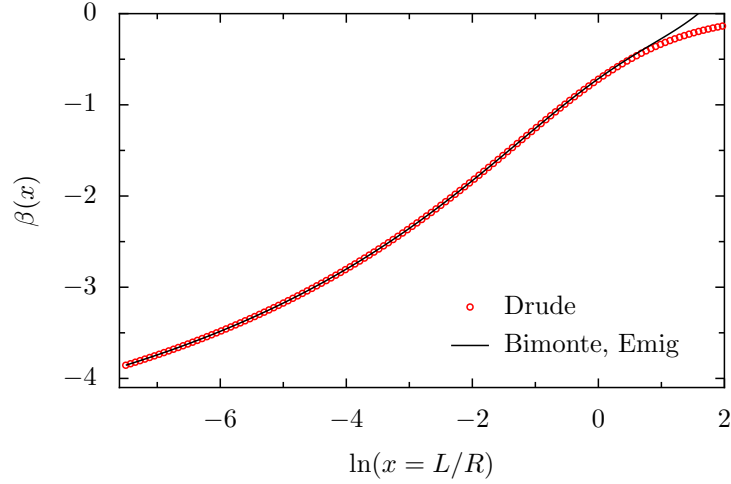


Figure 9.5.: Additive correction β to the PFA and the approximation given by BIMONTE and EMIG [5]. Both functions are in perfect agreement for small separations.

Moreover, we want to compare our numerical results with an analytical expression of the free energy derived by BIMONTE and EMIG for Drude metals [5]. This expression is supposed to be valid for small separations in the high temperature limit. The function Φ is given by

$$\Phi_{\text{BE}}^{\text{D}}(x) = \frac{1}{2} \left[-\frac{\xi(3)}{2\mu^2} + \frac{\ln \mu}{12} + \frac{1}{8} - \gamma_0 - \frac{7\mu^2}{2880} - \frac{31\mu^4}{725760} \right. \\ \left. \ln(\gamma_1 - \ln \mu) + \frac{-\gamma_2 + \ln \mu}{-\gamma_1 + \ln \mu} \frac{\mu^2}{6} - \frac{\gamma_3 - \gamma_4 \ln \mu + \ln^2 \mu}{(-\gamma_1 + \ln \mu)^2} \frac{\mu^4}{180} + \mathcal{O}(\mu^6) \right], \quad (9.13)$$

where

$$\mu \equiv \ln(1 + x + \sqrt{x(2+x)}). \quad (9.14)$$

The constants $\gamma_0 = 0.174897$, $\gamma_1 = 0.1270362$, $\gamma_2 = 1.35369$, $\gamma_3 = 1.59409$ and $\gamma_4 = 2.51153$ are given by integrals, but BIMONTE and EMIG give only an expression for the integral of γ_0 . Fig. 9.5 shows β^{D} and the function $\beta_{\text{BE}}^{\text{D}}$ obtained from $\Phi_{\text{BE}}^{\text{D}}$. Both functions are for small separations in perfect agreement. In Fig. 9.4 a) the free energy in terms of Φ is plotted with the approximation (9.13) obtained by BIMONTE and EMIG.

9.3. Intermediate temperatures

For intermediate temperatures we have to rely on numerical results. In Fig. 9.6 the ratio $\mathcal{F}(T)/\mathcal{F}(T=0)$ is depicted in the range $0.25 \leq L/R \leq 5$ and $0.5 \leq T \leq 2$. In Fig. 9.7 we plot the ratio $\mathcal{F}(T)/\mathcal{F}(T=0)$ for various separations L/R dependent on T . For a constant separation L/R the ratio first decreases for increasing temperatures, reaches a minimum, and increases afterwards. As the free energy is negative, a minimum of the ratio $\mathcal{F}(T)/\mathcal{F}(T=0)$ corresponds to a maximum of the free energy and

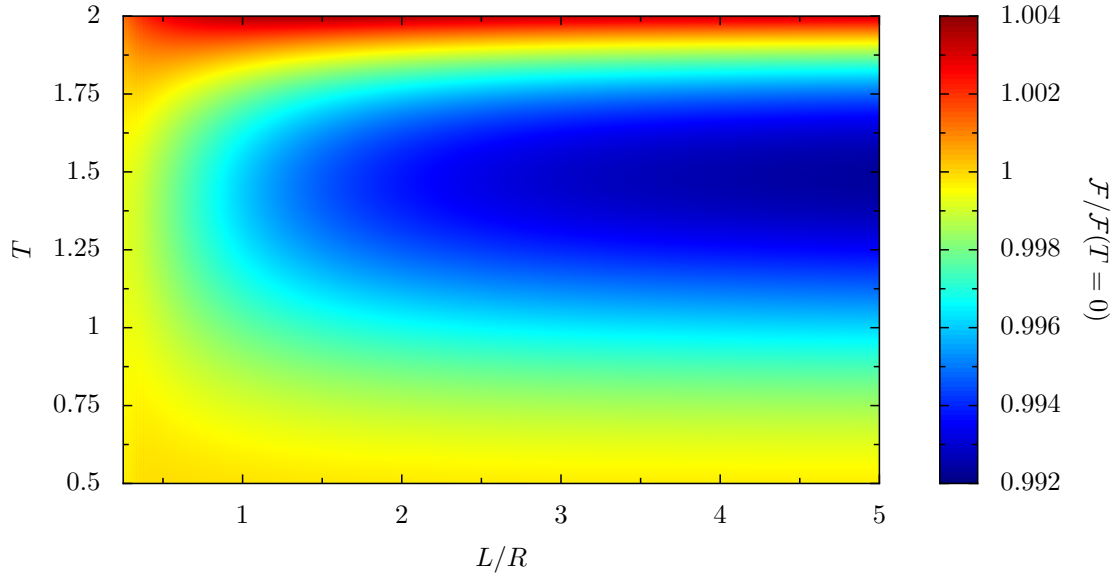


Figure 9.6.: $\mathcal{F}(T)/\mathcal{F}(T=0)$ in the range $0.25 \leq L/R \leq 5$ and $0.5 \leq T \leq 2$.

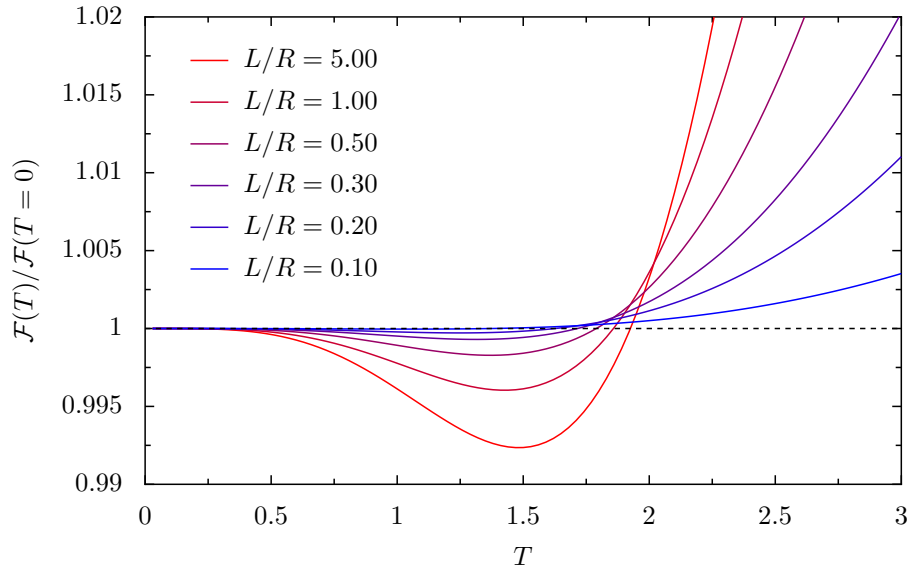


Figure 9.7.: $\mathcal{F}(T)/\mathcal{F}(T=0)$ for various separations dependent on temperature.

thus to $S = 0$. For large values of L/R we find the large-distance limit: The maximum of the free energy is located at $T \approx 1.5$ in accordance with the results of chapter 8. For smaller separations the minimum is reached at temperatures lower than $T \approx 1.5$. We also see that the thermal increase of the free energy is an effect in the order of per mille. Moreover, the effect becomes more evident for large separations.

The numerical results were obtained using $\epsilon_p = 10^{-8}$, $\ell_{\max} = \max(20, \lfloor \eta R/L \rfloor)$ with $\eta = 6$. The separations between two point is $\Delta_T \approx 0.0031$ and $\Delta_{L/R} \approx 0.0045$. The numerical data was converted using bilinear interpolation to a resolution of 1000x1000 points in Fig. 9.6.

10. Negative entropies

In the last chapters, we have found that parameters for which the entropy becomes negative exist in the plane–plane as well as in the plane–sphere geometry. In the plane–plane geometry negative entropies do not occur for perfect reflectors and are thus caused by effects due to finite conductivity and plasma oscillations of the metals. In contrast to this, negative entropies are found in the plane–sphere geometry for perfect reflectors thus suggesting a geometrical origin. In the large–distance limit we showed that the root of the effect is due to a change of polarizations and the entropy is always positive for temperatures higher than $T \approx 1.5$. Throughout this chapter, we will denote the temperature for fixed separation for which the entropy changes its sign by $T_S(L/R)$. For smaller separations the effect becomes less pronounced and our numerical results suggest that $T_S(L/R)$ tends to zero for $L/R \rightarrow 0$. This assumption is also strengthened by the PFA approximation. On the one hand, the PFA yields positive values for the entropy for arbitrary separations and temperatures. On the other hand, the approximation becomes accurate for small separations. For these reasons, we expect negative entropies to disappear for small separations. This argument can also be restated in terms of geometry. For small separations the curvature of the sphere becomes small and the geometry becomes similar to the plane–plane geometry. As the curvature becomes small, changes of polarization may be neglected and the effect of negative entropies vanishes.

We now study the effect of negative entropies for arbitrary separations and temperatures. In Fig. 10.2 a) we plot the entropy dependent on separation and temperature in the range $0.03415 \leq L/R \leq 1$ and

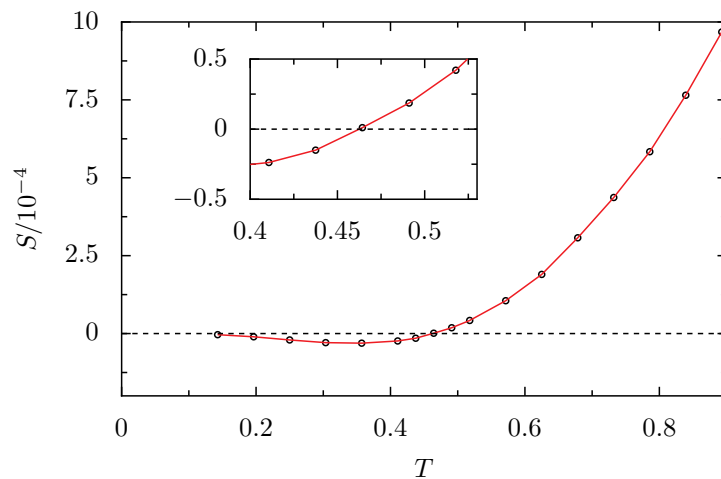
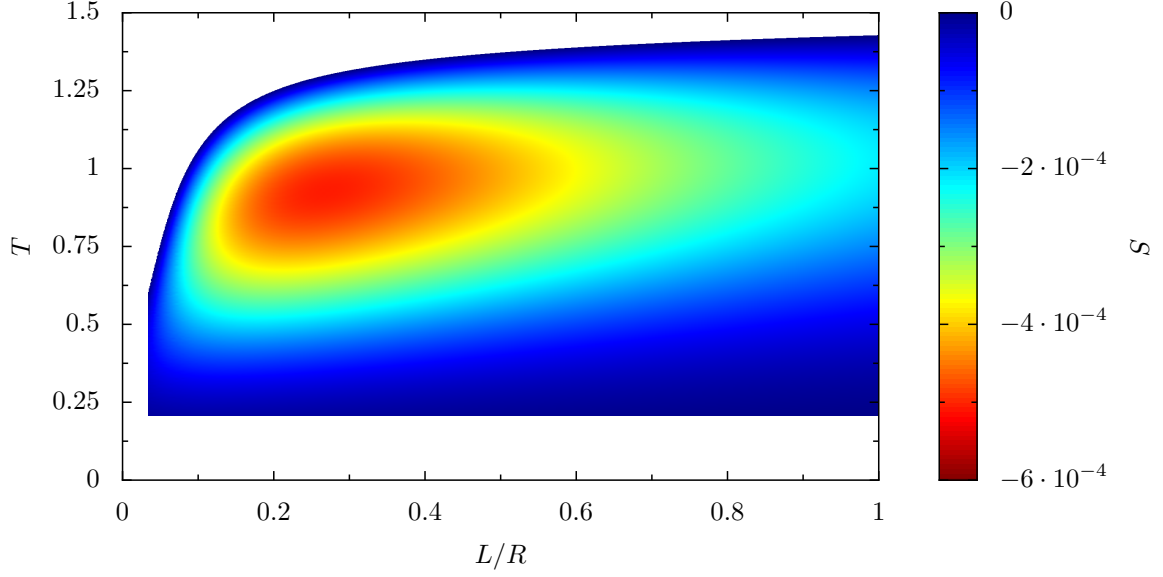
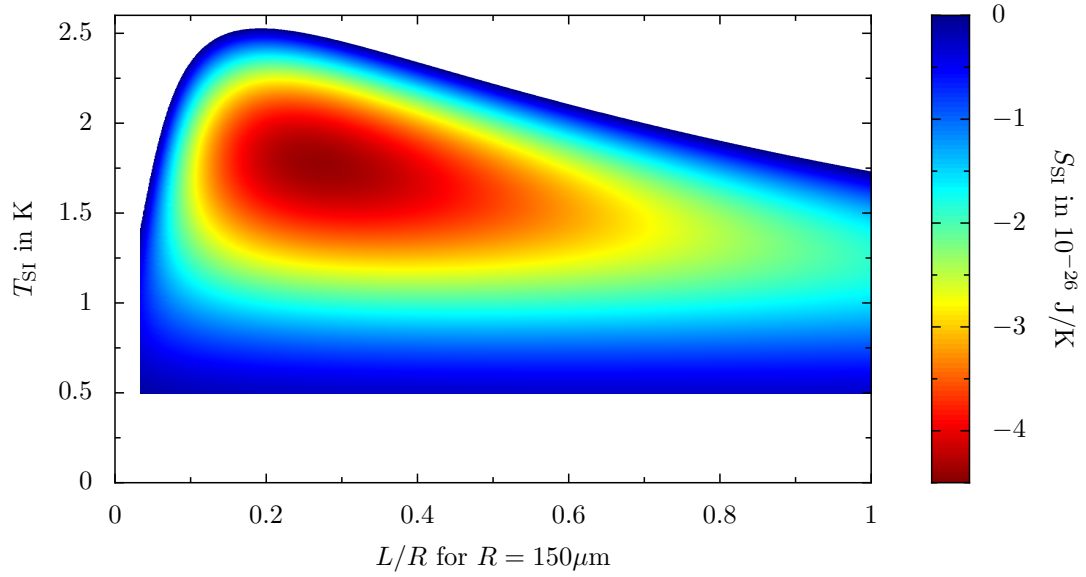


Figure 10.1.: Entropy for S for $L/R = 0.02$ dependent on temperature. We find negative entropies for temperatures $T \lesssim 0.46$. ($\epsilon_p = 10^{-8}$, $\ell_{\max} = 300$)



(a) Negative entropy in scaled units for $0.207 \leq T \leq 1.5$.



(b) Negative entropy in SI units for $R = 150\mu\text{m}$ and $0.5\text{K} \leq T_{\text{SI}} \leq 2.6\text{K}$

Figure 10.2.: Negative entropy dependent on temperature T and separation L/R . The entropy is plotted a) in scaled units and b) in SI units for a sphere of radius $R = 150\mu\text{m}$ for separations $0.03415 \leq L/R \leq 1$ and temperatures according to subcaptions. White areas within this range correspond to positive values of the entropy. The minimum is located at $L/R = 0.270$ and a) $T = 0.927$, and b) $T_{\text{SI}} = 1.77\text{K}$.

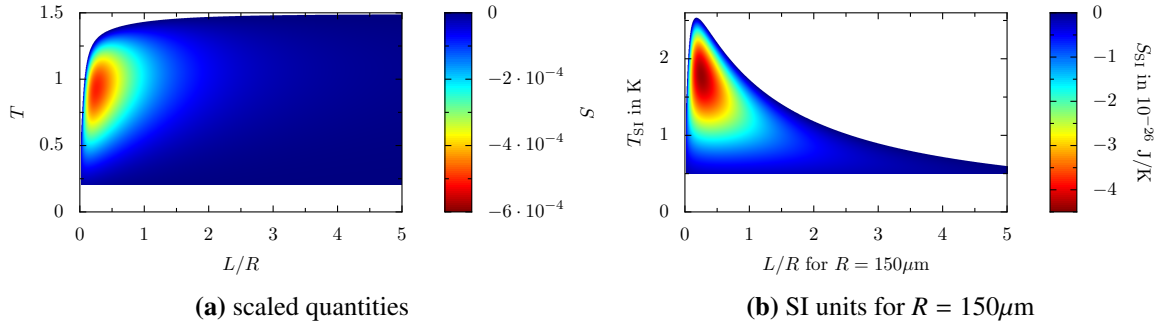


Figure 10.3.: Negative entropies for a) scaled quantities and b) in SI units for separations up to $L/R = 5$.

$0.207 \leq T \leq 1.5$. White areas within this range correspond to positive entropies. For large separations we rediscover the results of the large-distance limit and the entropy is negative for temperatures lower than $T < T_S(L/R) \approx 1.49$. Fig. 10.3 a) shows the same plot for separations up to $L/R = 5$. For smaller separations $T_S(L/R)$ decreases, while the absolute values of the negative entropies increase down to $L/R \approx 0.3$. This may be understood as a result of two competing effects: On the one hand, negative entropies are more distinct for large separations, or small spheres respectively. In other words, the decrease of the ratio $\mathcal{F}/\mathcal{F}(T = 0)$ is stronger for large separations (cf. Fig. 9.6). On the other hand, the free energy decreases with larger separations. Consequently, the effect of negative entropies increases with separation, but at the same time the Casimir effect becomes less pronounced. We find a minimum of the entropy for $L/R \approx 0.270$ and $T \approx 0.927$. For smaller separations $T_S(L/R)$ continues to decrease. For $L/R \approx 0.034$ we find negative entropies for temperatures $T_S \lesssim 0.60$. Because of the arguments stated in the previous paragraph, it seems plausible that $T_S(L/R)$ tends to zero for $L/R \rightarrow 0$. This assumption is also strengthened by Fig. 10.1. For $L/R = 0.02$ we find negative entropies for temperatures $T \lesssim 0.46$. The numerical data for Fig. 10.2 and Fig. 10.3 was obtained with identical parameters and resolution as in section 9.3.

In Fig. 10.2 we plot the negative entropy in SI units for a sphere of radius $R = 150\mu\text{m}$ which is a typical size in experiments [33]. We want to remind the reader that quantities measured in SI units are labeled with a subscript “SI”. While the separation L/R remains constant when changing to SI units, the temperature of the minimum of the entropy is now located at $T_{\text{SI}} = 1.77\text{K}$. The minimum in SI units for arbitrary values of R is given by (5.41)

$$T_{\text{SI}} \approx \frac{\hbar c}{2\pi k_B R(1 + L/R)} T = \frac{0.927}{1.270} \frac{\hbar c}{2\pi k_B R}. \quad (10.1)$$

For smaller spheres this temperature increases and corresponds to ambient temperature for $R \approx 1.2\mu\text{m}$. While $T_S(L/R)$ tends to a constant value for large separations in scaled units, $T_S(L/R)$ tends to zero for SI units. This is caused by the scaling (5.41). In SI units the entropy is given by

$$S_{\text{SI}} = -\frac{\partial \mathcal{F}_{\text{SI}}}{\partial T_{\text{SI}}} = -\frac{\hbar c}{\mathcal{L}} \frac{\partial \mathcal{F}}{\partial T} \frac{\partial T}{\partial T_{\text{SI}}} = 2\pi k_B S(T) = 2\pi k_B S\left(T = \frac{2\pi k_B R(1 + L/R)}{\hbar c} T_{\text{SI}}\right). \quad (10.2)$$

For large separations the entropy S is negative for $T \lesssim 1.5$. From this it follows that $T_S(L/R)$ decreases

for large separations like

$$T = \frac{2\pi k_B R(1 + L/R)}{\hbar c} T_{\text{SI}} \lesssim 1.5 \quad \Leftrightarrow \quad T_{\text{SI}} \lesssim 1.5 \frac{\hbar c}{2\pi k_B R(1 + L/R)} \propto \frac{1}{1 + L/R}. \quad (10.3)$$

This can be seen in Fig. 10.3 b) for separations up to $L/R = 5$.

We now address the question about the relevance of negative entropies in the Casimir effect. We have found non-monotonic behaviour of the free energy over a wide range of parameters. However, the definition of the entropy from statistical mechanics claims that the entropy is positive. This contradiction is resolved by the fact that the Casimir free energy is an interaction energy. We are actually only considering a subsystem of the full system [9]. For this reason, the Casimir entropy corresponds to a difference of two entropies. There is no physical reason why the difference of two entropies ought to be positive [26, 41].

11. Conclusion and outlook

In this master thesis, we have studied the Casimir effect in the plane–sphere geometry, in particular with respect to the effect of negative entropies. We have shown that the Maxwell equations in vacuum are equivalent to the source-free vector Helmholtz equation and introduced the plane wave basis and the multipole basis as solutions. Moreover, we have presented the solutions to the scattering problems of electromagnetic waves at a planar, homogenous interface and at a sphere, where the metallic properties of plane and sphere are either described by the Drude model, the plasma model or the model of perfect reflectors. With the Fresnel and Mie coefficients as well as the solutions of the Helmholtz equation at hand, we have applied the scattering approach to the plane–plane and to the plane–sphere geometry. Although equivalent to the matrix elements of DURAND et al. [10, 13], our matrix elements of the scattering matrix in the plane–sphere geometry avoid Wigner D-matrix elements. After changing to scaled quantities the free energy for perfect reflectors depends only on temperature and separation. Also, we have considered analytically the contribution to the free energy of the Matsubara frequency $\xi = 0$, because this special case raises numerical problems. The software implementation of the formulas reveals several serious numerical problems, e.g. the problem of computing the determinant of a matrix whose elements differ by hundreds of orders of magnitude. We have discussed these problems and presented solutions for a fast and stable software implementation.

We have compared our numerical results with the proximity force approximation (PFA) that links the unknown free interaction energy of arbitrary geometries to the well-known energy of the plane–plane geometry. We have shown that indeed the PFA becomes a good approximation in the limit of small separations. As entropies obtained using the PFA are always positive, we have conjectured that the effect of negative entropies vanishes for small separations. This assumption was strengthened by the study of the large–distance limit. We have derived an analytical expression for the free energy in the limit of large separations and have shown that the negative entropies are linked with a change of polarization within a round trip. For low temperatures we showed that the entropy as a function of the separation has a minimum and probably tends to zero for small separations. As the matrix elements of the scattering matrix become independent of the particular properties of the material in the high temperature limit, we have studied this limit for perfect reflectors as well as for Drude mirrors. We have ruled out several suggestions for the free energy at small separations and proofed the validity of an expansion by BIMONTE and EMIG. At last, we have shown that negative entropies exist over a wide range of parameters. In accordance with previous assumptions, we have found that negative entropies disappear for small separations. While the entropy for large separations is negative for (scaled and thus dimensionless) temperatures $T \lesssim 1.5$, the entropy has a minimum for $T \approx 0.927$ and $R/L \approx 0.207$. The smaller the separation the lower is the temperature at which the entropy becomes positive. This

means that the effect of negative entropies is more evident for large separations. In contrast to this, at the same time the Casimir effect becomes less pronounced for large separations.

This master thesis has covered the main aspects of the Casimir effect in the plane–sphere geometry for perfect reflectors. Further studies could focus on effects due to plasma oscillations and finite conductivity of the metallic mirrors. This adds two more length scales and makes the parameter space more complicated, yet more interesting. Moreover, for a more accurate description it is also necessary to consider effects due to corrugations of plane and sphere [34].

A. Special functions

In this chapter, we briefly describe properties of several special functions that we need for various calculations. The functions are not discussed in completeness, the reader finds a more detailed description in Ref. [1].

A.1. Spherical harmonics

The spherical harmonics

$$Y_{\ell m}(\theta, \varphi) = N_{\ell m} P_{\ell}^m(\cos \theta) \frac{e^{im\varphi}}{\sqrt{2\pi}} \quad (\text{A.1})$$

form a complete and orthonormal set of functions on the unit sphere. They depend on two parameters ℓ, m with $\ell \geq 0$ and $-\ell \leq m \leq \ell$. The factor

$$N_{\ell m} = \sqrt{\frac{2\ell + 1}{2} \frac{(\ell - m)!}{(\ell + m)!}} \quad (\text{A.2})$$

is a normalization constant and P_{ℓ}^m are associated Legendre polynomials. The normalization constant for negative values of m can be expressed by positive values of m :

$$N_{\ell, -m} = \frac{(\ell + m)!}{(\ell - m)!} N_{\ell m} \quad (\text{A.3})$$

The spherical harmonics are orthogonal

$$\int Y_{\ell m}^*(\theta, \varphi) Y_{\ell' m'}(\theta, \varphi) d\Omega = \delta_{\ell \ell'} \delta_{mm'} \quad (\text{A.4})$$

and complete

$$\sum_{\ell=0}^{\infty} \sum_{m=-\ell}^{\ell} Y_{\ell m}^*(\theta', \varphi') Y_{\ell m}(\theta, \varphi) = \delta(\varphi - \varphi') \delta(\cos \theta - \cos \theta'). \quad (\text{A.5})$$

The spherical harmonics up to $\ell = 3$ are listed in table A.1.

A. Special functions

$Y_{\ell m}(\theta, \varphi)$	$\ell = 0$	$\ell = 1$	$\ell = 2$	$\ell = 3$
$m = -3$				$\sqrt{\frac{35}{64\pi}} \sin^3 \theta e^{-3i\varphi}$
$m = -2$			$\sqrt{\frac{15}{32\pi}} \sin^2 \theta e^{-2i\varphi}$	$\sqrt{\frac{105}{32\pi}} \sin^2 \theta \cos \theta e^{-2i\varphi}$
$m = -1$		$\sqrt{\frac{3}{8\pi}} \sin \theta e^{-i\varphi}$	$\sqrt{\frac{15}{8\pi}} \sin \theta \cos \theta e^{-i\varphi}$	$\sqrt{\frac{21}{64\pi}} \sin \theta (5 \cos^2 \theta - 1) e^{-i\varphi}$
$m = 0$	$\sqrt{\frac{1}{4\pi}}$	$\sqrt{\frac{3}{4\pi}} \cos \theta$	$\sqrt{\frac{5}{16\pi}} (3 \cos^2 \theta - 1)$	$\sqrt{\frac{7}{16\pi}} (5 \cos^3 \theta - 3 \cos \theta)$
$m = 1$		$-\sqrt{\frac{3}{8\pi}} \sin \theta e^{-i\varphi}$	$-\sqrt{\frac{15}{8\pi}} \sin \theta \cos \theta e^{i\varphi}$	$-\sqrt{\frac{21}{64\pi}} \sin \theta (5 \cos^2 \theta - 1) e^{i\varphi}$
$m = 2$			$\sqrt{\frac{15}{32\pi}} \sin^2 \theta e^{2i\varphi}$	$\sqrt{\frac{105}{32\pi}} \sin^2 \theta \cos \theta e^{2i\varphi}$
$m = 3$				$-\sqrt{\frac{35}{64\pi}} \sin^3 \theta e^{3i\varphi}$

Table A.1.: Spherical harmonics up to $\ell = 3$.

A.2. Associated Legendre polynomials

Associated Legendre polynomials for $\ell \geq 0$ and $-\ell \leq m \leq \ell$ are defined as derivatives of ordinary Legendre polynomials

$$P_\ell^m(x) = (-1)^m (1-x^2)^{m/2} \frac{d^m}{dx^m} P_\ell(x) = \frac{(-1)^m}{2^\ell \ell!} (1-x^2)^{m/2} \frac{d^{\ell+m}}{dx^{\ell+m}} (x^2-1)^\ell. \quad (\text{A.6})$$

In contrast to associated Legendre polynomials, ordinary Legendre polynomials $P_\ell(x)$ are actual polynomials. Associated Legendre polynomials for negative values of m are proportional to the corresponding functions with positive m :

$$P_\ell^{-m}(x) = (-1)^m \frac{(\ell-m)!}{(\ell+m)!} P_\ell^m(x) \quad (\text{A.7})$$

The associated Legendre polynomials up to $\ell = 3$ are listed in table A.2.

Derivatives of associated Legendre polynomials are linear combinations of associated Legendre polynomials:

$$P_\ell^{m'}(x) = \frac{(\ell-m+1)P_{\ell+1}^m(x) - (\ell+1)xP_\ell^m(x)}{x^2-1} \quad (\text{A.8})$$

The prime denotes derivation with respect to the argument, i.e.

$$P_\ell^{m'}(x) = \left. \frac{dP_\ell^m(y)}{dy} \right|_{y=x}. \quad (\text{A.9})$$

Associated Legendre polynomials and their derivatives are even or odd functions:

$$P_\ell^m(-x) = (-1)^{\ell+m} P_\ell^m(x) \quad P_\ell^{m'}(-x) = (-1)^{\ell+m+1} P_\ell^{m'}(x) \quad (\text{A.10})$$

$P_\ell^m(x)$	$\ell = 0$	$\ell = 1$	$\ell = 2$	$\ell = 3$
$m = -3$				$\frac{1}{48} \sqrt{1-x^2}(1-x^2)$
$m = -2$			$\frac{1}{8}(1-x^2)$	$\frac{1}{8}x(1-x^2)$
$m = -1$		$\frac{1}{2} \sqrt{1-x^2}$	$\frac{1}{2}x \sqrt{1-x^2}$	$\frac{1}{8} \sqrt{1-x^2}(5x^2-1)$
$m = 0$	1	x	$-\frac{1}{2}(1-3x^2)$	$\frac{1}{2}(5x^3-3x)$
$m = 1$		$-\sqrt{1-x^2}$	$-3x \sqrt{1-x^2}$	$-\frac{3}{2} \sqrt{1-x^2}(5x^2-1)$
$m = 2$			$3(1-x^2)$	$15x(1-x^2)$
$m = 3$				$-15 \sqrt{1-x^2}(1-x^2)$

Table A.2.: Associated Legendre polynomials up to $\ell = 3$.

For $|x| > 1$ the values of associated Legendre polynomials and their derivatives are real for m even and pure imaginary for m odd:

$$P_\ell^{2m}(x), P_\ell^{2m'}(x) \in \mathbb{R} \quad P_\ell^{2m+1}(x), P_\ell^{2m+1'}(x) \in i\mathbb{R} \quad (\text{A.11})$$

The generalization of associated Legendre polynomials to values of $|x| > 0$ is not unique as the square root has two solutions. We use the convention $\sqrt{1-x^2} \equiv +i\sqrt{x^2-1}$ for $|x| > 1$. However, products of associated Legendre polynomials and its derivatives are independent of this choice and are real or pure imaginary:

$$P_{\ell_1}^m(x) P_{\ell_2}^m(x) \in \mathbb{R} \quad P_{\ell_1}^{m'}(x) P_{\ell_2}^{m'}(x) \in \mathbb{R} \quad P_{\ell_1}^m(x) P_{\ell_2}^{m'}(x) \in i\mathbb{R} \quad (\text{A.12})$$

With definition (A.6) associated Legendre polynomials can be written as a series

$$P_\ell^m(x) = \frac{(-1)^m}{2^\ell \ell!} (1-x^2)^{m/2} \sum_{k=0}^{\ell} (-1)^k \binom{\ell}{k} \frac{d^{\ell+m}}{dx^{\ell+m}} x^{2\ell-2k}, \quad (\text{A.13})$$

where the derivative is given by:

$$\frac{d^{\ell+m}}{dx^{\ell+m}} x^{2\ell-2k} = \begin{cases} 0 & \text{for } k > \frac{\ell-m}{2} \\ \frac{(2\ell-2k)!}{(\ell-2k-m)!} x^{\ell-2k-m} & \text{otherwise} \end{cases} \quad (\text{A.14})$$

For $x \gg 1$ the term $k = 0$ is dominant and we find the approximations

$$P_\ell^m(x) \simeq \frac{(-1)^m}{2^\ell \ell!} (1-x^2)^{m/2} x^m \frac{d^{\ell+m}}{dx^{\ell+m}} x^{2\ell} \simeq \frac{(-i)^m (2\ell)!}{2^\ell \ell! (\ell-m)!} x^\ell, \quad (\text{A.15})$$

$$P_\ell^{m'}(x) \simeq \frac{(-i)^m (2\ell)!}{2^\ell (\ell-1)! (\ell-m)!} x^{\ell-1}. \quad (\text{A.16})$$

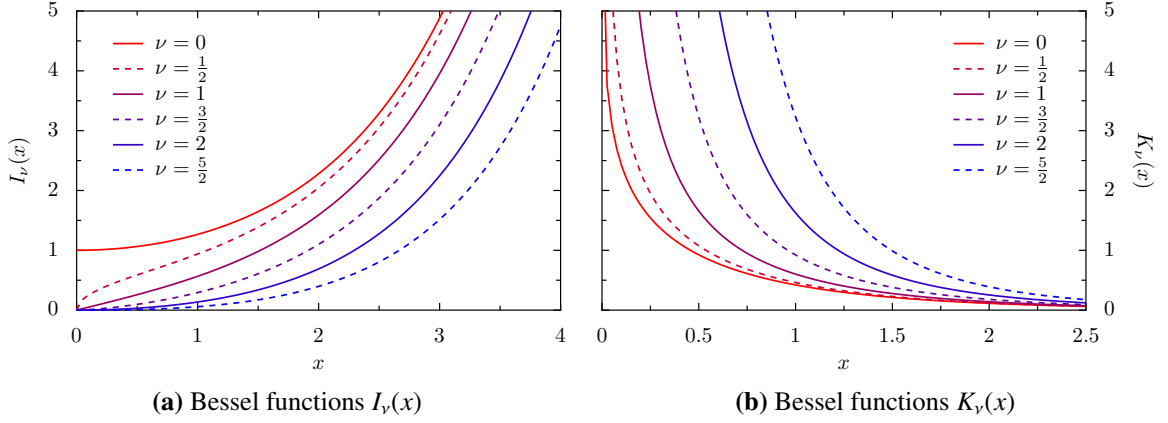


Figure A.1.: Modified Bessel function a) of the first kind and b) of the second kind for various values of ν .

A.3. Wigner (small) d-matrix elements

With eqs. (67) and (68) from [40], one can show

$$\begin{aligned}
 d_{m,1}^\ell(\theta) + d_{m,-1}^\ell(\theta) &= (-1)^{m+1} \sqrt{\frac{2}{\ell(\ell+1)(2\ell+1)}} 2\pi_{\ell m}(\theta) \\
 &= (-1)^{m+1} \sqrt{\frac{2}{\ell(\ell+1)(2\ell+1)}} \frac{2m \bar{P}_\ell^m(\cos \theta)}{\sin \theta} = \frac{-\sqrt{8}m N_{\ell m}}{\sqrt{\ell(\ell+1)(2\ell+1)}} \frac{P_\ell^m(\cos \theta)}{\sin \theta}
 \end{aligned} \tag{A.17}$$

and

$$\begin{aligned}
 d_{m,1}^\ell(\theta) - d_{m,-1}^\ell(\theta) &= (-1)^{m+1} \sqrt{\frac{2}{\ell(\ell+1)(2\ell+1)}} 2\bar{\pi}_{\ell m}(\theta) \\
 &= -2 \sqrt{\frac{(\ell-m)!}{\ell(\ell+1)(\ell+m)!}} \frac{dP_\ell^m(\cos \theta)}{d\theta} = \frac{\sqrt{8} N_{\ell m}}{\sqrt{\ell(\ell+1)(2\ell+1)}} P_\ell^{m'}(\cos \theta) \sin \theta.
 \end{aligned} \tag{A.18}$$

Definitions and properties of Wigner small d-matrix elements are described in Refs. [4, 47].

A.4. Modified Bessel functions

The modified Bessel functions of the first kind $I_\nu(x)$ and the modified Bessel function of the second kind $K_\nu(x)$ are defined by

$$I_\nu(x) = \sum_{k=0}^{\infty} \frac{1}{k! \Gamma(k + \nu + 1)} \left(\frac{x}{2}\right)^{2k+\nu}, \quad K_\nu(x) = \frac{\pi}{2} \frac{I_{-\nu}(x) - I_\nu(x)}{\sin(\nu\pi)}. \tag{A.19}$$

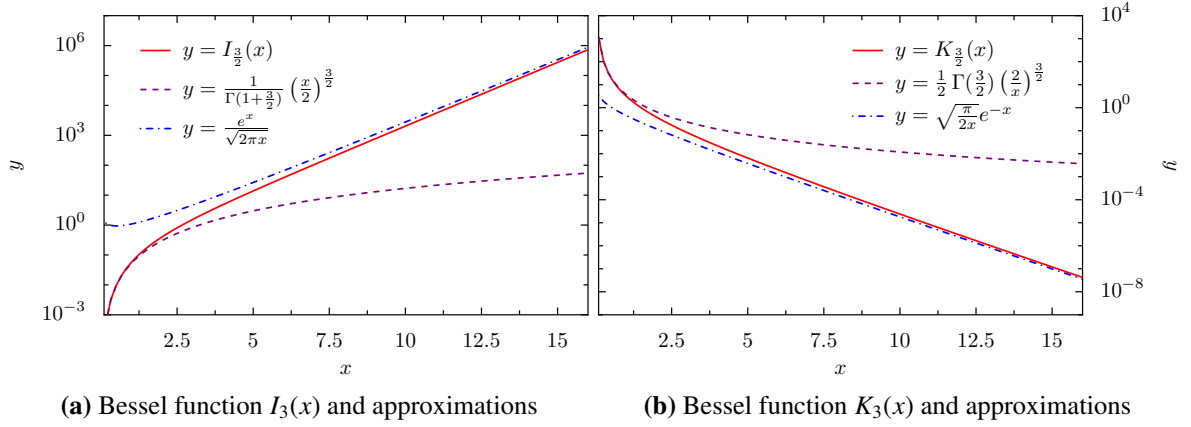


Figure A.2.: Bessel functions a) $I_{3/2}(x)$ and b) $K_{3/2}(x)$, and approximations (A.21) and (A.22).

The modified Bessel functions satisfy the recurrence relations

$$I_{\nu-1}(x) - I_{\nu+1}(x) = \frac{2\nu I_{\nu}(x)}{x}, \quad K_{\nu+1}(x) - K_{\nu-1}(x) = \frac{2\nu K_{\nu}(x)}{x}. \quad (\text{A.20})$$

For $|x| \ll 1$ the modified Bessel functions may be approximated by

$$I_{\nu}(x) = \frac{1}{\Gamma(\nu+1)} \left(\frac{x}{2}\right)^{\nu} + \mathcal{O}(x^{\nu+2}), \quad K_{\nu}(x) = \frac{\Gamma(\nu)}{2} \left(\frac{2}{x}\right)^{\nu} + \mathcal{O}(x^{\nu+2}), \quad (\text{A.21})$$

and for $|x| \gg 1$ by

$$I_{\nu}(x) = \frac{e^x}{\sqrt{2\pi x}} \left[1 + \mathcal{O}\left(\frac{1}{x}\right)\right], \quad K_{\nu}(x) = \sqrt{\frac{\pi}{2x}} e^{-x} \left[1 + \mathcal{O}\left(\frac{1}{x}\right)\right]. \quad (\text{A.22})$$

Fig. A.1 shows modified Bessel functions of the first and second kind for various values of ν , Fig. A.2 shows the modified Bessel functions $I_{3/2}$ and $K_{3/2}$, and its approximations.

A.5. Polylogarithms

Polylogarithms are functions that are defined by the power series

$$\text{Li}_s(x) = \sum_{k=1}^{\infty} \frac{x^k}{k^s} \quad (\text{A.23})$$

and depend on a parameter s . The series converges for $|x| \leq 1$. The polylogarithms for $s = 0$ and $s = 1$ can be expressed analytically:

$$\text{Li}_0(x) = \frac{x}{1-x} \quad \text{Li}_1(x) = -\ln(1-x) \quad (\text{A.24})$$

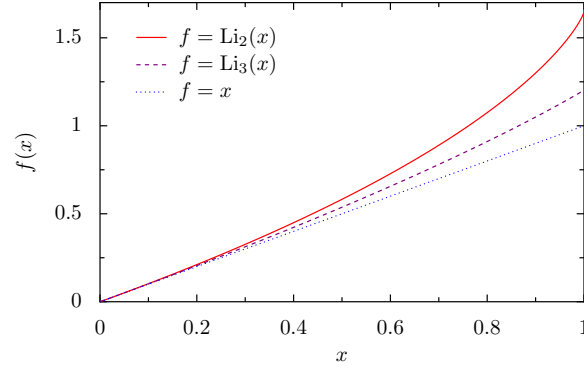


Figure A.3.: Polylogarithm for $s = 2$ and $s = 3$.

For integer orders of s polylogarithms can be expressed using the recurrence formula

$$\text{Li}_{s+1}(x) = \int_0^x dt \frac{\text{Li}_s(t)}{t}. \quad (\text{A.25})$$

For $x = 1$ the polylogarithms reduce to the Riemann zeta function

$$\text{Li}_s(1) = \zeta(s). \quad (\text{A.26})$$

For $x \ll 1$ all summands in (A.23) but $k = 1$ can be neglected and we find the approximation

$$\text{Li}_s \simeq x. \quad (\text{A.27})$$

In Fig. A.3 we plot the polylogarithms Li_2 and Li_3 .

B. Proofs and mathematical transformations

B.1. Normalization

In this section, we determine the normalizing constant A from the condition

$$\langle \mathbf{k}', \omega', \phi', p' | \mathbf{k}, \omega, \phi, p \rangle \stackrel{!}{=} \delta_{pp'} \delta_{\phi\phi'} \delta(\mathbf{k} - \mathbf{k}') \delta\left(\frac{\omega}{c} - \frac{\omega'}{c}\right). \quad (\text{B.1})$$

Inserting the identity operator yields

$$\begin{aligned} \langle \mathbf{k}', \omega', \phi', p' | \mathbf{k}, \omega, \phi, p \rangle &= \int d^3\mathbf{R} \langle \mathbf{k}', \omega', \phi', p' | \mathbf{R} \rangle \langle \mathbf{R} | \mathbf{k}, \omega, \phi, p \rangle \\ &= |A|^2 (2\pi)^3 \delta_{pp'} \delta(\mathbf{k} - \mathbf{k}') \delta(\phi k_z - \phi' k'_z) \\ &= |A|^2 (2\pi)^3 \delta_{pp'} \delta(\mathbf{k} - \mathbf{k}') \delta\left(\sqrt{\frac{\omega^2}{c^2} - k^2} - \frac{\phi'}{\phi} \sqrt{\frac{\omega'^2}{c^2} - k^2}\right), \end{aligned} \quad (\text{B.2})$$

where we have used that the delta function is even.

In order to cast (B.2) in the form of (B.1) we have to rewrite the second delta function. We use the identity

$$\delta(f(x)) = \sum_i \frac{\delta(x - x_i)}{|f'(x_i)|}, \quad (\text{B.3})$$

where x_i are the roots of $f(x)$. We find

$$f\left(\frac{\omega}{c}\right) = \sqrt{\frac{\omega^2}{c^2} - k^2} - \frac{\phi'}{\phi} \sqrt{\frac{\omega'^2}{c^2} - k^2}, \quad f'\left(\frac{\omega}{c}\right) = \frac{\omega}{c \sqrt{\frac{\omega^2}{c^2} - k^2}} = \frac{\omega}{c k_z}. \quad (\text{B.4})$$

As ω and ω' are non-negative, f has just one root at $\omega/c = \omega'/c$ for $\phi = \phi'$. For $\phi \neq \phi'$ the function f has no roots and the integral (B.2) vanishes. We therefore transform the delta function to

$$\delta\left(\sqrt{\frac{\omega^2}{c^2} - k^2} - \frac{\phi'}{\phi} \sqrt{\frac{\omega'^2}{c^2} - k^2}\right) = \delta_{\phi, \phi'} \left| \frac{c k_z}{\omega} \right| \delta\left(\frac{\omega}{c} - \frac{\omega'}{c}\right). \quad (\text{B.5})$$

With (B.5) eq. (B.2) becomes

$$\begin{aligned} \langle \mathbf{k}', \omega', \phi', p' | \mathbf{k}, \omega, \phi, p \rangle &= |A|^2 (2\pi)^3 \delta_{pp'} \delta_{\phi, \phi'} \delta(\mathbf{k} - \mathbf{k}') \left| \frac{ck_z}{\omega} \right| \delta\left(\frac{\omega}{c} - \frac{\omega'}{c}\right) \\ &\stackrel{!}{=} \delta_{pp'} \delta_{\phi, \phi'} \delta(\mathbf{k} - \mathbf{k}') \delta\left(\frac{\omega}{c} - \frac{\omega'}{c}\right) \end{aligned}$$

and the normalization constant A is given by

$$A = \frac{1}{(2\pi)^{3/2}} \sqrt{\left| \frac{\omega}{ck_z} \right|}. \quad (\text{B.6})$$

The constant A is only unique up to an arbitrary phase factor. We choose A to be real.

B.2. Commutation of \mathcal{J}_z and \mathcal{M}

The round-trip operator is invariant under arbitrary rotations around the z -axis, therefore it commutes with the rotation operator $\mathcal{R}_z(\varphi)$. The angular momentum operator is the generator of the rotation and the rotation operator can be expressed as

$$\mathcal{R}_z(\varphi) = \exp(-i\varphi \mathcal{J}_z). \quad (\text{B.7})$$

It is sufficient to consider an infinitesimal rotation, because any finite rotation can be built from infinitesimal rotations. For an infinitesimal rotation the rotation operator simplifies to

$$\mathcal{R}_z(\delta\varphi) = \mathbb{1} - i\delta\varphi \mathcal{J}_z \quad (\text{B.8})$$

and we can show that the round-trip operator commutes with the angular momentum operator

$$0 = [\mathcal{R}_z(\delta\varphi), \mathcal{M}] = (\mathbb{1} - i\delta\varphi \mathcal{J}_z) \mathcal{M} - \mathcal{M}(\mathbb{1} - i\delta\varphi \mathcal{J}_z) = i\delta\varphi [\mathcal{M}, \mathcal{J}_z] \quad (\text{B.9})$$

$$\Rightarrow [\mathcal{M}, \mathcal{J}_z] = 0. \quad (\text{B.10})$$

The z -component of the angular momentum is thus conserved during scattering processes, the round-trip operator is block diagonal with respect to m

$$\mathcal{M}(\omega) = \begin{pmatrix} \ddots & & & 0 \\ & \mathcal{M}^{(m-1)} & & \\ & & \mathcal{M}^{(m)} & \\ & & & \mathcal{M}^{(m+1)} \\ 0 & & & & \ddots \end{pmatrix}, \quad (\text{B.11})$$

and each block $\mathcal{M}^{(m)}$ yields an independent contribution to the free energy

$$\mathcal{F} = k_B T \sum_{n=0}^{\infty} \ln \det [\mathbb{1} - \mathcal{M}(\omega)] = k_B T \sum_{n=0}^{\infty} \sum_{m=-\infty}^{\infty} \ln \det [\mathbb{1} - \mathcal{M}^{(m)}(\omega)]. \quad (\text{B.12})$$

B.3. Determinants of block matrices

Let $A, B, C, D \in \mathbb{C}^{n \times n}$, $\lambda \in \mathbb{C}$, then it follows:

$$\det \begin{pmatrix} A & \lambda B \\ \frac{1}{\lambda} C & D \end{pmatrix} = \frac{1}{\lambda^n} \det \begin{pmatrix} \lambda A & \lambda B \\ C & D \end{pmatrix} = \frac{\lambda^n}{\lambda^n} \det \begin{pmatrix} A & B \\ C & D \end{pmatrix} = \det \begin{pmatrix} A & B \\ C & D \end{pmatrix} \quad (\text{B.13})$$

In particular, it follows

$$\det \begin{pmatrix} A & iB \\ iC & D \end{pmatrix} = \det \begin{pmatrix} A & -B \\ C & D \end{pmatrix} \quad (\text{B.14})$$

and

$$\det \begin{pmatrix} A & -B \\ -C & D \end{pmatrix} = \det \begin{pmatrix} A & B \\ C & D \end{pmatrix}. \quad (\text{B.15})$$

B.4. Equivalence of the matrix elements of CANAGUIER–DURAND et al.

At first glance the matrix elements (5.24)–(5.27) differ from those of CANAGUIER–DURAND et al. [10, 13], but the actual expressions can be rearranged into each other. We want to demonstrate this for the matrix element $\mathcal{M}_{\text{TE}}^{(m)}(E, E)_{\ell_1 \ell_2}$.

We start with the matrix element of CANAGUIER–DURAND et al. [10, 13]:

$$\mathcal{M}_{\text{TE}}^{(m)}(E, E)_{\ell_1 \ell_2} = \sqrt{\frac{(2\ell_1 + 1)\pi}{\ell_2(\ell_2 + 1)}} a_{\ell_1}(-im) \int_0^\infty \frac{dk}{\kappa} \left[d_{m,1}^{\ell_1}(\theta^+) + d_{m,-1}^{\ell_1}(\theta^+) \right] Y_{\ell_2, m}(\theta^-, 0) r_{\text{TE}} e^{-2\kappa \mathcal{L}} \quad (\text{B.16})$$

We can replace the sum of the Wigner d-matrix elements by an associated Legendre polynomial using (A.17). We also write the spherical harmonic in terms of an associated Legendre polynomial and get:

$$\begin{aligned} \mathcal{M}_{\text{TE}}^{(m)}(E, E)_{\ell_1 \ell_2} &= im^2 a_{\ell_1} \frac{\sqrt{8} N_{\ell_1 m}}{\sqrt{\ell_2(\ell_1 + 1)(2\ell_1 + 1)}} \sqrt{\frac{(2\ell_1 + 1)\pi}{\ell_2(\ell_2 + 1)}} \\ &\quad \times \int_0^\infty \frac{dk}{\kappa} \frac{P_{\ell_1}^m(\cos \theta^+)}{\sin \theta^+} \frac{N_{\ell_2 m}}{\sqrt{2\pi}} P_{\ell_2}^m(\cos \theta^+) r_{\text{TE}} e^{-2\kappa \mathcal{L}} \end{aligned} \quad (\text{B.17})$$

Sine and cosine of the Wick rotated polar angle can be expressed by

$$\sin \theta^\pm = \frac{-ick}{\xi}, \quad \cos \theta^\pm = \pm \frac{c\kappa}{\xi}. \quad (\text{B.18})$$

After inserting in (B.17), cancelling and resorting, we find

$$\begin{aligned} \mathcal{M}_{\text{TE}}^{(m)}(E, E)_{\ell_1 \ell_2} &= im^2 a_{\ell_1} \frac{-2N_{\ell_1 m} N_{\ell_2 m}}{\sqrt{\ell_1(\ell_1 + 1) \ell_2(\ell_2 + 1)}} \\ &\times \int_0^\infty \frac{dk}{\kappa} \frac{\xi}{ick} r_{\text{TE}} P_{\ell_1}^m \left(\frac{\kappa c}{\xi} \right) P_{\ell_2}^m \left(-\frac{\kappa c}{\xi} \right) e^{-2\kappa \mathcal{L}}. \end{aligned} \quad (\text{B.19})$$

This can be rearranged to

$$\mathcal{M}_{\text{TE}}^{(m)}(E, E)_{\ell_1 \ell_2} = \Lambda_{\ell_1 \ell_2}^{(m)} a_{\ell_1} \frac{m^2 \xi}{c} \int_0^\infty dk \frac{1}{\kappa k} r_{\text{TE}} P_{\ell_1}^m \left(\frac{\kappa c}{\xi} \right) P_{\ell_2}^m \left(-\frac{\kappa c}{\xi} \right) e^{-2\kappa \mathcal{L}} \quad (\text{B.20})$$

We see that (B.20) is identical to (5.24) for the TE mode.

B.5. $B_{\ell_1 \ell_2, p}^{(m)}$ for $\xi \rightarrow 0$

For $\xi = nT \rightarrow 0$ we may replace κ by k , because

$$\kappa = \sqrt{n^2 T^2 + k^2} \stackrel{nT \rightarrow 0}{=} k. \quad (\text{B.21})$$

Also, we assume the Fresnel coefficients to be independent of ξ and k . Then, we can put r_p in front of the integral and we obtain

$$B_{\ell_1 \ell_2, p}^{(m)} = \frac{r_p}{(nT)^3} \int_0^\infty dk e^{-2k} k^2 P_{\ell_1}^{m'} \left(\frac{k}{nT} \right) P_{\ell_2}^{m'} \left(-\frac{k}{nT} \right). \quad (\text{B.22})$$

For $nT \rightarrow 0$ the argument of the associated Legendre polynomials becomes large according to amount and they can be approximated using (A.16):

$$B_{\ell_1 \ell_2, p}^{(m)} \simeq r_p \frac{(-1)^{\ell_2+m+1} (-i)^{2m} (2\ell_1)! (2\ell_2)!}{2^{\ell_1+\ell_2} (\ell_1-1)! (\ell_2-1)! (\ell_1-m)! (\ell_2-m)!} \left(\frac{1}{nT} \right)^{\ell_1+\ell_2+1} \int_0^\infty dk e^{-2k} k^{\ell_1+\ell_2} \quad (\text{B.23})$$

The integral in (B.23) yields

$$\int_0^\infty dk e^{-2k} k^{\ell_1+\ell_2} = \frac{(\ell_1 + \ell_2)!}{2^{\ell_1+\ell_2+1}}, \quad (\text{B.24})$$

and after inserting we obtain

$$B_{\ell_1 \ell_2, p}^{(m)} \simeq r_p \frac{(-1)^{\ell_2+1} (2\ell_1)! (2\ell_2)! (\ell_1 + \ell_2)!}{2^{2\ell_1+2\ell_2+1} (\ell_1-1)! (\ell_2-1)! (\ell_1-m)! (\ell_2-m)!}. \quad (\text{B.25})$$

The diagonal block matrices thus become

$$\mathcal{M}^{(m)}(E, E)_{\ell_1 \ell_2} \simeq \Lambda_{\ell_1 \ell_2}^{(m)} a_{\ell_1} B_{\ell_1 \ell_2, \text{TM}}^{(m)} = \Xi_{\ell_1 \ell_2}^{(m)} r_{\text{TM}}^{\xi \rightarrow 0} a_{\ell, 0}^{\text{perf}} \left(\frac{R}{\mathcal{L}} \right)^{\ell_1 + \ell_2 + 1} \left(\frac{nT R}{\mathcal{L}} \right)^{\ell_1 - \ell_2}, \quad (\text{B.26})$$

$$\mathcal{M}^{(m)}(M, M)_{\ell_1 \ell_2} \simeq \Lambda_{\ell_1 \ell_2}^{(m)} b_{\ell_1} B_{\ell_1 \ell_2, \text{TE}}^{(m)} = \Xi_{\ell_1 \ell_2}^{(m)} r_{\text{TE}}^{\xi \rightarrow 0} b_{\ell, 0}^{\text{perf}} \left(\frac{R}{\mathcal{L}} \right)^{\ell_1 + \ell_2 + 1} \left(\frac{nT R}{\mathcal{L}} \right)^{\ell_1 - \ell_2}, \quad (\text{B.27})$$

where we have defined the prefactor

$$\Xi_{\ell_1 \ell_2}^{(m)} \equiv \Lambda_{\ell_1 \ell_2}^{(m)} \frac{(-1)^{\ell_2 + 1} (2\ell_1)! (2\ell_2)! (\ell_1 + \ell_2)!}{4^{2\ell_1 + \ell_2 + 1} (\ell_1 - 1)! (\ell_2 - 1)! (\ell_1 - m)! (\ell_2 - m)!}. \quad (\text{B.28})$$

The prefactors $a_{\ell, 0}^{\text{perf}}$ and $b_{\ell, 0}^{\text{perf}}$ have been defined in (3.35).

B.6. Determinant of $\mathcal{M}^{(m)}(P, P)$ for $\xi \rightarrow 0$

For $n = 0$ the Matsubara frequency $\xi_{n=0} = nT = 0$ vanishes. The matrix elements scale as $\mathcal{M}^{(m)}(P, P)_{l_1 l_2} \sim \lambda^{\ell_1 - \ell_2}$, where

$$\lambda = \frac{nT R}{\mathcal{L}}, \quad (\text{B.29})$$

and the matrix looks like

$$\mathcal{M}^{(m)}(P, P) = \begin{pmatrix} a_{11} \lambda^0 & a_{12} \lambda^{-1} & \cdots & a_{1n} \lambda^{-n+1} \\ a_{21} \lambda^1 & a_{22} \lambda^0 & \cdots & a_{2n} \lambda^{-n+2} \\ \vdots & & \ddots & \vdots \\ a_{n-1,1} \lambda^{n-2} & a_{n-1,2} \lambda^{n-3} & \cdots & a_{n-1,n} \lambda^{-1} \\ a_{n1} \lambda^{n-1} & a_{n2} \lambda^{n-2} & \cdots & a_{nn} \lambda^0 \end{pmatrix}, \quad (\text{B.30})$$

where a_{ij} are coefficients that are independent of λ .

Let us multiply the first row of the matrix by the factor λ^{n-1} , the second row by the factor λ^{n-2} , \dots , and the second last row by the factor λ^1 . As the determinant of a $n \times n$ matrix is a n -linear function, multiplying a row or a column by a factor α alters the determinant by a factor α . So we have to multiply $\lambda^{-1} \lambda^{-2} \dots \lambda^{-n+1}$ in order to keep the value of the determinant constant:

$$\det \mathcal{M}^{(m)}(P, P) = \prod_{k=1}^{n-1} \lambda^{-k} \det \begin{pmatrix} a_{11} \lambda^{n-1} & a_{12} \lambda^{n-2} & \cdots & a_{1n} \lambda^0 \\ a_{21} \lambda^{n-1} & a_{22} \lambda^{n-2} & \cdots & a_{2n} \lambda^0 \\ \vdots & & \ddots & \vdots \\ a_{n-1,1} \lambda^{n-1} & a_{n-1,2} \lambda^{n-2} & \cdots & a_{n-1,n} \lambda^0 \\ a_{n1} \lambda^{n-1} & a_{n2} \lambda^{n-2} & \cdots & a_{nn} \lambda^0 \end{pmatrix} \quad (\text{B.31})$$

If we now multiply the first column by the factor λ^{n-1} , the second column by the factor λ^{n-2} , \dots , and the second last column by the factor λ , the prefactor vanishes and we obtain:

$$\det \mathcal{M}^{(m)}(P, P) = \det \begin{pmatrix} a_{11} & a_{12} & \cdots & a_{1n} \\ a_{21} & a_{22} & \cdots & a_{2n} \\ \vdots & & \ddots & \vdots \\ a_{n-1,1} & a_{n-1,2} & \cdots & a_{n-1,n} \\ a_{n1} & a_{n2} & \cdots & a_{nn} \end{pmatrix} \quad (\text{B.32})$$

For this reason, the determinant is independent of λ and thus also independent of $\xi = nT$.

B.7. Infinite series

For $|q| < 1$ the value of the geometric series is:

$$\sum_{k=0}^{\infty} q^k = \frac{1}{1-q} \quad (\text{B.33})$$

By differentiating the left and right hand side of (B.33), and multiplying by the factor q afterwards, we obtain:

$$\sum_{k=0}^{\infty} kq^k = \frac{q}{(1-q)^2} \quad (\text{B.34})$$

Similarly, differentiating two times and multiplying by the factor q^2 yields:

$$\sum_{k=0}^{\infty} k^2 q^k = \frac{2q^2}{(1-q)^2} + \sum_{k=0}^{\infty} kq^k = \frac{q(q+1)}{(1-q)^3} \quad (\text{B.35})$$

B.8. Scattering at a sphere and factor -2

The matrix elements for the scattering at the sphere are given by

$$\langle \ell, m, E | \mathcal{R}_S | \ell, m, E \rangle = -2a_\ell(\omega), \quad (\text{B.36})$$

$$\langle \ell, m, M | \mathcal{R}_S | \ell, m, M \rangle = -2b_\ell(\omega). \quad (\text{B.37})$$

However, the appearance of the factor -2 is contrary to expectation. In this section, we will discuss the reason for the appearance of the factor -2 . The scattering of plane waves at a sphere is discussed in Refs. [27, 30], however, we will only refer to [6] in our argumentation.

The problem of absorption and scattering of electromagnetic waves at a sphere is usually called Mie scattering in literature. Usually, one considers a plane x -polarized wave that propagates in $+z$ -direction. Arbitrary incident angles and polarizations may be described by a rotation of the coordinate system using Wigner-D matrices [4, 47].

The incident plane wave may be expanded in VSH

$$\mathbf{E}_i(\mathbf{R}) = \sum_{\ell=1}^{\infty} E_{\ell} \left(\mathbf{M}_{o,\ell 1}^{(1)} - i\mathbf{N}_{e,\ell 1}^{(1)} \right), \quad E_{\ell} = i^{\ell} E_0 \frac{2\ell + 1}{\ell(\ell + 1)}, \quad (\text{B.38})$$

where E_0 corresponds to the amplitude of the incident wave, \mathbf{M} and \mathbf{N} are VSH. These VSH, however, differ from the VSH we introduced in section 2.4. The VSH \mathbf{M} and \mathbf{N} are defined in real space and have a radial dependence. The superscript “1” denotes that the radial dependence is given by spherical Bessel functions j_{ℓ} . Moreover, the VSH \mathbf{M} and \mathbf{N} are separated in even (e) and odd (o) functions, and the value of m is non-negative. In the expansion (B.38) all terms but $m = 1$ vanish.

The expansion of the scattered wave is given by

$$\mathbf{E}_s(\mathbf{R}) = - \sum_{\ell=1}^{\infty} E_{\ell} \left(b_{\ell} \mathbf{M}_{o,\ell 1}^{(3)} - ia_{\ell} i\mathbf{N}_{e,\ell 1}^{(3)} \right), \quad (\text{B.39})$$

where the superscript “3” denotes that the radial dependence is given by spherical Hankel functions of the first kind $h_{\ell}^{(1)}$.

Comparing (B.38) and (B.39) reveals that the sign in the matrix elements (B.36) and (B.37) is caused by the definition of the Mie coefficients:

$$\mathcal{R}_S \mathbf{N}_{o,\ell 1}^{(1)} = -a_{\ell} \mathbf{N}_{o,\ell 1}^{(3)} \quad (\text{B.40})$$

$$\mathcal{R}_S \mathbf{M}_{o,\ell 1}^{(1)} = -b_{\ell} \mathbf{M}_{o,\ell 1}^{(3)} \quad (\text{B.41})$$

However, the reason of the factor 2 is still unclear. Eqs. (B.40) and (B.41) are no eigenvalue equations, because the radial dependence for the incident and the scattered fields are different: The radial dependence of the incident wave is given by spherical Bessel functions j_{ℓ} , while the radial dependence of the scattered wave is given by spherical Hankel functions of the first kind $h_{\ell}^{(1)}$. So, the Hankel functions $h_{\ell}^{(1)}$ have to be converted to spherical Bessel functions j_{ℓ} . This is possible for different origins and the factor 2 is due to this conversion [8].

C. Numerical implementation

The numerical implementation raises serious numerical problems. Moreover, the implementation is supposed to be fast in order to obtain results in tolerable time. However, fast code is often in contradiction to readable code.

The implementation involves about 2400 lines of C code. In order to find errors and numerical problems at an early stage, as well as to prevent regressions, unit tests were used. Unit tests compare the returned value of a function with the expected value. The expected values were calculated using Maxima¹ or Wolfram Alpha². In total, the unit tests cover

- 33 tests for $\Lambda_{\ell_1 \ell_2}^{(m)}$,
- 22 tests for $\Xi_{\ell_1 \ell_2}^{(m)}$,
- 22 tests for the integrals $A_{\ell_1 \ell_2, p}^{(m)}, B_{\ell_1 \ell_2, p}^{(m)}, C_{\ell_1 \ell_2, p}^{(m)}, D_{\ell_1 \ell_2, p}^{(m)}$,
- 45 tests for the Bessel function I_ν ,
- 45 tests for the Bessel function K_ν ,
- 25 tests for the Mie coefficients a_ℓ and b_ℓ ,
- 1 test for the QR decomposition,
- 16 tests for the addition of numbers in the logarithm approach,
- 4 tests of $\ln \det \mathcal{D}^{(m)}(nT)$,
- 3 tests of \mathcal{F} .

Moreover, git was used as revision control system during the software development. Git helped more than one time to find errors.

The numerical implementation is licensed under the terms of the GNU General Public License version 2³ and can be downloaded from github⁴. Also, if the numerical implementation is useful to you, please give me feedback and consider to cite the implementation.

¹<http://maxima.sourceforge.net/>

²<http://www.wolframalpha.com/>

³<http://www.gnu.org/licenses/gpl-2.0.html>

⁴<https://github.com/michael-hartmann/Casimir>

Bibliography

- [1] M. Abramowitz and I. A. Stegun. *Handbook of Mathematical Functions: With Formulas, Graphs, and Mathematical Tables*. Applied mathematics series. Dover Publications, 1964.
- [2] N.W. Ashcroft and N.D. Mermin. *Solid state physics*. Science: Physics. Saunders College, 1976.
- [3] R. G. Barrera, G. A. Estevez, and J. Giraldo. “Vector spherical harmonics and their application to magnetostatics”. In: *European Journal of Physics* 6 (4 1985).
- [4] L. C. Biedenharn, J. D. Louck, and P. A. Carruthers. *Angular Momentum in Quantum Physics: Theory and Application*. Encyclopedia of Mathematics and its Applications. Cambridge University Press, 2009.
- [5] G. Bimonte and T. Emig. “Exact Results for Classical Casimir Interactions: Dirichlet and Drude Model in the Sphere-Sphere and Sphere-Plane Geometry”. In: *Phys. Rev. Lett.* 109 (16 2012).
- [6] Craig F. Bohren and D. R. Huffman. *Absorption and scattering of light by small particles*. Wiley science paperback series. Wiley, 1983.
- [7] M. Bordag et al. *Advances in the Casimir Effect*. International Series of Monographs on Physics. OUP Oxford, 2009.
- [8] A. Boström, G. Kristensson, and S. Ström. “Transformation properties of plane, spherical and cylindrical scalar and vector wave functions”. In: *International Journal of Modern Physics: Conference Series*. Acoustic, Electromagnetic and Elastic Wave Scattering, Field Representations and Introduction to Scattering 1 (1991), pp. 165–210.
- [9] I. Brevik, S. A. Ellingsen, and K. A. Milton. “Thermal corrections to the Casimir effect”. In: *New Journal of Physics* 8.10 (2006).
- [10] A. Canaguier-Durand. “Multipolar scattering expansion for the Casimir effect in the sphere-plane geometry.” PhD thesis. Université Pierre et Marie Curie, 2011.
- [11] A. Canaguier-Durand et al. “Casimir Interaction between Plane and Spherical Metallic Surfaces”. In: *Phys. Rev. Lett.* 102 (23 2009).
- [12] A. Canaguier-Durand et al. “Classical Casimir interaction in the plane-sphere geometry”. In: *Phys. Rev. A* 85 (5 2012).
- [13] A. Canaguier-Durand et al. “Thermal Casimir effect for Drude metals in the plane-sphere geometry”. In: *Phys. Rev. A* 82 (1 2010).
- [14] H. B. G. Casimir. “On the attraction between two perfectly conducting plates”. In: *Proc. K. Ned. Akad. Wet.* 51 (1948), pp. 793–795.

- [15] C. Cohen-Tannoudji, J. Dupont-Roc, and G. Grynberg. *Photons and Atoms: Introduction to Quantum Electrodynamics*. New York, NY: Wiley, 1989.
- [16] B. V. Derjaguin, I. I. Abrikosova, and E. M. Lifshitz. “Direct measurement of molecular attraction between solids separated by a narrow gap”. In: *Q. Rev. Chem. Soc.* 10 (3 1956), pp. 295–329.
- [17] B. Fornberg. “Generation of Finite Difference Formulas on Arbitrarily Spaced Grids”. In: *Mathematics of Computation* 51.184 (1988), pp. 699–706.
- [18] C. D. Fosco, F. C. Lombardo, and F. D. Mazzitelli. “Proximity force approximation for the Casimir energy as a derivative expansion”. In: 84.10, 105031 (Nov. 2011).
- [19] C. Genet, A. Lambrecht, and S. Reynaud. “Casimir force and the quantum theory of lossy optical cavities”. In: *Phys. Rev. A* 67 (4 2003).
- [20] H. Gies and K. Klingmüller. “Worldline algorithms for Casimir configurations”. In: 74.4, 045002 (Aug. 2006).
- [21] G.H. Golub and C.F. Van Loan. *Matrix Computations*. Johns Hopkins Studies in the Mathematical Sciences. Johns Hopkins University Press, 1996, pp. 206–236.
- [22] P. Hobson, G.P. Efstathiou, and A.N. Lasenby. *General Relativity: An Introduction for Physicists*. Cambridge University Press, 2006.
- [23] I. R. Hooper and J. R. Sambles. “Dispersion of surface plasmon polaritons on short-pitch metal gratings”. In: *Phys. Rev. B* 65 (16 2002).
- [24] IEEE Task P754. *ANSI/IEEE 754-1985, Standard for Binary Floating-Point Arithmetic*. Aug. 1985, p. 20.
- [25] G.-L. Ingold and A. Lambrecht. “Casimir effect from a scattering approach”. In: *ArXiv e-prints* (2014).
- [26] G.-L. Ingold, A. Lambrecht, and S. Reynaud. “Quantum dissipative Brownian motion and the Casimir effect”. In: 80.4, 041113 (Oct. 2009).
- [27] John D. Jackson. *Classical Electrodynamics Third Edition*. 3rd ed. Wiley, Aug. 1998.
- [28] R. L. Jaffe. *The Casimir Effect and the Quantum Vacuum*. 2005.
- [29] R. L. Jaffe and A. Scardicchio. “Casimir Effect and Geometric Optics”. In: *Physical Review Letters* 92.7, 070402 (Feb. 2004).
- [30] M. Kerker. *The scattering of light, and other electromagnetic radiation*. Physical chemistry. Academic Press, 1969.
- [31] G. L. Klimchitskaya, U. Mohideen, and V. M. Mostepanenko. “Casimir and van der Waals forces between two plates or a sphere (lens) above a plate made of real metals”. In: 61.6, 062107 (June 2000).
- [32] A. Lambrecht, P. Maia Neto, and S. Reynaud. “The Casimir effect within scattering theory”. In: *New Journal of Physics* 8 (10 2006).
- [33] A. Lambrecht and S. Reynaud. “Casimir Effect: Theory and Experiments”. In: *International Journal of Modern Physics A* 27, 1260013 (June 2012).

-
- [34] A. Lambrecht et al. “Casimir effect in the scattering approach: correlations between material properties, temperature and geometry”. In: *Lect.Notes Phys.* 834 (2011), pp. 97–127.
 - [35] F. Mignard and S. Klioner. “Analysis of astrometric catalogues with vector spherical harmonics”. In: *arxiv* (2012).
 - [36] K. A. Milton et al. “Negative Casimir Entropies in Nanoparticle Interactions”. In: *ArXiv e-prints* (May 2014).
 - [37] L. Moyaerts, K. Langfeld, and H. Gies. “Worldline Approach To The Casimir Effect”. In: *ArXiv High Energy Physics - Theory e-prints* (Nov. 2003).
 - [38] Claus Müller. *Foundations of the Mathematical Theory of Electromagnetic Waves*. Springer-Verlag, 1969.
 - [39] R. Onofrio. “Casimir forces and non-Newtonian gravitation”. In: *New Journal of Physics* 8 (237 2006).
 - [40] J. David Pendleton. “Euler angle geometry, helicity basis vectors, and the Wigner D-function addition theorem”. In: *American Journal of Physics* 71 (2003).
 - [41] L. P. Pitaevskii. “Casimir-Lifshitz Forces and Entropy”. In: *International Journal of Modern Physics A* 25 (2010).
 - [42] W. H. Press et al. *Numerical Recipes in FORTRAN; The Art of Scientific Computing*. 2nd. New York, NY, USA: Cambridge University Press, 1993.
 - [43] P. Rabinowitz and G. Weiss. “Tables of Abscissas and Weights for Numerical Evaluation of Integrals of the Form $\int_0^\infty e^{-x} x^n f(x) dx$ ”. In: *Mathematical Tables and Other Aids to Computation* 13.68 (1959), pp. 285–294.
 - [44] S. J. Rahi et al. “Scattering Theory Approach to Electrodynamic Casimir Forces”. In: *Phys.Rev.* D80 (2009).
 - [45] S. Reynaud et al. “The Scattering Approach to the Casimir Force”. In: *Int. J. Mod. Phys.* A25 (2010).
 - [46] A. G. Riess et al. “Observational Evidence from Supernovae for an Accelerating Universe and a Cosmological Constant”. In: 116 (Sept. 1998).
 - [47] M. E. Rose. *Elementary Theory of Angular Momentum*. Dover books on physics and chemistry. Dover, 1995.
 - [48] M. J. Sparnaay. “Measurements of attractive forces between flat plates”. In: *Physica* 24.6–10 (1958), pp. 751–764.
 - [49] J. A. Stratton. *Electromagnetic Theory*. McGraw-Hill Book Company, 1941.
 - [50] D. F. Styer. “What good is the thermodynamic limit?” In: *American Journal of Physics* 72 (1 2004), pp. 25–29.
 - [51] J. H. Wilkinson, C. Reinsch, and F. L. Bauer. *Handbook for Automatic Computation: Linear Algebra (Grundlehren der Mathematischen Wissenschaften, Vol 186)*. Springer-Verlag, 1986, pp. 315–326.